Important Notice

This copy may be used only for the purposes of research and private study, and any use of the copy for a purpose other than research or private study may require the authorization of the copyright owner of the work in question. Responsibility regarding questions of copyright that may arise in the use of this copy is assumed by the recipient.

THE UNIVERSITY OF CALGARY

Formulation of digital filters using polynomial

approximation methods with applications

to Bouguer gravity data from

northern Alberta

by

Jeffrey Blair Thurston

A THESIS

SUBMITTED TO THE FACULTY OF GRADUATE STUDIES

IN PARTIAL FULFILMENT OF THE REQUIREMENTS FOR THE

DEGREE OF MASTER OF SCIENCE

DEPARTMENT OF

GEOLOGY AND GEOPHYSICS

CALGARY, ALBERTA

AUGUST, 1991

THE UNIVERSITY OF CALGARY

FACULTY OF GRADUATE STUDIES

The undersigned certify that they have read, and recommend to the Faculty of Graduate Studies for acceptance, a thesis entitled, "Formulation of digital filters using polynomial approximation methods with applications to Bouguer gravity data from northern Alberta", submitted by Jeffrey Blair Thurston in partial fulfilment of the requirements for the degree of Master of Science.
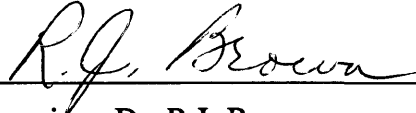
Supervisor, Dr. R.J. Brown
Geology and Geophysics

Dr. R.R. Stewart
Geology and Geophysics

Dr. T.M. Gordon
Geology and Geophysics
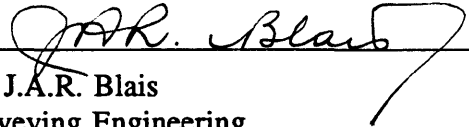
Dr. J.A.R. Blais
Surveying Engineering

August 1991

Abstract

One approach to local least-squares polynomial approximation of data in two independent variables consists of centring a square subarea on each point in a data set and computing the coefficients that define the best-fit polynomial over the subset defined by this window. Replacing the input sample at the centre of the window with the value of the best-fit polynomial enables formulation of an expression for the impulse responses of low-pass filters. This is simplified if the approximating function is written in terms of orthogonal polynomials. Cutoff frequencies of these filters are inversely proportional to the size of the subarea and proportional to the polynomial order. Polynomial order has been defined as the highest power either of any term in the polynomial or of any independent variable in the polynomial. The latter definition results in polynomials that consist of all of the terms that comprise polynomials arising from the former definition, as well as higher-order cross terms. Including these extra terms lessens the directional bias of the transfer functions. However, some distortion persists, with lowest frequencies passed in the direction of the coordinate axes and highest frequencies passed at 45° to the axes. The dependency of cutoff frequency on polynomial order and window size has been empirically quantified. These results, coupled with the expressions for the impulse responses, make possible the design of convolution operators without transformation to the frequency domain. Application of these local least-squares operators to a Bouguer gravity data set from northern Alberta indicates that these produce regional anomaly fields that are generally similar to those obtained from wavelength filtering.

Approximating an entire data set with one polynomial is commonly done to compute long-wavelength constituents of the Bouguer gravity field. When this technique is formulated in terms of convolution, a unique weight function operates on each data point. The operators for the central portion of the data set have amplitude responses that are similar to those of the local least-squares operators. This implies that polynomial approximation of the long-wavelength components of the gravity field should incorporate the higher-order cross terms in order to diminish directional bias. This is demonstrated by applying this method to the aforementioned Bouguer gravity data.

The local least-squares filters have been transformed to operators that output the components of the horizontal-gradient vector. This combines the high-frequency amplification property of differentiation with the low-pass nature of local least-squares approximation. This generates operators with both variable passbands and a likeness to the ideal response in this passband. These gradient-component operators have been used to compile a suite of maps of the magnitude of the horizontal-gradient vector of the Bouguer gravity field, featuring different bandwidths of crustal anomalies. Because the procedure is formulated in terms of convolution, the frequency content of each magnitude map is known. This facilitates the generation of complementary pairs of gradient-magnitude and wavelength-filtered maps. The gradient-magnitude maps enhance the interpretation by highlighting density boundaries. This is useful for mapping the edges of source bodies, identifying subtle characteristics, and determining spatial relationships between trends.

Acknowledgements

I am grateful to my supervisor, Dr. Brown, for his guidance through the course of this work. His urging to explore questions that were of foremost interest to me made this project a satisfying and rewarding experience.

I owe thanks to the members of my committee for proofreading the text, and improving the thesis by highlighting some inconsistencies in the original draft. As well, courses taught by E.S. Krebes, F.A. Cook, D.C. Lawton, and R.R. Stewart improved my understanding of a number of topics in the earth sciences.

Home Oil Co. Ltd. was instrumental in initiating the project, and the enthusiasm demonstrated by Arnold Rivett and Vadim Lyatsky was greatly appreciated.

My parents, Norma and Don, were a seemingly inexhaustible supply of support and advice. My brothers, Ross and Tim, recognized when my spirit was flagging, and were on hand with encouragement and diversions.

Last but not least, thanks are due to the many friends who put up with/helped/tolerated me in these three years.

Table of Contents

List of Tables

viii

List of Figures

approximating polynomial is computed for each data point. While the concept is not

original, a comprehensive investigation of the nature and applications of this method

does not exist to my knowledge for data in two independent variables. Hence, the

present study was initiated.

It is found that this approach to least-squares polynomial approximation is

well-suited to the formulation of two types of digital filters: low-pass phase-invariant

filters with predictable and reliable amplitude spectra, and horizontal-gradient-

component filters, with variable and measurable passbands. The weights of the

operators for the low-pass filters are computed using analytic expressions in the space

domain, and hence the impulse responses can be generated without transformation to

the frequency domain. A significant portion of the analysis of these weight functions

addresses the form that the approximating polynomial should adopt. This is

incorporated into an investigation of the frequency-domain properties of the ensuing

impulse responses. Further, while the approach in which a single approximating

polynomial is used differs fundamentally from the local approximation technique, the

results of the discussion of the local least-squares method, in particular the analysis

pertaining to the form of the approximating polynomial, is applicable. Thus some

implications for the conventional technique are discussed and illustrated. This

illuminates some subtle yet important details of geophysical applications of least-

squares polynomial approximation. The transfer functions of the horizontal-gradient-

component filters adhere closely to the ideal gradient-component filter responses.

The thesis is structured in the following way: the impulse responses describing

Chapter 1 - Introduction

There are two main objectives of this thesis. The first is to use least-squares polynomial approximation methods to develop analytic expressions for the impulse responses of digital filters for data in two independent variables. The second is to apply these weight functions to a Bouguer gravity data set from north-central Alberta in order to compare the processed data with those obtained from standard digital filters.

This body of work evolved from an algorithm devised by Dr. R.J. Brown in conjunction with a group of geologists at Home Oil Company Ltd. They were incorporating potential-field data into a regional study of the crystalline basement underlying the Western Canada Sedimentary Basin. The algorithm was designed to compute horizontal-gradient vector components for application to gravity and magnetic data. While the details of the procedure are described in chapter 3, at present it suffices to say that the method is based on approximating unique best-fit polynomials, in a least-squares sense, to local windows of the data.

Least-squares polynomial approximation is widely applied for the processing of potential-field data, and a review of the pertinent literature is presented in chapter 2. The usual approach is to compute the regional field, which is the contribution to the anomalous field that is thought to arise from deep-seated large-scale features, by approximation of an entire data set with a single low-order polynomial. The particular adaptation of this method that is the focus of this thesis, namely local least-squares polynomial approximation, deviates from the typical approach in that a unique

the local least-squares polynomial approach are first derived and studied; implications

for the more conventional method of approximating an entire data set with a single

polynomial are discussed; the local operators are transformed to gradient-component

operators, whose frequency-domain characteristics are in turn studied; conventional

wavelength filtering is applied to a Bouguer gravity data set, the results of which are

interpreted; and the polynomial approximation techniques are applied to the same

Bouguer data set for comparison with the results of the wavelength filtering.

Chapter 2 - Least-Squares Polynomial Approximation Filters

Introduction

Originally, the focus of the present investigation was to develop an algorithm for computing the magnitude of the horizontal gradient for the purpose of highlighting trends on areal Bouguer gravity data. The mathematical details of the approach are given in the following chapter, however the method can be summarized as: obtain a best-fit least-squares polynomial in a local window of the data and; analytically differentiate this polynomial with respect to the position variables to obtain the components of the horizontal gradient. The gradient components are then assigned to the centre of the window. The gradient data are compiled by centring the window at each grid point.

The original algorithm was based on obtaining the regression coefficients by the method outlined by Davis (1986). The foundation of this technique is the inversion of a Hilbert matrix. This procedure was later supplanted by a technique developed from concepts originated by Wood and Hockens (1970) and Chan and Leong (1972). For data in one independent variable these authors formulated local least-squares polynomial smoothing as convolution. This technique entails replacing each input datum at the centre of a moving window with the value at that point of the best-fit polynomial. The derivative theorem of convolution makes it possible to convert these smoothing filters to gradient filters; however, it is first necessary to extend the local least-squares polynomial operators to two independent variables. It is this task that is

addressed in this chapter.

The chapter began as a brief introduction for the following chapters. However, in the course of this work several questions arose that have not been addressed elsewhere, and consequently warrant further investigation. Thus this chapter explores several aspects of polynomial approximation of gravity data. The result is a study that fulfils its original objective, and provides an enhanced understanding of geophysical applications of polynomial approximation.

This study begins with a justification of polynomials as the approximating function. This is followed by the formulation of the expression for two-dimensional local least-squares polynomial impulse responses, which in turn facilitates a frequency-domain analysis of these weight functions. The chapter concludes with a discussion of the utility of these impulse responses.

Approximating gravity data by polynomials

The purpose of the following discussion is to verify that local least-squares fitting of a function to areal gravity data should be performed with a polynomial of order n and either of the form:

$$F(x,y) = \sum_{r=0}^{r+s\leq n} \sum_{s=0} a_{rs} x^r y^s, \qquad (2.1a)$$

or of the form:

$$F(x,y) = \sum_{r=0}^{n} \sum_{s=0}^{n} a_{rs} x^r y^s. \tag{2.1b}$$

The difference between these two forms is demonstrated by table 2.1, which contains the terms in the polynomial for n equal to 4. The form specified by equation 2.1a contains the terms that are above the solid line, whereas the form specified by equation 2.1b contains all the terms in table 2.1

1	x	x^2	x^3	x^4
y	xy	x^2y	x^3y	x^4y
y^2	xy^2	x^2y^2	x^3y^2	x^4y^2
y^3	xy^3	x^2y^3	x^3y^3	x^4y^3
y^4	xy^4	x^2y^4	x^3y^4	x^4y^4

Table 2.1
Terms included in approximating polynomials.

At this point it is not clear which is the preferable form. This will, however, become obvious in the course of the forthcoming frequency-domain analysis. Because this argument applies equally for both polynomial types, the upper limits of the summations will be omitted for the sake of generality, with the understanding that these limits are specified in equations 2.1.

This discussion is founded on a theorem fundamental to approximation theory given by Weierstrass (Achieser, 1956). For data in two independent variables this theorem can be stated as: for a function $f(x,y)$ which is continuous over a finite interval, to each $\varepsilon > 0$ there corresponds a polynomial of the form of equations 2.1 such that the inequality:

$$|F(x,y) - f(x,y)| < \epsilon \qquad (2.2)$$

is satisfied over the interval defined by x and y. In addition, if $f(x,y)$ is 2-π periodic, continuous everywhere, and differentiable at x and y, then its trigonometric sum (Fourier series), given by

$$F(x,y) = \sum_{m=0}^{\infty} \sum_{n=0}^{\infty} a_{mn}\cos(mx)\cos(ny) + b_{mn}\cos(mx)\sin(ny) \qquad (2.3)$$
$$+ c_{mn}\sin(mx)\cos(ny) + d_{mn}\sin(mx)\sin(ny),$$

converges to $f(x,y)$ at x and y.

There are numerous accounts of approximating gravity data with polynomials of the form of equations 2.1. A brief review of these is given in the following section. In addition, Henderson and Cordell (1971) have reported accurate representations using Fourier series expansion. Thus, for most applications, approximations to gravity data may be performed with either polynomial or Fourier series expansion. The focus of this study is the computation of approximating functions over relatively small subsets of the data. The limited areal size of the window impedes the use of Fourier series expansion. This is because the record length, N, determines the fundamental frequency, 1/N, and the increment between consecutive harmonics (i.e. the spectral resolution), 2/N, 3/N, ..., present in the Fourier series expansion. Because of this, selection of the record length, which in this case is the spatial dimensions of the window, is tied to the spectral content of the data. In practice, windows should be sufficiently large so as to include several wavelengths of the lowest frequencies present in the data (Båth, 1974). On the other hand, polynomial approximation is not

inhibited by this restriction. That is, polynomials of the form of equations 2.1 can approximate data with infinitely many wavelengths regardless of window size, the inherent difference being that polynomial approximation requires no assumptions regarding the periodicity of the signal. Thus Fourier series expansion does not lend itself to local approximations over subsets of the entire data set.

Applications of polynomial approximation

Potential-field data are generally subjected to a separation procedure before a quantitative interpretation is undertaken. The goal of this operation is to separate the long-wavelength anomalies, attributed to deep sources and often termed the regional field, from shorter wavelength features which are assumed to arise from shallower sources and often said to constitute the residual field. There are a great many studies in the literature that describe methods for performing this separation. These techniques can be divided into three general categories: manual smoothing; approximating the long-wavelength component of the field with a low-order polynomial; and linear digital filtering.

Approximating a data set by the method of least squares can be approached in two ways: the entire data set can be replaced by repeatedly evaluating the same polynomial (herein called global least-squares polynomial fitting); or a unique set of polynomial coefficients, based only on neighbouring points, can be generated for each observation (herein called local least-squares polynomial fitting). Application of either method results in a smoothed version of the field, which for an appropriate choice of

coefficients can be considered to be the regional. This regional can either be subtracted from the original data to produce a residual, or retained as a smoothed version of the input.

Early applications of this technique to potential-field measurements favoured global least-squares polynomial fitting in order to compute residuals (Agocs, 1951; Simpson, 1954; Swarz, 1954). This may have been due to the then prohibitive number of computations required to repeatedly perform a local least-squares fit. Some more recent studies still adopt this approach (Abdelrahman et al., 1985; 1989; Zeng, 1989). On the other hand, there are a number of applications that rely on the local least-squares approximation method for residual/regional separation (Wood and Hockens, 1970; Chan and Leong, 1972; Ku, 1990). As well, this approach is used to compute the 'interference term' in Werner deconvolution (Hartman et al., 1971; Kilty, 1982). Finally, Chandler et al. (1981), and von Frese et al. (1982) integrated local least-squares polynomial fitting into a scheme for quantitatively correlating gravity and magnetic anomalies. For large-scale surveys, one might expect this to be a more reasonable approach, because the character of the field, with its diverse influences, will vary considerably, and it is likely inappropriate to approximate the long-wavelength components with a single polynomial.

Three studies detailing the filtering characteristics of global and local polynomial approximation techniques have been encountered. In all of these, the formulation as convolution is accomplished by writing the best-fit polynomial in terms of orthogonal polynomials. For data in one independent variable it has been shown

that removing residual features via local least-squares approximation is equivalent to linear digital filtering (Wood and Hockens, 1970; Chan and Leong, 1972). These authors also investigated the wavenumber-domain characteristics of these filters. In addition, Lance (1982) presented formulations for global one- and two-dimensional least-squares polynomial convolution operators and investigated the filtering characteristics of the one-dimensional operators. The purpose of the present frequency-domain investigation is to extend the analysis of one-dimensional local least-squares operators, presented by Wood and Hockens (1970) and Chan and Leong (1972), to the two-dimensional local least-squares convolution operators, derived in this study.

Obtaining the Fourier transform of the impulse response facilitates examination of the transfer functions of these filters and makes it possible to evaluate their effectiveness and reliability in performing regional and residual separation of potential-field data. Knowledge of the behaviour of the transfer functions of these operators provides a quantitative criterion for selecting the parameters that determine the passband of the filter. As well, this enables reliable estimates of the wavenumber content of the filtered maps.

Local least-squares separation filters
The method of nonorthogonal polynomials

The use of nonorthogonal polynomials in least-squares approximation for highlighting trends in potential-field data is well known (Agocs, 1951; Fajklewicz, 1959; Coons et al., 1967; Abdelrahman et al., 1985). Further, a detailed summary has

been given by Davis (1986). Hence only a cursory discussion is presented here. It is important to note that the following discussion is tailored to the case in which a polynomial fit is performed at each grid node over a local subset of the entire data. Then the best-fit polynomial at the centre point of the subset is back-calculated to give the regional. Chandler et al. (1981) have used the term 'moving window' to describe this technique.

It is assumed that the data, denoted $z(x_i, y_j)$, have been acquired on a rectangular grid with spatial dimension $m\Delta x$ by $p\Delta y$ where Δx and Δy are the grid intervals in the x and y directions. In addition, the task is simplified if the moving window is defined by the interval $\{x_{i-w}, y_{j-w}\}$ through $\{x_{i+w}, y_{j+w}\}$, where $i = 1,2,...,m$, $j = 1,2,...,p$, $w = 1,2,...,2k+1$, $k \leq (m-1)/2$ and $k \leq (p-1)/2$.

If $Z(x,y)$ represents the polynomial that best fits the data in the window, then it has the form of equation 2.1a or b. The distinction between equations 2.1a and 2.1b is not important for this derivation because it applies equally to both polynomials, and again the limits of summation will be omitted.

The coefficients a_{rs} can be determined by minimization of the mean square error, E, of the best-fit polynomial, $Z(x,y)$, relative to the observed data $z(x,y)$,

$$E = \sum_{t=i-w}^{i+w} \sum_{u=j-w}^{j+w} \{Z(x_t,y_u)-z(x_t,y_u)\}^2. \tag{2.4}$$

Setting $(n+1)(n+2)/2$ partial derivatives equal to 0 (for polynomials of the form of equation 2.1a) or $(n+1)(n+2)/2 + n(n+1)/2$ $(=(n+1)^2)$ partial derivatives equal to 0 (for polynomials of the form of equation 2.1b) invokes the least-squares condition, i.e.,

$$\frac{\partial E}{\partial a_{rs}} = 0, \qquad (2.5)$$

for all $r+s=0,1,2,...n$

or $r=0,1,2,...n$ and $s=0,1,2,...n$.

This generates either a system of $(n+1)(n+2)/2$ normal equations that can be used to solve for the unknown coefficients of equation 2.1a; or a system of $(n+1)^2$ normal equations that can be used to solve for the unknown coefficients of equation 2.1b.

For both regional and residual calculations, this procedure must be performed at each grid node. If this method is being used to compute a regional, then the output at each grid node is $Z(x_i, y_j)$; and, if it is being used to compute a residual, the output is $z(x_i, y_j) - Z(x_i, y_j)$.

The method of orthogonal polynomials

When using the method of nonorthogonal polynomials one encounters numerical difficulties that arise from inverting a Hilbert matrix (Lapidus, 1962, p. 329). These include: (1) a loss of accuracy due to rounding errors, and (2) computationally intensive algorithms. Because these complications can be avoided by using orthogonal polynomials this, is the preferred approach. Of added importance for this study is the fact that orthogonal polynomials allow local least-squares polynomial separation calculations to be formulated as two-dimensional convolution, thus allowing wavenumber-domain analysis of the filters.

An excellent review of the use of orthogonal polynomials in removing residual

features from data in two independent variables has been given by Hayes (1970).
However in Hayes's discussion, the computational procedure is not stated in terms of a
convolution. Hence, after summarizing the relevant elements of Hayes's review, this
procedure, as well as high-pass filtering, will be shown to be equivalent to
convolution. The derivation is similar to the derivation given by Chan and Leong
(1972) for data in one independent variable.

It is possible to rewrite equations 2.1 in terms of the polynomials $p_{r,s}(x,y)$, that
correspond to the terms $x^r y^s$ in equations 2.1, and which are orthogonal over
summation in the interval defined by the moving window (i.e. in the interval $\{x_{i-l}, y_{j-l}\}$
through $\{x_{i+w}, y_{j+w}\}$. This can be stated as,

$$\sum_{t=i-w}^{i+w} \sum_{u=j-w}^{j+w} p_{a,b}(x_t, y_u)q_{c,d}(x_t, y_u) = 0 \qquad (2.6)$$

$$\text{for } m+n \neq v+w.$$

Because the data are arranged on a regular rectangular grid, orthogonal polynomials in
two independent variables are equivalent to the product of two orthogonal polynomials
in one variable. That is, Hayes (1970) has shown that,

$$p_{rs}(x,y) = p_r(x)q_s(y) \qquad (2.7)$$

$$\text{for } r \leq n, \; s \leq n$$

$$r+s \leq n$$

This is of significant practical importance, because several algorithms have been
developed for rapid generation of orthogonal polynomials in one variable. The most
prevalent method for doing this is the recursive relationship of Forsythe (1957):

$$p_{-1}(x) = 0$$

$$p_0(x) = 1 \tag{2.8}$$

$$p_{r+1}(x) = 2(x - \alpha_{r+1})p_r(x) - \beta_r\, p_{r-1}(x)$$

where

$$\alpha_{r+1} = \frac{\displaystyle\sum_{t=i-w}^{i+w} x_t p_r^2(x_t)}{\displaystyle\sum_{t=i-w}^{i+w} p_r^2(x_t)} \tag{2.9}$$

$$\beta_r = \frac{\displaystyle\sum_{t=i-w}^{i+w} p_r^2(x_t)}{\displaystyle\sum_{t=i-w}^{i+w} p_{r-1}^2(x_t)} . \tag{2.10}$$

Then the best-fit polynomial, from equations 2.1, can be rewritten as:

$$Z(x,y) = \sum_r \sum_s c_{rs}\, p_r(x) q_s(y) \tag{2.11}$$

where the least-squares solution is given by Hayes (1970) as:

$$c_{rs} = \frac{\displaystyle\sum_{t=i-w}^{i+w} \sum_{u=j-w}^{j+w} z(x_t, y_u) p_r(t) q_s(u)}{(\Delta x)^r (\Delta y)^s \displaystyle\sum_{t=i-w}^{i+w} \sum_{u=j-w}^{j+w} p_r^2(t) q_s^2(u)} . \tag{2.12}$$

Substituting equation 2.12 into equation 2.11 and rearranging the order of summation gives:

$$Z(x,y) = \sum_{t=i-w}^{i+w} \sum_{u=j-w}^{j+w} \sum_{r} \sum_{s} \frac{p_r(x)q_s(y)z(x_t,y_u)p_r(t)q_s(u)}{(\Delta x)^r (\Delta y)^s \sum_{t=i-w}^{i+w} \sum_{u=j-w}^{j+w} p_r^2(t)q_s^2(u)}. \qquad (2.13)$$

Evaluating equation 2.13 at $x=x_i$ and $y=y_j$ gives an expression for the best-fit polynomial at the centre of the moving window representing the long-wavelength, or regional, component:

$$Z_{reg}(x_i,y_j) = \sum_{t=-\infty}^{\infty} \sum_{u=-\infty}^{\infty} b_{tu}\, z(x_{i-t},y_{j-u}) \qquad (2.14)$$

where b_{tu} is zero, except in the interval $i-w \leq t \leq i+w$ and $j-w \leq u \leq j+w$, within which:

$$b_{tu} = \sum_{r} \sum_{s} \frac{p_r(0)p_r(t)q_s(0)q_s(u)}{\sum_{t=-w}^{w} \sum_{u=-w}^{w} p_r^2(t)q_s^2(u)}. \qquad (2.15)$$

The calculation described by equation 2.14 is a two-dimensional convolution, and hence equation 2.15 gives the expression for the space-domain operator for low-pass filtering of data in two variables.

An expression can be derived for the high-pass filters. The outputs of which are the short-wavelength or residual component, denoted $Z_{res}(x_i,y_j)$, is $z(x_i,y_j) - Z_{reg}(x_i,y_j)$. Then, using the expression for Z_{reg} from equation 2.14 gives:

$$Z_{res}(x_i, y_j) = z(x_i, y_j) - \sum_{t=-\infty}^{\infty} \sum_{u=-\infty}^{\infty} b_{tu} \; z(x_t, y_u). \tag{2.16}$$

This can also be formulated in terms of two-dimensional convolution as:

$$Z_{res}(x_i, y_j) = \sum_{t=-\infty}^{\infty} \sum_{u=-\infty}^{\infty} c_{tu} \; z(x_{i-t}, y_{j-u}) \tag{2.17}$$

where c_{tu} is given by

$$c_{tu} = \delta_{ti} \delta_{uj} - b_{tu} \tag{2.18}$$

in which δ_{ti} and δ_{uj} are Kronecker deltas, and b_{tu} is given by equation 2.15. Equation 2.18 gives the expression for the space-domain operator for high-pass filters in two independent variables.

Equation 2.14 and 2.17 indicate that these local least-squares weight functions are non-recursive. Thus these can be classified as finite impulse response filters. The significance of this will be explored later.

Properties of least-squares filters

At this point it is appropriate to discuss some properties of local least-squares filters that are revealed by the convolution formulation, as these have implications for both space-domain and frequency-domain computations. These properties apply to weight functions derived from polynomials given by both equation 2.1a and 2.1b. They are:

(1) Filters for polynomial orders n and $n+1$ (where $n = 0,2,4,...$) are identical for a given window size. This is because orthogonal polynomials of even orders are

even functions, and orthogonal polynomials of odd orders are odd functions. That is, from equation 2.9,

$$p_r(x) = p_r(-x) \text{ if } r \text{ is even}$$
$$p_r(x) = -p_r(-x) \text{ if } r \text{ is odd}$$

(2.19)

Thus over the symmetric interval defined by the moving window, odd powers of $p_r(0)$ and $q_s(0)$ are identical to zero, and hence the odd orthogonal polynomials do not contribute to the operator coefficients. This is consistent with one-dimensional low-pass filters (Wood and Hockens, 1970). An implication of this is that the convolution operators are even functions. This is important, because it suggests the filters are phase-distortionless, a necessary property of separation filters for potential-field data (Syberg, 1972; Jacobsen, 1987).

(2) The polynomial order may not exceed the size of the window, where window size is defined as the number of data points along one side of the window. This is because the sum of the squares of orthogonal polynomials can be written as (Wylie, 1960),

$$\sum_{-w}^{w} p_r^2(t) = \frac{(2w+2+r)^{(l+1)}}{(2r+1)(2w+1)^{(l)}},$$

(2.20)

where the exponents in parenthesis represent factorial polynomials, for example

$$(x)^{(n)} = x(x-1) \cdot \cdot \cdot (x-n+1).$$

(2.21)

Thus, the impulse response of local least-squares polynomial filters is undefined if the polynomial order is equal to or greater than the window size. For nonorthogonal polynomials this property manifests itself as an under-determined problem. In fact, if

the window size is equal to, or one less than the polynomial order and the formulation given by equation 2.1b is used, low-pass filters become all-pass filters, and high-pass filters become all-reject filters. This implies that the highest polynomial order that may be used for square windows containing an odd number of grid nodes per side, and polynomials of the form of equation 2.1b, is two less than the number of nodes of one side of the window.

(3) Low-pass filtering with a polynomial order of 0 or 1 is equivalent to computing an average within the window. This may be accounted for by considering the following features of orthogonal polynomials: equation 2.9 indicates that zero-order polynomials are always equal to 1 and equation 2.20 indicates that the sum of the square of zero-order orthogonal polynomials over the window is equal to the number of nodes in the window. Thus the filter coefficients become:

$$b_{tu} = \frac{1}{2w+1}.$$

(2.22)

These are typically referred to as mean filters (Claerbout and Muir, 1973; Stewart, 1985). Because these are special cases of local least-squares polynomial filters, it is possible to design more flexible filters that exhibit the same characteristics.

Some important considerations which are not obvious when nonorthogonal polynomials are used are unveiled by reformulating this technique as a convolution. To understand fully the nature of these filters, the wavenumber-domain responses for selected values of the window size and polynomial order will be examined.

Wavenumber-domain response of local least-squares filters

The objectives of the study of the filtering characteristics of local least-squares filters are fourfold. These are: to determine which of the two polynomial types specified by equations 2.1 generates a superior amplitude spectrum; to demonstrate the low-pass, and high-pass nature of the transfer functions and comment on the relevant features; to illustrate the dependence of passband on window size and polynomial order, and to quantify the filtering characteristics.

Transfer functions have been obtained by computing discrete Fourier transforms of the impulse responses. Because the impulse responses are real and even, their Fourier transforms are in turn real and even. Thus it is necessary to compute only the real part of the Fourier transform and to display only the first quadrant of the spectra. Because these are phase-invariant filters, phase spectra are not shown. Amplitude spectra are computed using a unit sampling interval for frequencies from zero to the Nyquist frequency.

Shown in figure 2.1 are the amplitude responses of low-pass filters computed using a 5x5 window and second-order polynomials specified respectively by equations 2.1a and b. Examination of spectra computed using several window sizes and polynomial orders indicates that these are representative examples. The transfer function generated when the approximating function is given by 2.1b is more reliable than the transfer function given by 2.1a. This is based on the fact that both filters pass the same frequencies parallel to the axes; however, figure 2.1b more closely resembles an ideal low-pass filter. On the other hand, the spectrum shown in figure 2.1a does not
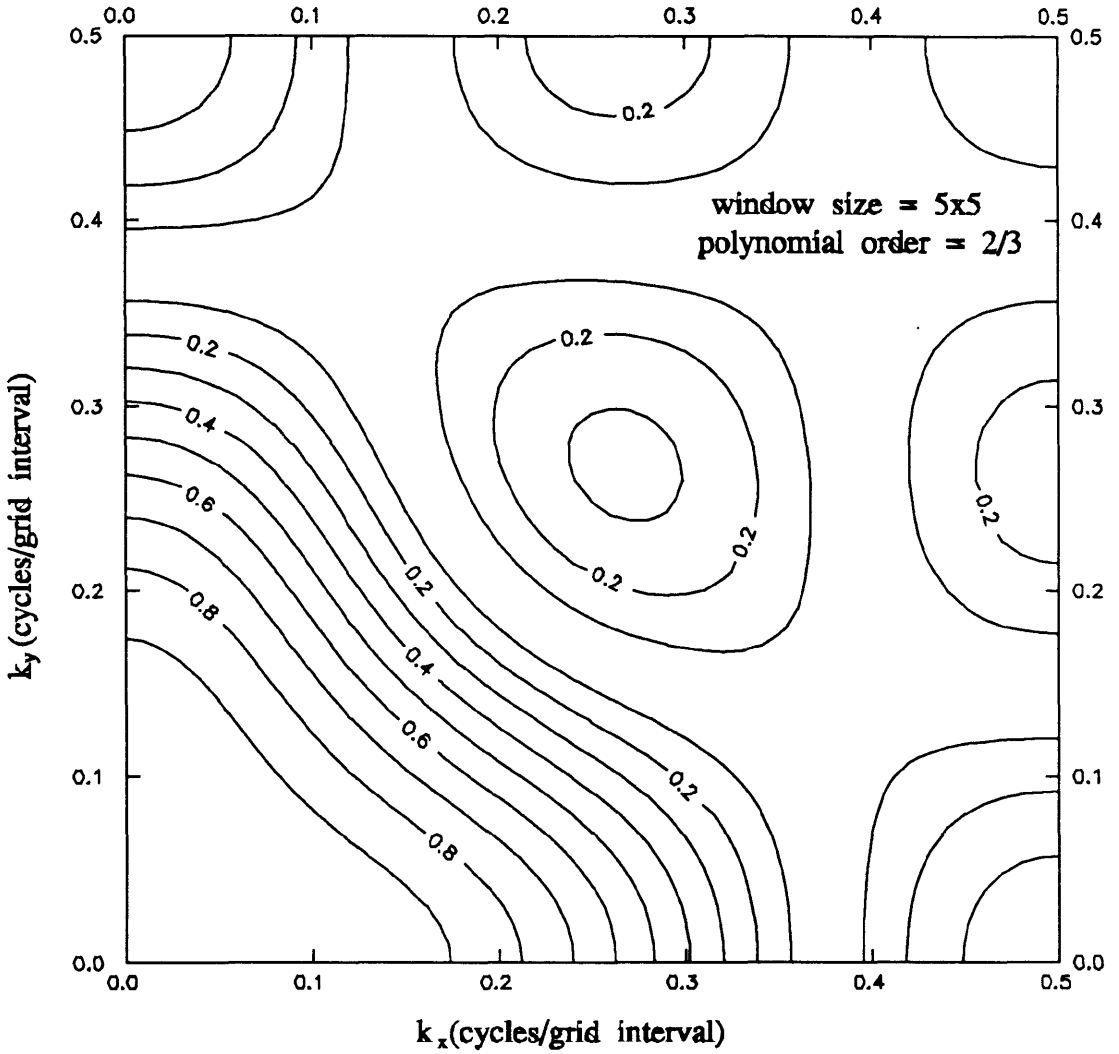
(a)

Figure 2.1 Transfer function of a low-pass filter computed using a 5x5 window and a second- or third-order polynomial of the form of equation 2.1a (a) and b (b).
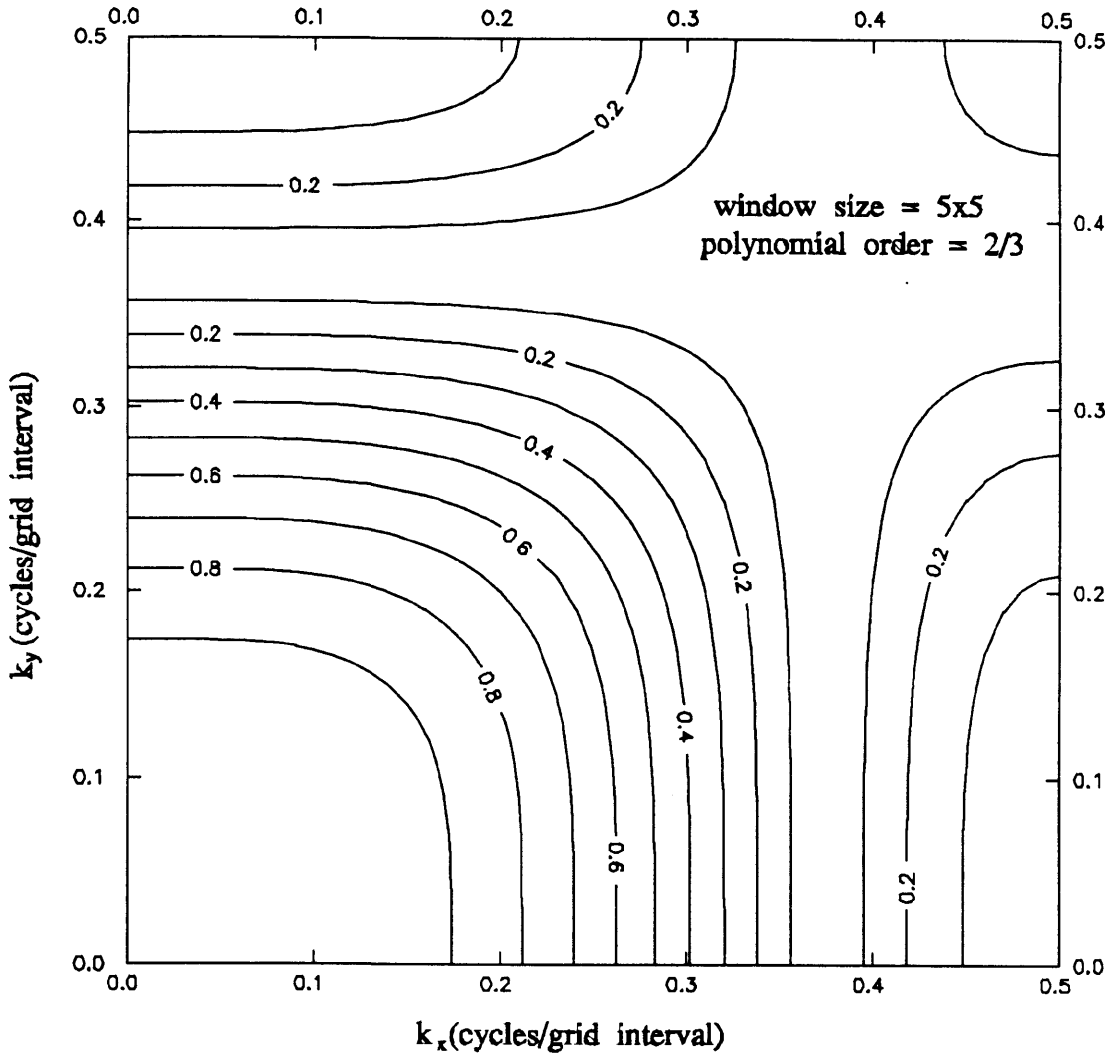
(b)

exhibit reliable filtering characteristics. Of significance is the prevalent directional distortion. That is, the passband is considerably narrower along $k_x = k_y$ than it is along k_x or $k_y = 0$. This would cause considerable spatial dependence in the frequency content of the filtered data. In figure 2.1b the directional dependence is much less severe, and will be addressed later. The conclusion that can be drawn from this is that for local least-squares polynomial filters, the approximating function should conform to the type described by equation 2.1b. Hence, all further discussion is restricted to weight functions based on these polynomials.

Figure 2.1b exhibits the general properties of these filters. This weight function passes virtually all frequencies; however, outside the passband the signal is effectively removed. The low-pass filters display a gentle decrease in amplitude with increasing wavenumber in the passband. This rate of attenuation increases in the roll-off region and decreases in the reject region. In the reject region there are a number of side lobes of negligible magnitude.

As mentioned previously, figure 2.1b indicates that there is some directional distortion induced by these filters. That is, along $k_x = k_y$ the axis defined by passband is widest; and in the directions of the coordinate axes the passband is narrowest. Because the Fourier transform preserves signal directivity (Fuller, 1967) for a coordinate system in which y is positive to the north and x is positive to the east, the high-frequency content will be reduced in the north-south and east-west directions compared to the northwest-southeast and northeast-southwest directions. It would be possible to alter the orientation of this directional dependence by rotating the space-

domain coordinate axes.

The spectrum in figure 2.1b shows that the amplitude spectrum is symmetric

about the axis defined by $k_x = k_y$, and thus these filters do not bias signal

corresponding to either one of the coordinate axes. This is because orders of x and y

are equally represented by the approximating polynomial. If this were not the case

then the frequency content would be increased along the frequency axis corresponding

to the spatial variable with the higher order. For example, figure 2.2 shows a filter for

a 7x7 window, and an approximating function given by:

$$P_{mn}(x,y) = \sum_{r=0}^{2} \sum_{s=0}^{4} a_{rs} x^r y^s.$$
(2.23)

That is, the terms containing orders of x higher than two have been omitted. In some

cases *a priori* information justifies enhancement of signal in a specified orientation

(Fuller, 1967; Peeples et al., 1986; Thorarinsson et al., 1988); however, in general,

introducing artifacts of this nature should be avoided.

From equations 2.14, 2.17, and 2.18 it can be seen that the amplitude responses

of high-pass filters are similar to those of the corresponding low-pass filters, with the

exception that the values of the amplitude spectrum are obtained by subtracting from

1. Thus the discussion of the transfer functions of low-pass filters is equally applicable

to high-pass filters.

For low-pass filters, one would expect the width of the passband to be

proportional to polynomial order and inversely proportional to window size (Thurston

et al., 1990). Computation of the amplitude responses confirms this result. Shown in
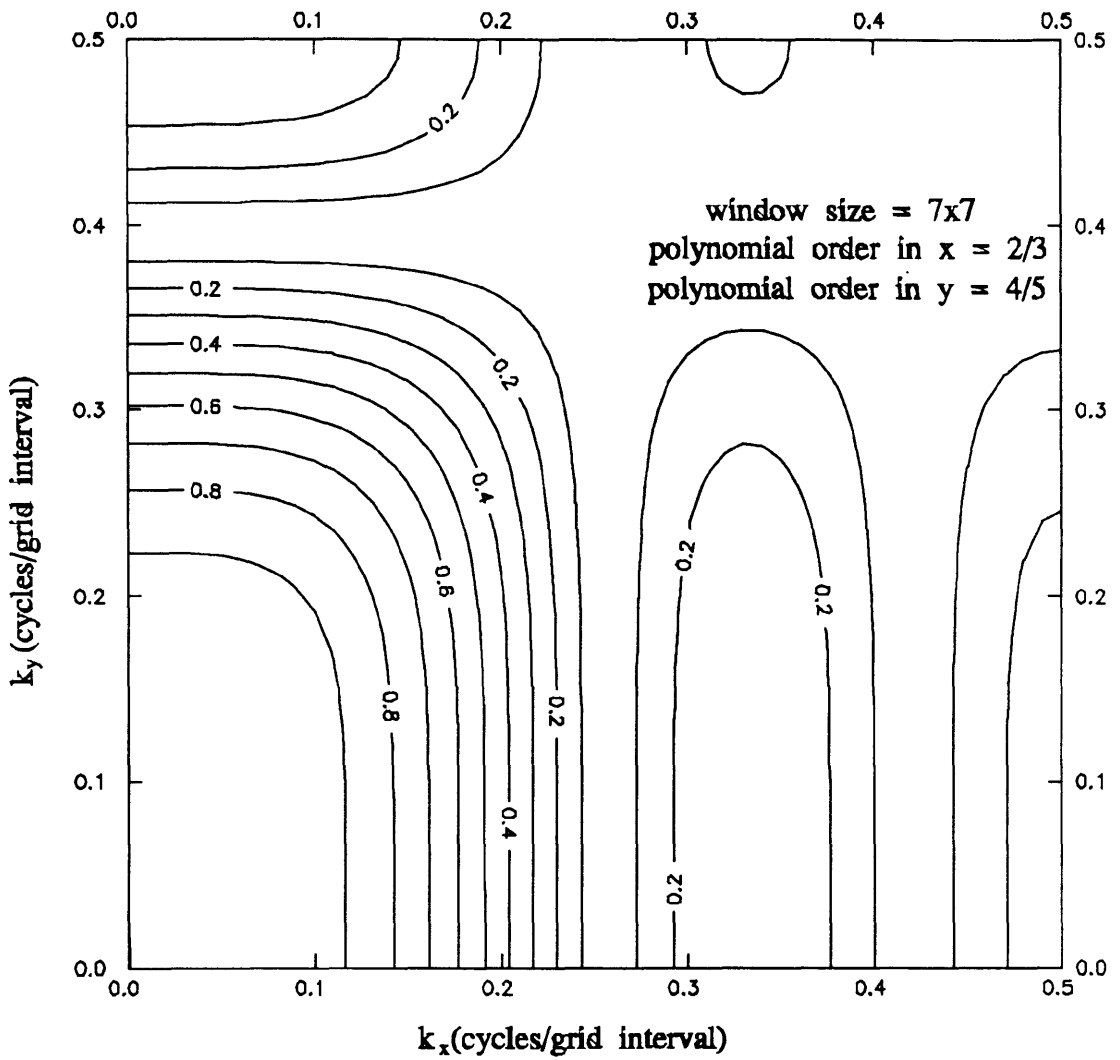
Figure 2.2. Orientation-dependent low-pass filter. Signal in the k_y direction is biased.

figures 2.3 is the suite of all possible filters that may be generated for a 9x9 window. Increasing the polynomial order increases the cutoff wavenumber of the filter. As well, these spectra demonstrate that the directional distortion increases for increasing polynomial order. That is, in figure 2.3a the passband is very nearly circular, while in figure 2.3c the passband is considerably more rectangular. Figures 2.1b, 2.3b, and 2.4 demonstrate the influence of window size on passband. These confirm that increasing the window size decreases the passband. In addition, increasing the passband increases the slope of the roll-off region. It is also important to note that the directional dependence increases with decreasing window size, although the effect is less significant than was observed for comparable changes in polynomial order.

The dependence of passband width on polynomial order and window size has been quantified. This was accomplished by measuring the passband for varying values of order and window size. This entailed determining the frequency corresponding to an amplitude decrease of 3dB. Because high-pass filters are derived from low-pass filters, it is necessary to do this only for low-pass filters. This was done by computing the discrete Fourier transform at increments of 0.001 cycles per grid interval, and determining the frequency at which the amplitude spectrum is 0.707 of the value at zero wavenumber. This method determines the passband to within ±0.0005 cycles per grid interval. In order to account for the directional dependence, the passbands were determined for their narrowest orientations (along the k_x or k_y axis), and along their widest orientations (along k_x equal to k_y).
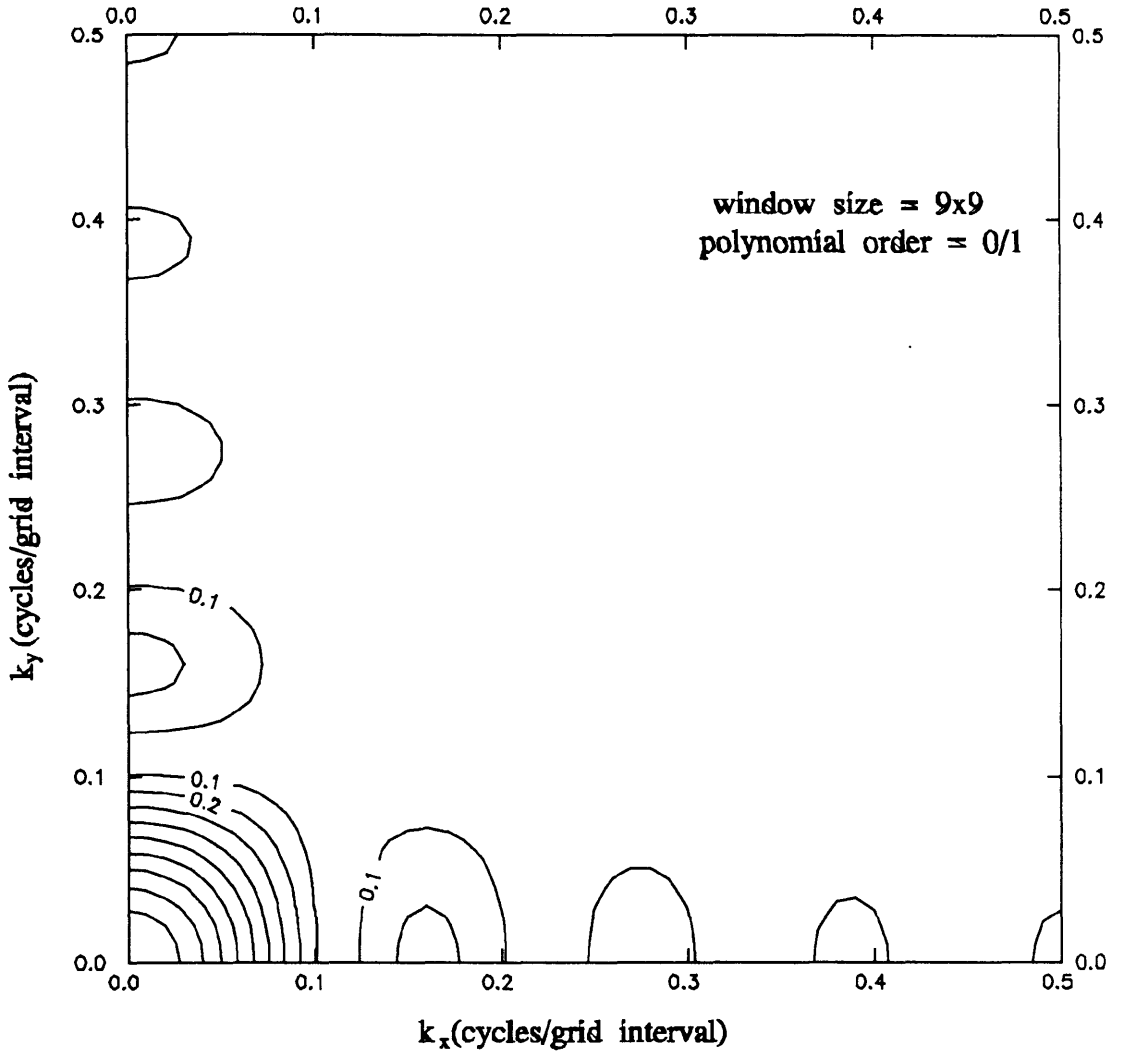
(a)

Figure 2.3a-d. Amplitude spectra of low-pass filters for a 9x9 window and polynomial orders ranging from 0 to 6. These are all the polynomial orders that may be used for a 9x9 window.

window size = 9x9
polynomial order = 2/3

(b)

window size = 9x9
polynomial order = 4/5

(c)

window size = 9x9
polynomial order = 6/7
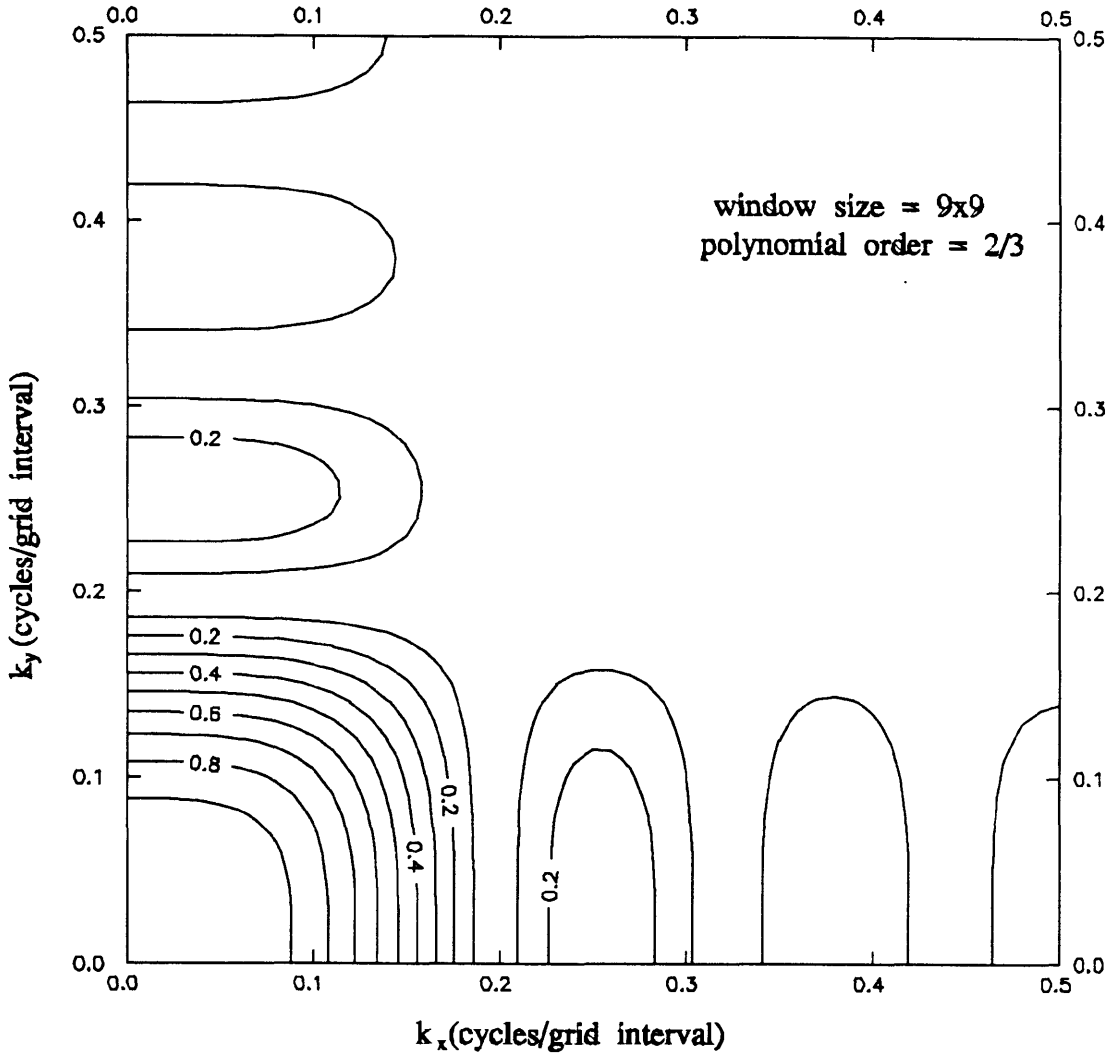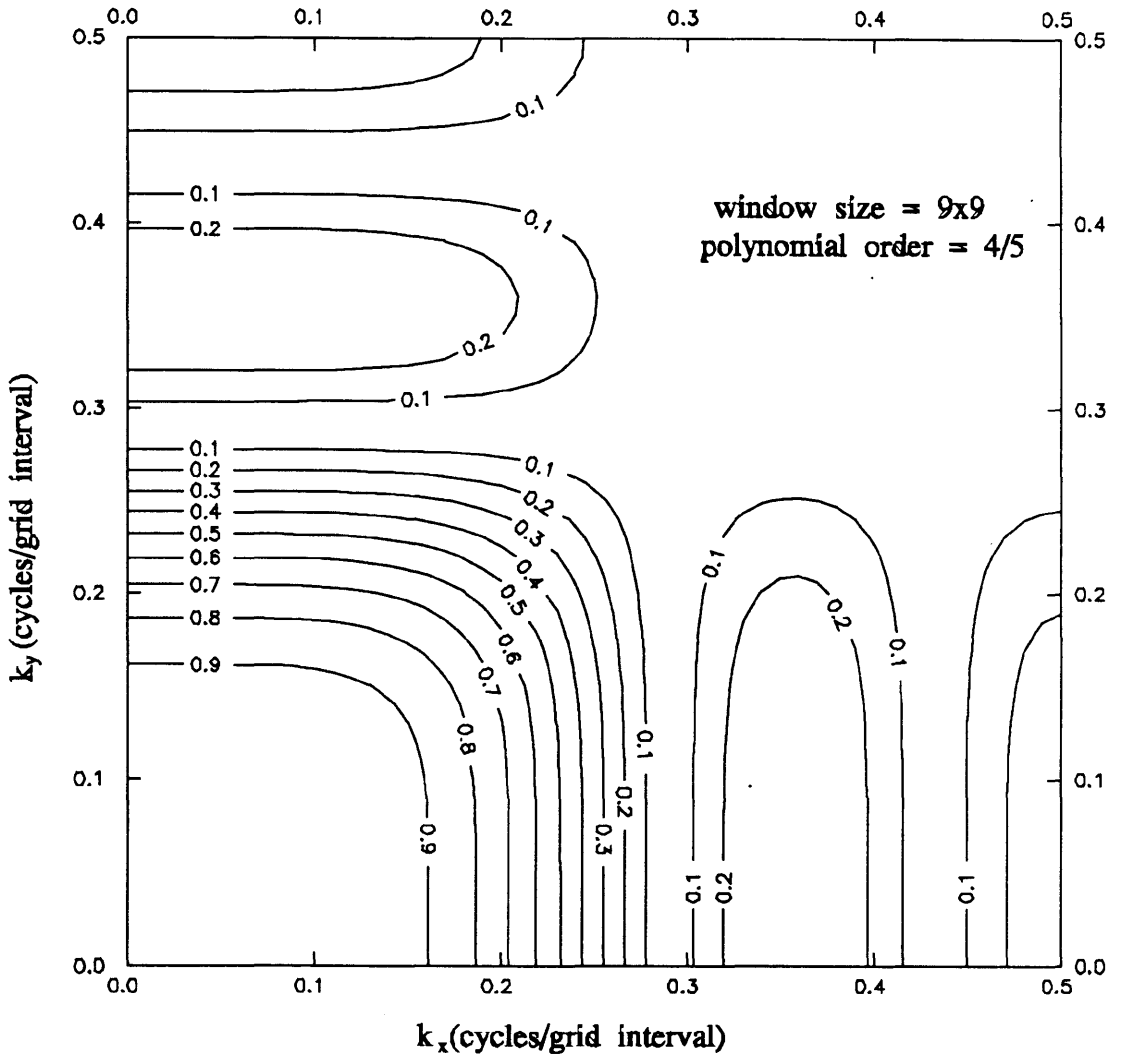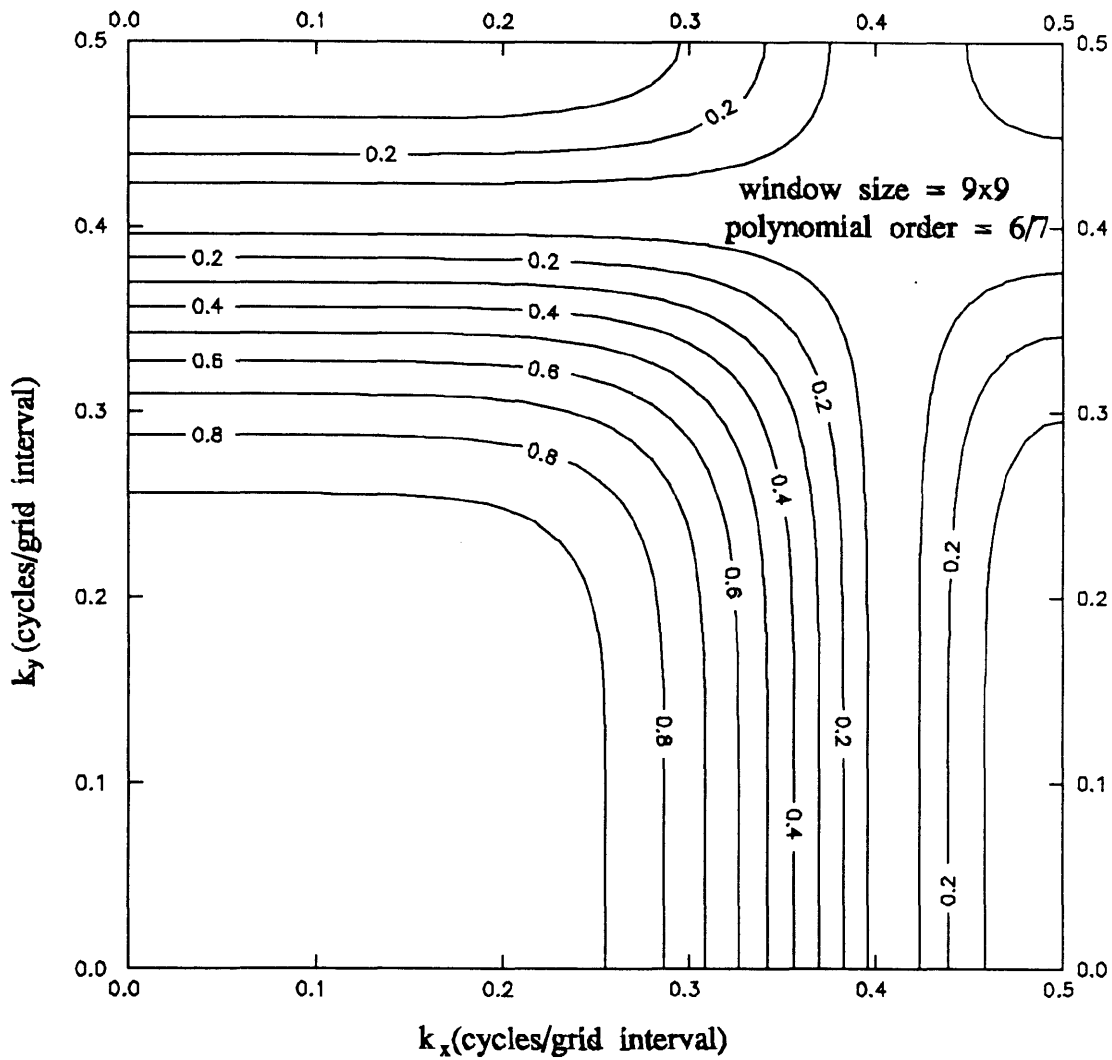
(d)
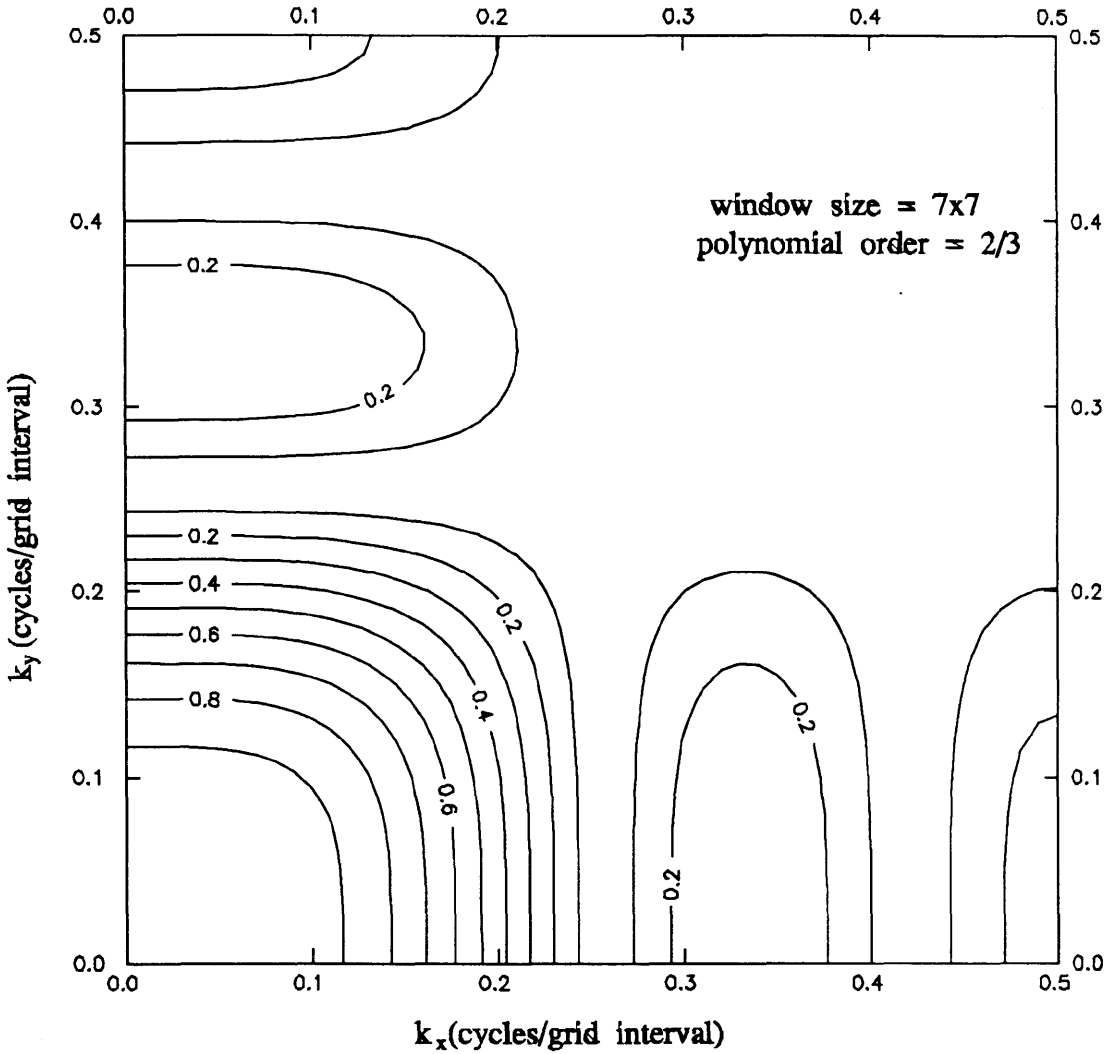
Figure 2.4. Amplitude spectrum of a filter computed using a 7x7 window and a second-order polynomial.

The Fourier transform along the k_x axis (that is for $k_y = 0$) is given by:

$$B(k_x, 0) = \sum_{t=-l}^{l} \sum_{u=-l}^{l} b_{tu} e^{-i2\pi t \Delta x k_x}. \qquad (2.24)$$

Substituting the expression for b_{mn} into equation 2.24, and separating the summation yields:

$$B(k_x, 0) = \sum_{t=-w}^{w} \sum_{r=0}^{n} \frac{p_r(0)p_r(t)}{\sum_{t=-l}^{l} p_r^2(t)} e^{-i2\pi t \Delta x k_x}$$
$$\cdot \left[\sum_{u=-w}^{w} \sum_{s=0}^{n} \frac{q_s(0)q_s(u)}{\sum_{u=-l}^{l} q_s^2(u)} \right]. \qquad (2.25)$$

The second double summation in equation 2.25 is equal to 1, and thus the discrete Fourier transform along the k_x axis is identical to the one-dimensional transform given by Chan and Leong (1972). Hence the results of the passband measurements along the k_x axis are identical to the results given in Chan and Leong's paper. The same argument could have been made for the k_y axis. Shown in figures 2.5 are the results of the quantitative study of the passband. Besides giving numerical results of the maximum and minimum frequency content to be expected, figure 2.5 also illustrates some important properties of these filters. First of all, it is difficult to change the passband significantly when the window size is large. Conversely, when the window size is small, the passband is sensitive to changes in window size. In addition, comparison of figures 2.5a and 2.5b quantifies the previously observed phenomena of increase in directional dependence for increasing polynomial order and decreasing
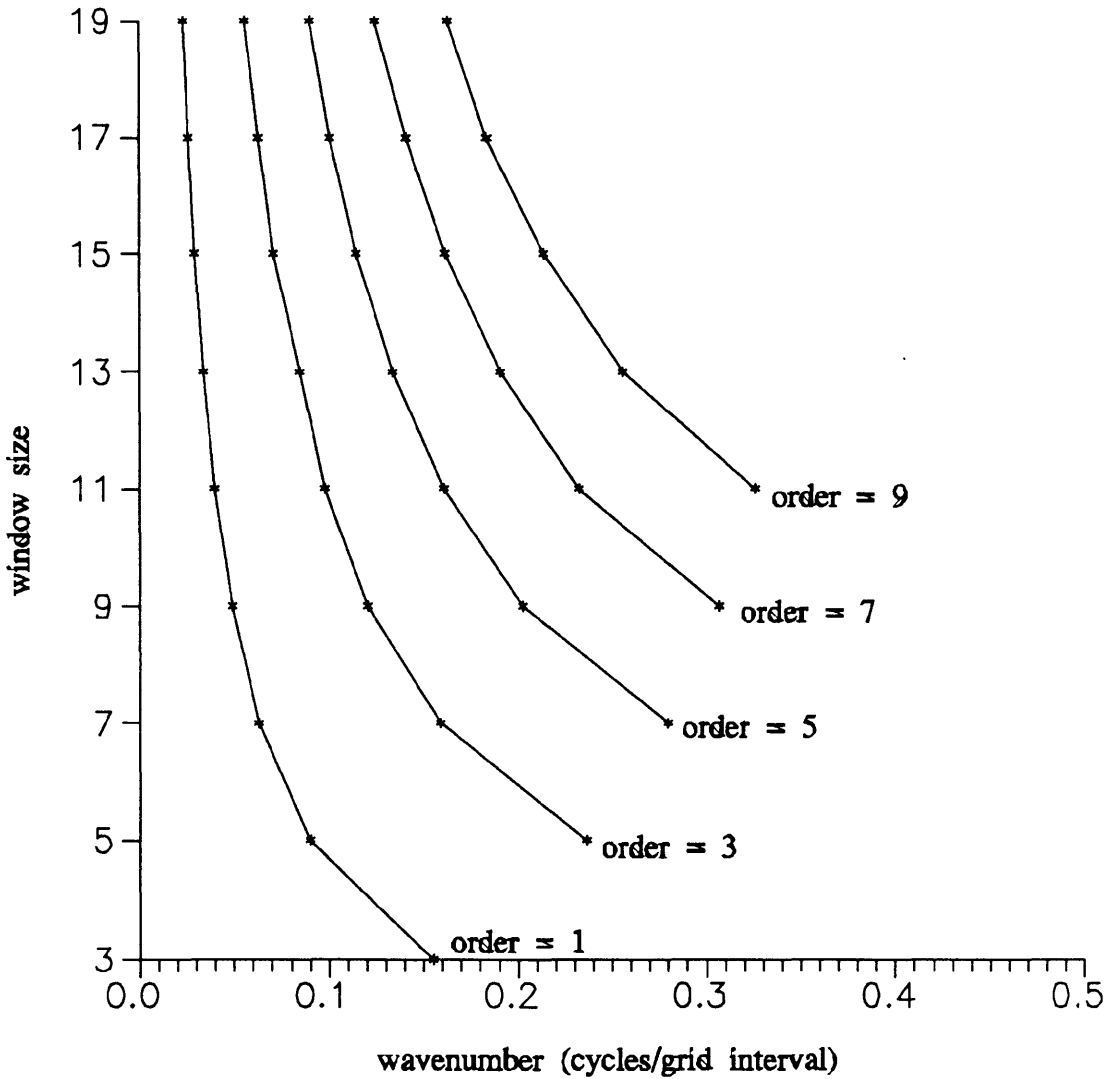
(a)

Figure 2.5. Bandwidth of low-pass filters as a function of polynomial order and window size measured along the frequency-domain axes (a), and at 45° to the axes (b).
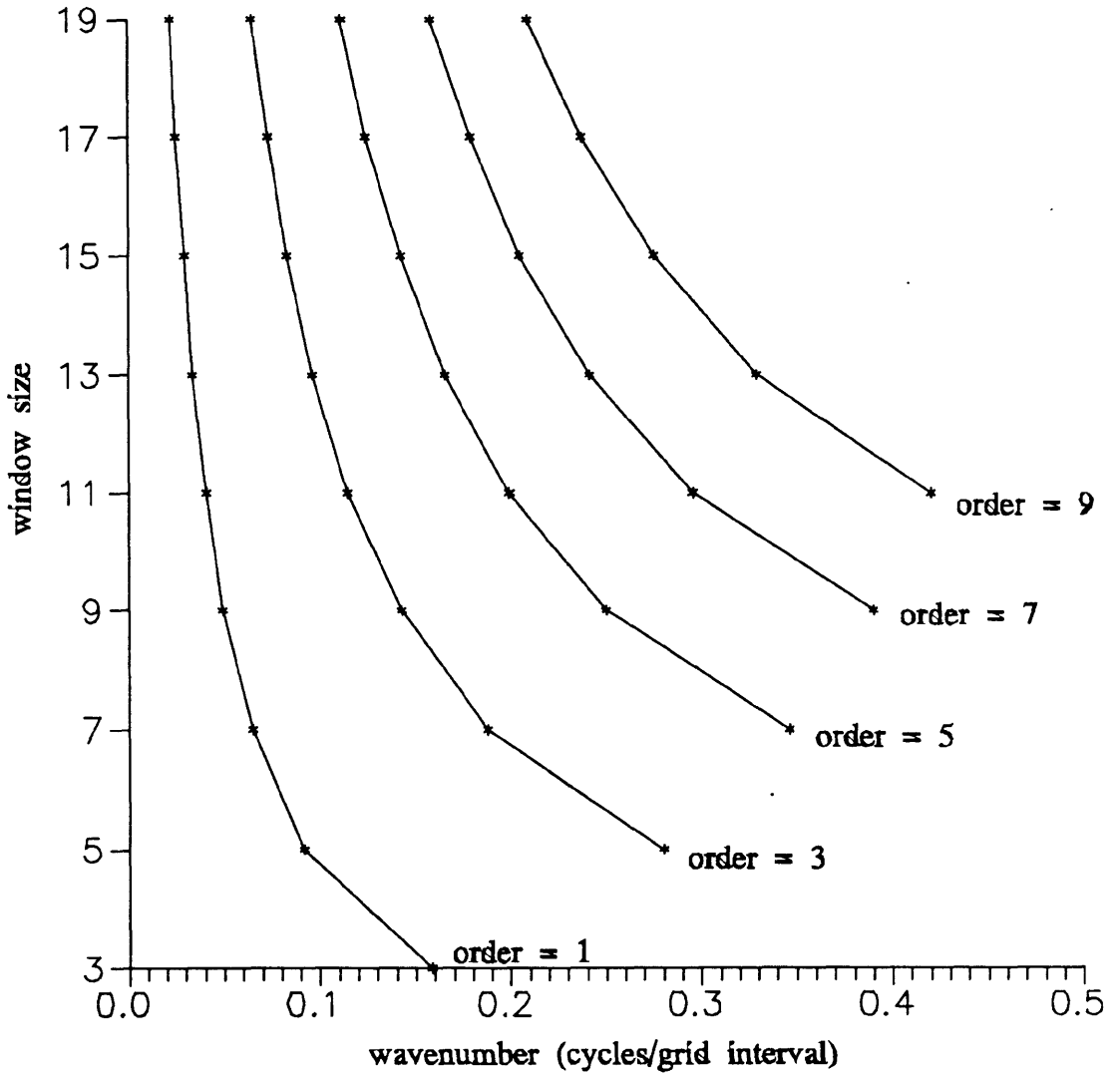
(b)

window size. This is an important criterion for selecting window size and polynomial order for obtaining the desired filtering effects. For instance, from figure 2.5a it is clear that a weight function based on an 11x11 window and a fifth-order polynomial, and a 7x7 window and a third-order polynomial have very nearly the same passband. However figure 2.5b indicates that the 7x7 filter is superior because there is less directional distortion. In general, directional distortion increases with increasing window sizes, and thus these should be kept as small as possible.

Because wavelength may be more intuitively meaningful than wavenumber, it often is used when specifying filtering parameters. For this reason these data have been replotted versus wavelength. This is shown in figures 2.6. A first-order least-squares best-fit line for each order has been calculated. It is interesting to note the linear relationship between cutoff wavelength and window size. It is straightforward to use figures 2.6 as a guide for designing low-pass and high-pass filters.

Implications for global polynomial approximation

Lance (1982) derived a space-dependent convolution form for global least-squares polynomial fitting in order to study the filtering characteristics of this regional/residual separation technique. The formula given for the coefficients of the weight function is:
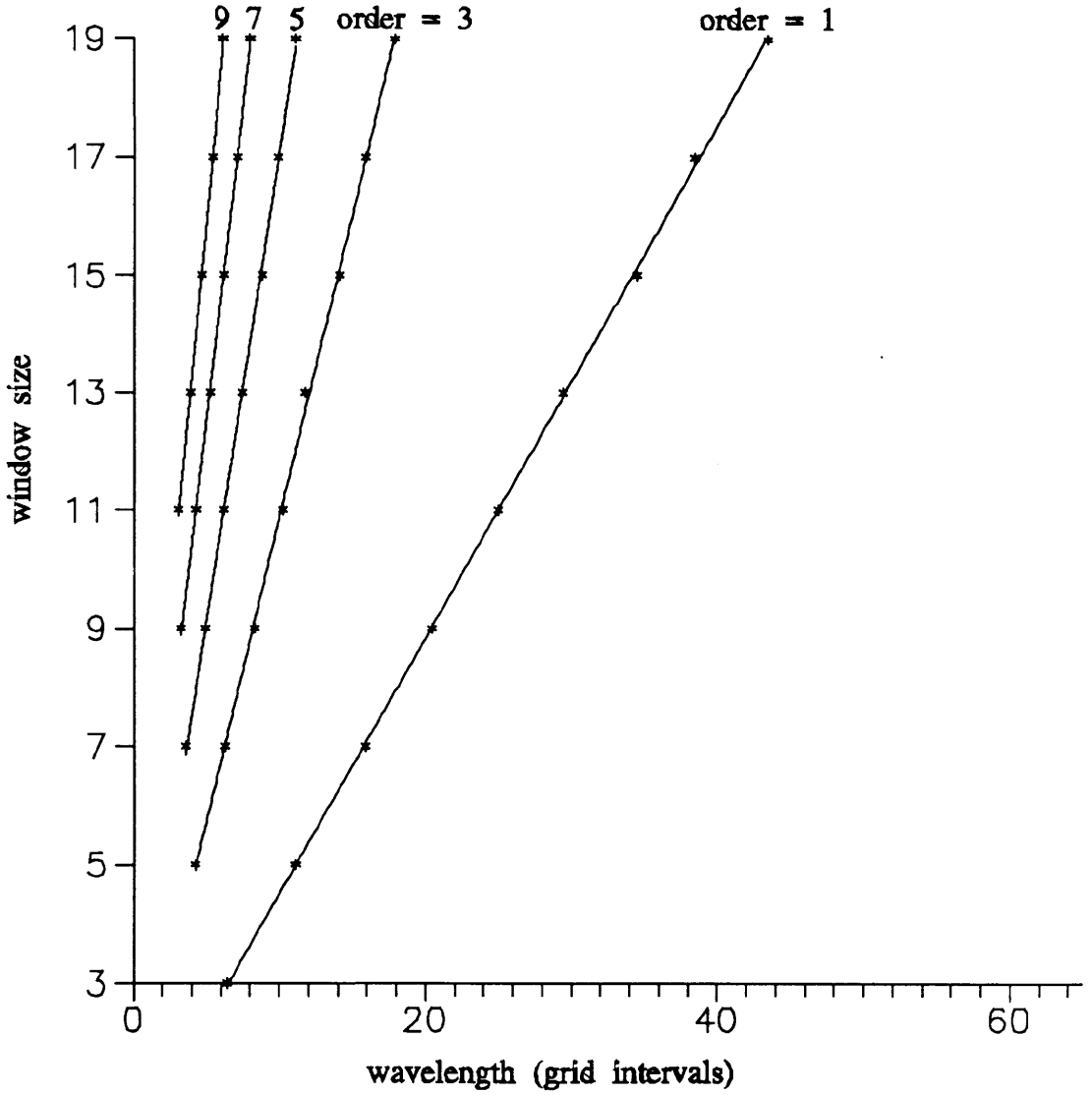
(a)

Figure 2.6a. Cutoff wavelengths (a) along the frequency axes, and (b) along $k_x=k_y$. A first-order best-fit line has been computed for each polynomial order.
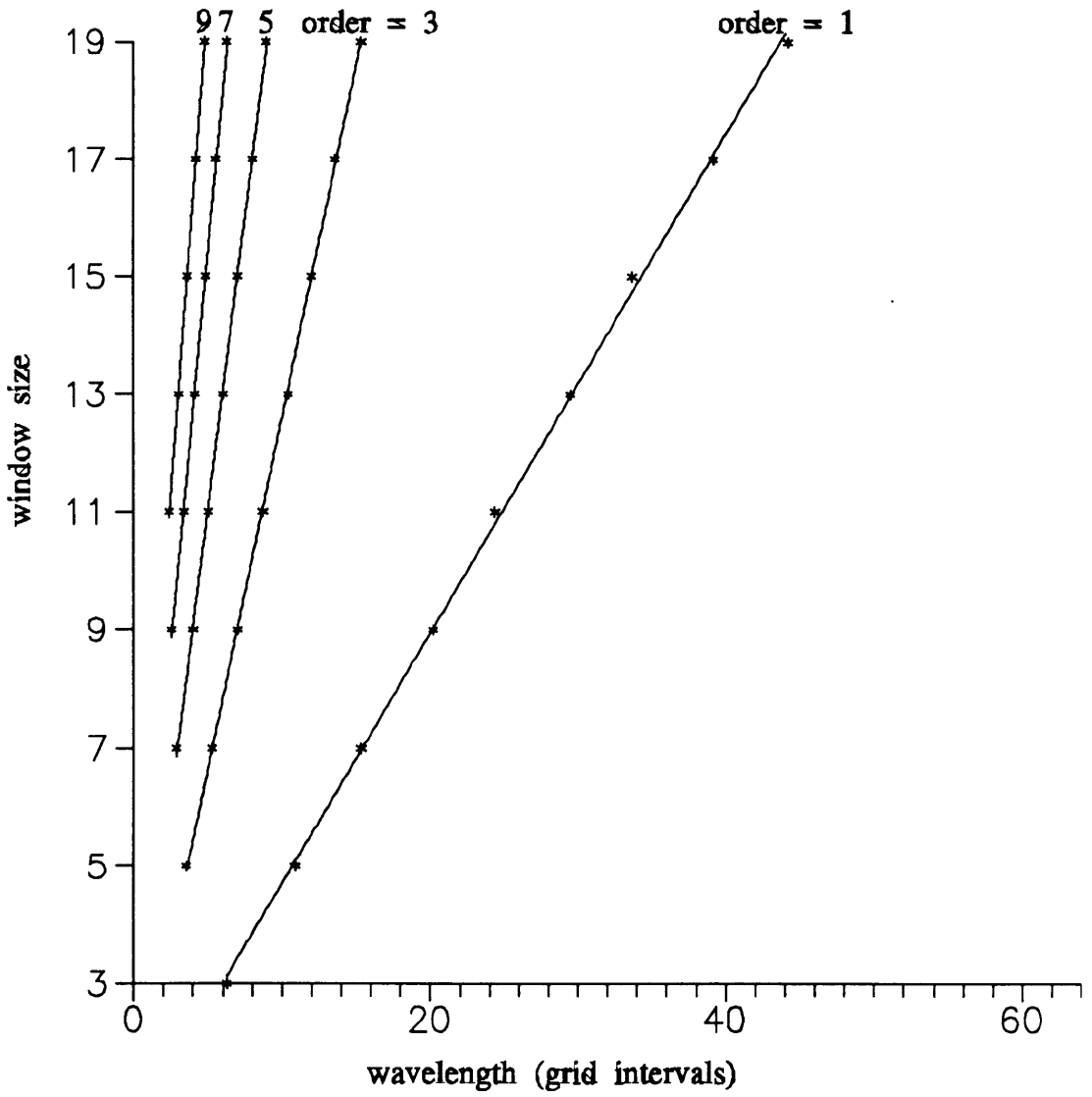
(b)

$$d_{tu}(i,j) = \sum_{r=0}^{o} \sum_{s=0}^{m-r} \frac{p_r(i\Delta x)p_r(t\Delta x)q_s(j\Delta y)q_s(u\Delta y)}{\sum_{t=1}^{m} \sum_{u=1}^{n} p_r^2(t\Delta x)q_s^2(u\Delta y)}$$ (2.26)

where the convolution is described by:

$$Z_{reg}(x_i,y_j) = \sum_{t=-\infty}^{\infty} \sum_{u=-\infty}^{\infty} d_{tu} \, z(x_{i-t},y_{j-u}).$$ (2.27)

Lance (1982) describes this as a shift-variant operation, with each sample in the output filtered by a unique operator. When i and j are equal to zero, the impulse response given by equation 2.26 is identical to the impulse response given by equation 2.15. Thus, the global least-squares weight function that operates on the centre value is a local least-squares filter, whose window size is equal to the size of the data set.

Because local least-squares polynomial filtering is a special case of global least-squares polynomial regional/residual separation, the preceding analysis has implications concerning the terms that should be included in the approximating polynomial. The expression presented by Lance (1982) is based on polynomials of the form of equation 2.1a, and a similar expression can be obtained for polynomials of the form of equation 2.1b by changing the upper limits of the summation in equation 2.26. Hence, figures 2.1a and 2.1b represent centre filters for 5x5 data sets approximated by second-order polynomials that are given by equations 2.1a and b respectively. This suggests that the centre filter has a more reliable low-pass character if polynomials of the form of equation 2.1b are used in place of polynomials of the form of equation 2.1a. This assertion can be extended to operators associated with other grid locations.

Study of such filters is complicated by the fact that they introduce phase distortion. Hence both amplitude and phase spectra must be studied when evaluating the performance of these filters. Examples of these spectra are shown in figures 2.7 and 2.8 for 5x5 windows and second-order polynomials. The phase spectra are essentially equivalent; however, the low-pass filter based on polynomials given by equation 2.1b has a superior amplitude spectrum.

In the literature review at the beginning of this chapter a number of studies that incorporate global least-squares polynomial approximation of potential-field data are described. In these studies, both forms of approximating polynomials are used; however none of these articles contains a justification for either polynomial type. The present analysis suggests that more dependable low-pass filtering of the data may be accomplished by using polynomials given by equation 2.1b. This is not surprising, as the latter type contains more degrees of freedom, and can thus better approximate the data. Nevertheless, comparisons between regional fields computed with both polynomials, is reasonable, as frequency content in the direction of the axes is the same. This is demonstrated by computing the Fourier transform of d_{tu}, given by equation 2.26, along the k_x axis, and separating the summation as was done for equation 2.25. This yields:

window size = 5x5
polynomial order = 2/3

(a)
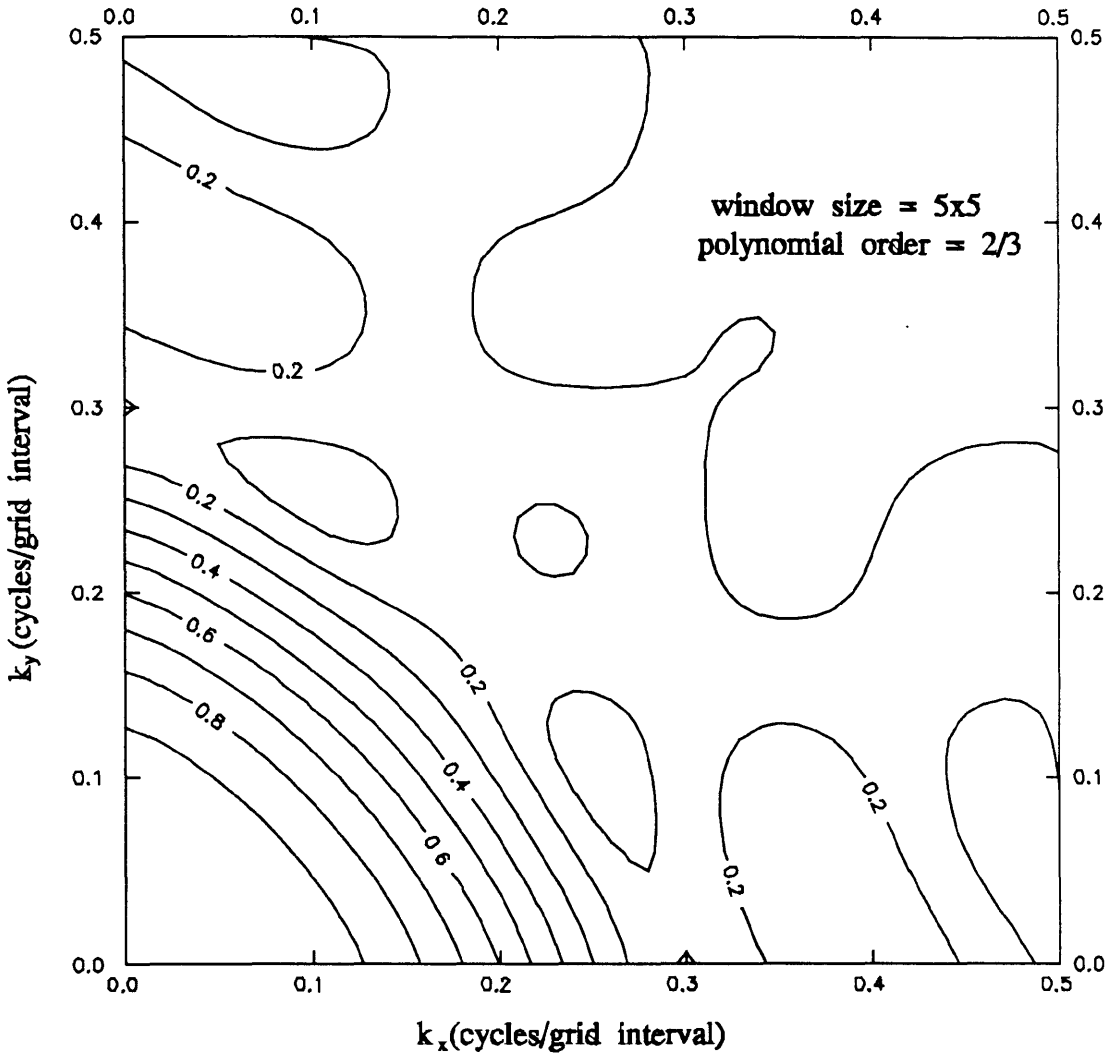
Figure 2.7. Amplitude (a) and phase (b) spectra of the filter based on a second-order polynomial given by equation 2.1a for a 5x5 window and $i = j = 1$.

(b)
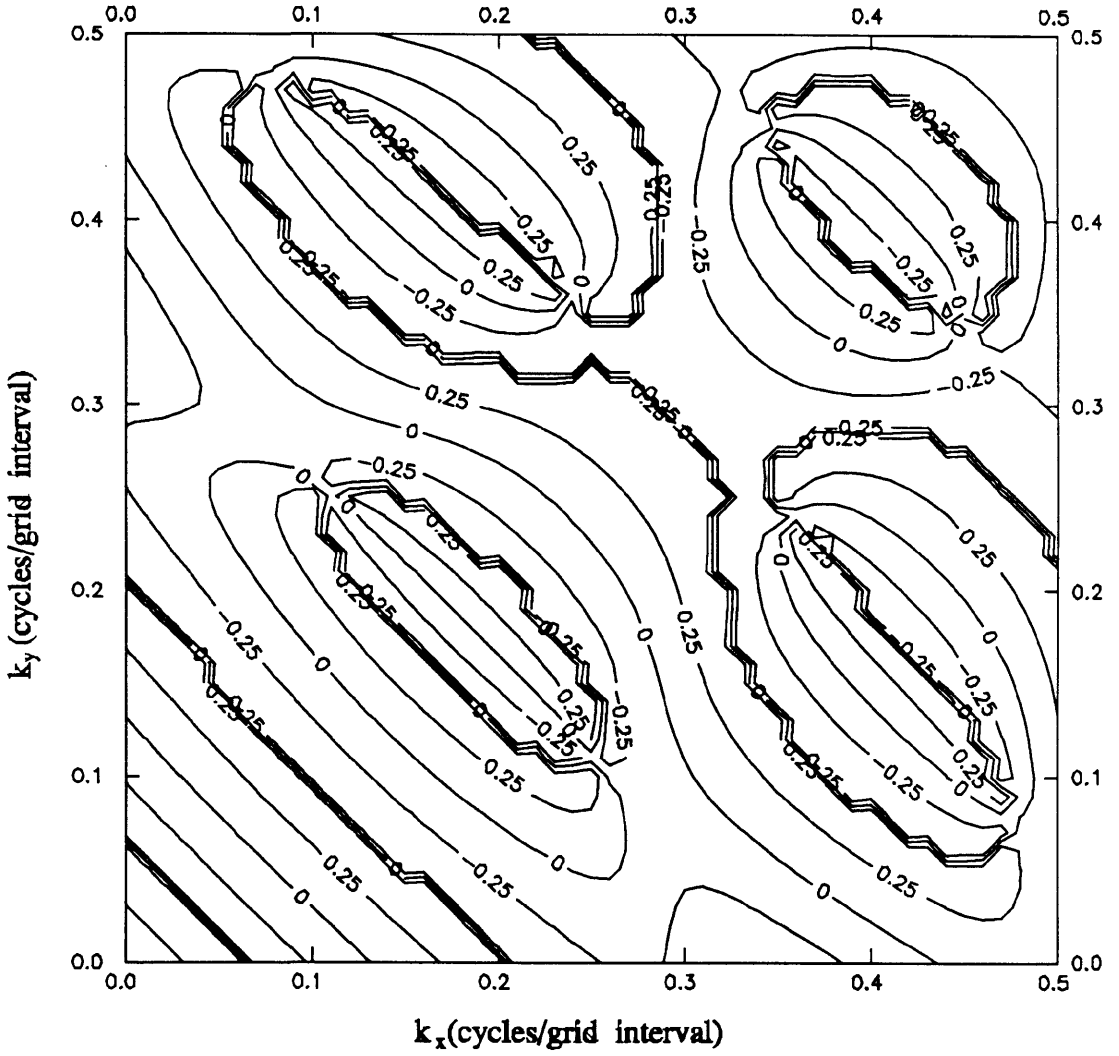
(contour units are π radians, and the interval is $\pi/4$ radians)
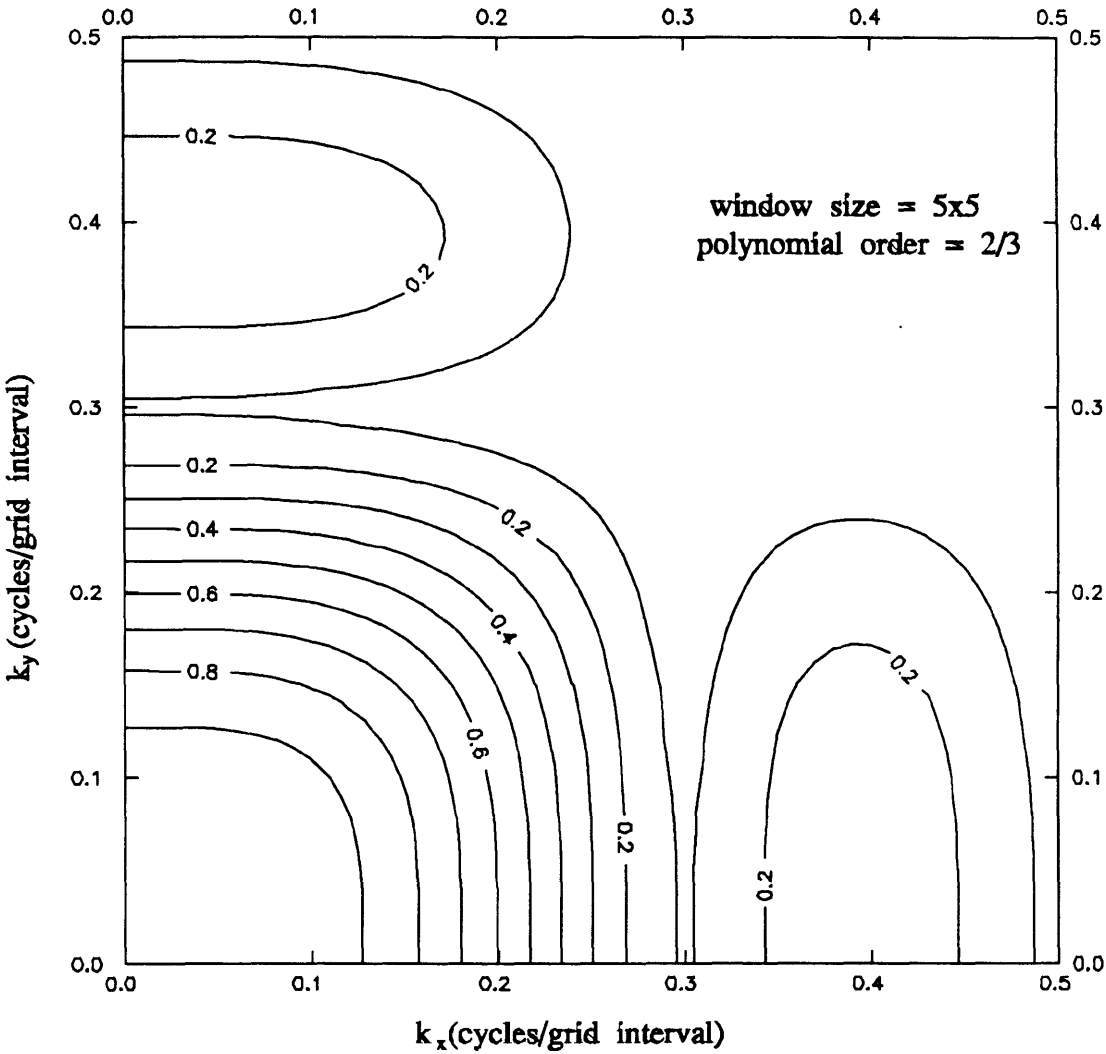
(a)

Figure 2.8. Amplitude (a) and phase (b) spectra of the filter based on a second-order polynomial given by equation 2.1b, for a 5x5 window and $i = j = 1$.

(b)

(contour units are π radians, and the interval is π/4 radians)

$$D(k_x,0)=\sum_{t=-l}^{l}\sum_{r=0}^{0}\frac{p_r(i\Delta x)p_r(t\Delta x)}{\sum\limits_{t=-l}^{l}p_r^2(t\Delta X)}e^{-i2\pi t\Delta xk_x}$$

$$\cdot\left\{\sum_{u=-l}^{l}\sum_{s=0}^{0}\frac{q_s(j\Delta x)q_s(u\Delta y)}{\sum\limits_{u=-l}^{l}q_s^2(u\Delta y)}\right\}.$$

(2.28)

The limit of the inner summation of the second term has been intentionally omitted. It is m-r and r for polynomial types 2.1a and b respectively. Regardless, this term equals 1, and the spectra along the axes are identical.

The utility of local least-squares convolution operators

It may be preferable to implement an algorithm for filtering gravity data in terms of convolution, rather than using a frequency-domain approach, either because of ease of implementation or for the sake of efficiency when filtering small data sets. For potential-field data this is done almost exclusively with finite-impulse-response (FIR) filters. This is probably due to the fact that a linear phase response is not easily realized with infinite-impulse-response (i.e. recursive) filters. Designing FIR filters entails determining the coefficients of the impulse response. This task has received considerable attention. The usual procedure is to approximate the frequency-domain response of the filter with a windowed (i.e. finite) space-domain representation of the operator. Because local least-squares polynomial fitting and linear digital filtering are equivalent operations, coefficients of weight functions for low-pass and high-pass filters can be obtained without transforming between domains. This circumvents the

difficulties encountered when the infinite operator is truncated to give a useable operator. In addition, because obtaining the coefficients of local least-squares impulse responses does not require performing a Fourier transform, it is possible to obtain weight functions very rapidly.

Hence, the expressions presented here, accompanied by the analysis of the filtering characteristics, make possible the efficient and accurate design of shift-invariant two-dimensional impulse responses, with reliable and predictable amplitude characteristics. In addition, the low-pass filters form the foundation of a new type of filter for computing the components of the horizontal-gradient vector. This is the topic of the next chapter.

Chapter 3 - Horizontal-Gradient-Vector-Component Filters

The horizontal-gradient vector of gravity

The horizontal gradient of gravity is a vector quantity, with components determined by partial derivatives with respect to the independent position variables x and y. Telford et al. (1976) give expressions for the vertical component of the gravitational acceleration, and the x-component and y-component of its horizontal gradient in terms of the gravitational potential, U, at a distance r from the centre of a three-dimensional body of arbitrary shape and density ρ. If subscripts denote partial derivatives (for example U_z denotes differentiation with respect to z, and thus is the vertical component of acceleration, and U_{zx} is the derivative with respect to x of the vertical component of acceleration), then these expressions are:

$$U_z \equiv \frac{\partial U}{\partial z} = -\gamma \rho \iiint_{x\,y\,z} \frac{z}{r^3} dx dy dz \qquad (3.1a)$$

$$U_{zx} \equiv \frac{\partial^2 U}{\partial x \partial z} = 3\gamma \rho \iiint_{x\,y\,z} \frac{xz}{r^5} dx dy dz \qquad (3.1b)$$

$$U_{yz} \equiv \frac{\partial^2 U}{\partial y \partial z} = 3\gamma \rho \iiint_{x\,y\,z} \frac{yz}{r^5} dx dy dz \qquad (3.1c)$$

where

$$r = \sqrt{x^2 + y^2 + z^2} \qquad (3.1d)$$

The horizontal-gradient vector will have magnitude,

$$H = \sqrt{U_{xz}^2 + U_{yz}^2} \qquad (3.2a)$$

and direction

$$\theta = \tan^{-1}\frac{U_{yz}}{U_{xz}}. \qquad (3.2b)$$

The present study focuses on computing and applying the magnitude of the horizontal gradient.

Equations 3.1 and 3.2a indicate the theoretical differences between acceleration and gradient magnitudes. The significant differences are: the gradient attenuates more rapidly with increasing r, and thus for multisource data there will be less interference from neighbouring bodies; and inflection points of acceleration correspond to maxima of gradient magnitudes.

These properties imply that the gradient magnitude is useful for delineating source-body geometry. This has been recognized by a number of researchers, and it has been demonstrated that for two- and three-dimensional rectangular parallelepipeds the maxima of the horizontal gradient corresponds spatially to the edges of the source body (for example see Heiland, 1943; Cordell and Grauch, 1985; Blakely and Simpson, 1986). It should be noted that for two-dimensional parallelepipeds that are not rectangular, and extend to infinity in either the horizonal or vertical direction, the offset of the gradient maximum from the edge is predictable (Grauch and Cordell, 1987).

A review of computational methods and applications of gradient magnitude data

The purpose of this section is to review the techniques that have been developed for computation of the components of the horizontal-gradient vector, and to describe briefly some typical applications. These can be classified as one of three methods: finite differences (Cordell, 1979; Cordell and Grauch, 1982; 1985), least-squares polynomial fitting (Sharpton et al., 1987), and wavenumber-domain digital filter design (Dole and Jordan, 1978; Kis, 1983).

The simplest and most commonly applied method is that of finite differences. According to this approach, the x- and y-components of the horizontal gradient for data $g(x,y)$, whose digital grid representation is denoted $g_{i,j}$, are respectively,

$$\frac{\partial g}{\partial x}\Big|_{i,j} \approx \frac{g_{i+1,j} - g_{i-1,j}}{2\Delta x} \tag{3.3a}$$

$$\frac{\partial g}{\partial y}\Big|_{i,j} \approx \frac{g_{i,j+1} - g_{i,j-1}}{2\Delta y}. \tag{3.3b}$$

Equations 3.3 can be rewritten in terms of convolution. The impulse responses are:

$$\frac{1}{\Delta x}\begin{pmatrix} 0 & 0 & 0 \\ 0.5 & 0 & -0.5 \\ 0 & 0 & 0 \end{pmatrix};$$

and

$$\frac{1}{\Delta y}\begin{pmatrix} 0 & 0.5 & 0 \\ 0 & 0 & 0 \\ 0 & -0.5 & 0 \end{pmatrix}.$$

Gradient-magnitude data have been computed by this technique for several published studies. For example, Cordell (1979) inferred that the maxima of such data located graben-bounding faults in the Española Basin, New Mexico. In addition, Cordell and Grauch (1985) mapped boundaries of basement magnetization zones from so-called pseudogravity data (Cordell and Grauch, 1985) in the San Juan basin, New Mexico. Further, Grauch and Sawatzky (1989) developed an algorithm based on statistical analysis of these kinds of data to delineate high-angle normal faults in Nevada.

It is also possible to design digital gradient filters in the wavenumber domain. This is possible because the Fourier transform of the derivative of a function with respect to an independent variable amounts to multiplication by the corresponding frequency, and reversal of the phase (Erdélyi et al., 1954). That is, if S_{kx} and S_{ky} are the transfer functions of differentiation with respect to x and y respectively, then

$$S_{kx}(k_x, k_y) = i2\pi k_x \qquad (3.4a)$$

and

$$S_{ky}(k_x, k_y) = i2\pi k_y. \qquad (3.4b)$$

Equation 3.4a and 3.4b demonstrate that obtaining the components of the gradient is equivalent to high-frequency amplification, and elimination of zero-frequency components. These are desirable properties of an edge-detection filter; however, it is undesirable to amplify monotonically the spectrum, because the noise that resides at the high frequencies will obscure the lower-frequency signal. Thus, design of gradient

operators as digital filters entails tapering the high-frequency band of the ideal transfer function of differentiation, given by equation 3.4, and inverse-Fourier transforming this function to generate the impulse response of the filter.

Dole and Jordan (1978) published two separate one-dimensional convolution operators which could be applied in the x- and y-directions in order to compute gradient components. One set of weights was intended for use on relatively noise-free data, while the second set was designed with a lower high-cut wavenumber. These authors did not describe the method used for tapering the filter. This technique can also be used to obtain two-dimensional weight functions. Kis (1983) designed operators based on the two-dimensional inverse discrete Fourier transform, tapered using a low-pass filter. The transfer function of the low-pass filter is:

$$S_{LP}(f_x, f_y) = e^{-\left(\frac{36}{m}\right)(f_x^2 + f_y^2)} \tag{3.5}$$

where m is an integer that controls the width of the passband of the filter. That is, increasing m increases the width of the passband. Then weight functions for the gradient-component operators, denoted $s_x(x,y)$ and $s_y(x,y)$ for the x- and y-component operators respectively, are found by inverse Fourier transforming the transfer functions,

$$s_x(x,y) = \frac{1}{M^2} \sum_{p=-\frac{M}{2}}^{\frac{M}{2}} \sum_{r=-\frac{M}{2}}^{\frac{M}{2}} S_{LP}\left(\frac{p}{M}, \frac{r}{M}\right) S_{kx}\left(\frac{p}{M}, \frac{r}{M}\right) e^{i\frac{2\pi}{M}(xp + yr)} \tag{3.6a}$$

and

$$s_y(x,y) = \frac{1}{M^2} \sum_{p=-\frac{M}{2}}^{\frac{M}{2}} \sum_{r=-\frac{M}{2}}^{\frac{M}{2}} S_{LP}\left(\frac{p}{M},\frac{r}{M}\right) S_{ky}\left(\frac{p}{M},\frac{r}{M}\right) e^{i\frac{2\pi}{M}(xp+yr)} \qquad (3.6b)$$

where S_{kx} and S_{ky} are given by equations 3.4a and b respectively, and M is the number of points computed in the frequency domain. This technique is essentially a high-frequency enhancement filter cascaded with a low-pass filter to subdue high-frequency noise.

Sharpton et al. (1987) introduced local least-squares polynomial fitting as a technique for computing the horizontal gradient. Their approach is to compute the x- and y-components of the gradient from the two partial-regression coefficients, calculated by performing a least-squares polynomial fit of a first-order polynomial within a 5x5 grid. The magnitude is then assigned to the central grid point in the window.

A review of published accounts of applications of data computed with this algorithm indicate that they are used exclusively for studying crustal-scale features. Sharpton et al. (1987) used gradient trends to locate lateral discontinuities in the upper crust, and from these delineated sutures and rifts. Thomas et al. (1987) used these data to delimit Precambrian tectonic boundaries buried beneath the North American central plains. Thomas et al. (1988) presented a gravity trend map of North America based on horizontal-gradient magnitudes. This trend map was the framework for defining gravity-trend domains that were in turn used to deduce boundaries that support the notion of accretionary continental growth.

It will be shown that this method is equivalent to two-dimensional convolution, and an expression for the weights of the impulse response will be derived. Through wavenumber-domain analysis of the expression for the space-domain convolution operator, it is possible to show that for the 5 km x 5 km grid used in these three studies, the x- and y-components of the gradient each pass wavelengths approximately between 80 km and 100 km. Thus this approach is limited to applications to relatively large-scale features. The method that is derived in this investigation generalizes this technique, and reformulates it so that the passband of the gradient calculation is both variable and measurable.

Local least-squares polynomial gradient-component operators

The technique that is presented here is founded on local least-squares polynomial fitting. The two-step procedure required to compute derivatives with this technique is: determine a best-fit function for the data; and take analytical partial derivatives of this function with respect to the two independent position variables in order to compute the two components of the vector. As such, a version of the technique has been used previously, as was discussed above; however, the approach presented here has two significant differences: the algorithm has been reformulated as two-dimensional convolution; and the method has been generalized so that an analytic expression for the impulse response, as a function of the polynomial order and the window size, has been derived.

The advantages of convolution over the conventional least-squares approach for

filtering data were previously discussed. These advantages hold true for gradient computations. In addition, because the studies reviewed have demonstrated that gradient-magnitude maps are an effective means of detecting trends, a general expression for gradient-component weight functions facilitates designing filters that pass a specified frequency band. This enables trends corresponding to desired frequency bands to be amplified, making it possible to tailor the bandwidth of the edge-detection filter to suit the goals of the study. That is, for a small-scale survey in which the aim is to highlight relatively small shallow features, it would be desirable to magnify the high spatial frequencies; whereas for a larger survey, and deeper targets, lower wavenumbers could be emphasized.

Using gradients for enhancing high-frequency bands by computing derivatives via local least-squares polynomial fitting has been applied in other disciplines. For example, Besl (1988) presented expressions for computing partial derivatives of digital surfaces using second-order orthogonal polynomials. In addition, Letts and Rochon (1980) derived an operator for application to topographic data, based on a 3x3 window and a second-order polynomial. These authors derived the weights by rearranging the expression for the minimization of the square of the error (equation 2.4).

The starting point for this derivation is the previously presented method for local least-squares regional and residual calculations. Thus the gradient computations may be performed using either nonorthogonal polynomials or orthogonal polynomials. Procedures for calculating the gradient components will be presented for both classes of polynomials.

The method of nonorthogonal polynomials

As before, the data are assumed to be on a rectangular grid, with dimensions $m\Delta x$ by $p\Delta y$ where Δx and Δy are the grid intervals in the x and y directions. The moving window is specified by $\{x_{i-w}, y_{j-w})\}$ through $\{x_{i+w}, y_{j+w})\}$, where $i = 1,2,...,m$, $j = 1,2,...,n$, $w = 1,2,...,2k+1$, $k \leq (p-1)/2$ and $k \leq (m-1)/2$. Again, let $Z(x,y)$ represent the best-fit polynomial in the window; then,

$$Z(x,y) = \sum_{r=0}^{n} \sum_{s=0}^{n} a_{rs} x^r y^s \qquad (3.7)$$

where n is the order of the polynomial. It is important to note that polynomials defined by equation 2.1b are used rather than those specified by 2.1a. This is because, as was demonstrated in the previous chapter , the polynomials given by 2.1b have more reliable filtering characteristics than those given by 2.1a.

The analytical partial derivatives of this function with respect to x and y are respectively:

$$\frac{\partial Z}{\partial x} = \sum_{r=0}^{n} \sum_{s=0}^{n} r a_{rs} x^{r-1} y^s \qquad (3.8a)$$

and

$$\frac{\partial Z}{\partial y} = \sum_{r=0}^{n} \sum_{s=0}^{n} sa_{rs}x^{r}y^{s-1} \tag{3.8b}$$

Imposing the L_2 norm is one method of determining the best-fit polynomial for the data,

$$\frac{\partial E}{\partial a_{rs}} = 0 \tag{3.9}$$

for all $r = 0,1,2,... n$, and $s = 0,1,2,...n$

where

$$E = \sum_{t=i-w}^{i+w} \sum_{u=j-w}^{j+w} \{Z(x_t, y_u) - z(x_t, y_u)\}^2. \tag{3.10}$$

Solving the ensuing system of $(n+1)^2$ normal equations gives the least-squares solution for the coefficients a_{rs}. These can in turn be used to compute the x- and y-components of the gradient with equations 3.8.

The method of orthogonal polynomials

In the previous chapter an analytic expression for convolution operators for regional-pass least-squares polynomial filtering was derived. The derivative theorem for convolution (Båth, 1974) allows these operators to be transformed to gradient-component operators. This theorem can be stated as

$$\frac{\partial}{\partial x}[f_1(x,y) * f_2(x,y)] = \frac{\partial f_1(x,y)}{\partial x} * f_2(x,y)$$
$$= f_1(x,y) * \frac{\partial f_2(x,y)}{\partial x} \tag{3.11a}$$

and

$$\frac{\partial}{\partial y}[f_1(x,y) * f_2(x,y)] = \frac{\partial f_1(x,y)}{\partial y} * f_2(x,y)$$
$$= f_1(x,y) * \frac{\partial f_2(x,y)}{\partial y}$$

(3.11b)

Thus, differentiating the expression for the weight function of regional-pass filters with respect to x and y transforms these to operators which have outputs that are the x- and y-components of the gradient. These filters thus incorporate the high-frequency enhancement behaviour of differentiation with the low-pass nature of regional filters. The result, as will be borne out by wavenumber-domain analysis, is a class of band-pass filters for which the transmission band may, to a certain extent, be selected.

This discussion thus begins with the expression for the impulse response of the smoothing filter previously presented,

$$b_{mn} = \sum_{r=0}^{n} \sum_{s=0}^{n} \frac{p_r(x_i)p_r(m)q_s(0)q_s(n)}{\sum\limits_{m=-l}^{l} \sum\limits_{n=-l}^{l} p_r^2(m)q_s^2(n)}.$$

(2.12)

There is a subtle change here from the notation convention used in the previous chapter. Previously the origin of the coordinate system was placed at the centre of the window because this allowed substitution of zero for x_i, thereby simplifying computation of the impulse response without sacrificing generality. In this case, the x-dependence is explicit because there is no such substitution. Thus the operator for the x-component of the gradient is:

$$\frac{\partial b_{mn}}{\partial x_i} = \sum_{r=0}^{n} \sum_{s=0}^{n} \frac{\partial p_r(x_i)}{\partial x_i} \frac{p_r(m)q_s(0)q_s(n)}{\displaystyle\sum_{m=-l}^{l} \sum_{n=-l}^{l} p_r^2(m)q_s^2(n)}. \tag{3.12a}$$

Similarly, substituting $q_s(y_j)$ for $q_s(0)$ in equation 2.12, and differentiating this expression with respect to y, gives the impulse response for the y-component of the gradient,

$$\frac{\partial b_{mn}}{\partial y_j} = \sum_{r=0}^{n} \sum_{s=0}^{n} \frac{\partial q_s(y_j)}{\partial y_j} \frac{p_r(m)p_r(0)q_s(n)}{\displaystyle\sum_{m=-l}^{l} \sum_{n=-l}^{l} p_r^2(m)q_s^2(n)}. \tag{3.12b}$$

It is seen from equation 3.12 that computing gradient operators requires taking derivatives of orthogonal polynomials. This can be done by differentiating the recursive relationships of Forsythe (1957), given by equation 2.7. These derivatives are:

$$\frac{\partial p_{-1}(x)}{\partial x} = 0$$

$$\frac{\partial p_0(x)}{\partial x} = 0 \tag{3.13}$$

$$\frac{\partial p_{r+1}(x)}{\partial x} = 2(1 - \frac{\partial \alpha_{r+1}}{\partial x})p_r(x) + 2(x - \alpha_{r+1})\frac{\partial p_r(x)}{\partial x}$$
$$- \beta_r \frac{\partial p_{r-1}(x)}{\partial x} - \frac{\partial \beta_r}{\partial x}p_{r+1}(x)$$

where

$$\frac{\partial \alpha_{r+1}}{\partial x_i} = \frac{\sum_i p_r^2(x_i)\left(p_r^2(x_i) + 2x_i p_r(x_i)\frac{\partial p_r(x_i)}{\partial x_i}\right) - 2x_i p_r^3(x_i)\frac{\partial p_r(x_i)}{\partial x_i}}{\left(\sum_i p_r^2(x_i)\right)^2} \qquad (3.14a)$$

and

$$\frac{\partial \beta_r}{\partial x_i} = 2\frac{\sum_i p_r(x_i)\frac{\partial p_r(x_i)}{\partial x_i}p_{r-1}^2(x_i) - p_{r-1}(x_i)\frac{\partial p_{r-1}(x_i)}{\partial x_i}p_r^2(x_i)}{\left(\sum_i p_{r-1}^2(x_i)\right)^2}. \qquad (3.14b)$$

Equations 3.13, 3.14 and 2.7 make it possible to compute the derivative of the $(r+1)$-order orthogonal polynomial from the values of the two previous orthogonal polynomials and their derivatives. These are the final formulae necessary for generating partial derivatives of the regional-pass weight functions, given by equations 3.12, giving the gradient-component operators.

Properties and computational procedures of local least-squares polynomial gradient-component operators

It is possible to simplify the recursive relationship for the derivatives of the orthogonal polynomials, and hence simplify computation of the gradient-component operators. Three factors make this possible. First, the derivative needs to be evaluated only at $x_i = 0$. Second, in the previous chapter it was demonstrated that $\alpha_{r+1} = 0$ always in the symmetrical interval defined by the moving window. Finally, examination of equation 3.14b indicates the derivative of β_r is zero in the moving window. This is because the numerator of equation 3.14b is the sum of an odd

function over a symmetrical interval, and thus is equal to zero. The product under summation in the numerator of equation 3.14b can be seen to be odd by recalling the property of orthogonal polynomials expressed by equation 2.15, coupled with the following property:

$$\frac{\partial p_r(x)}{\partial x} = \frac{\partial p_r(-x)}{\partial x} \quad \text{if } r \text{ is even}$$

$$\frac{\partial p_r(x)}{\partial x} = -\frac{\partial p_r(-x)}{\partial x} \quad \text{if } r \text{ is odd} \tag{3.15}$$

Incorporating these three factors into equation 3.13 allows this recursive relationship to be written as

$$\frac{\partial p_{-1}(x)}{\partial x} = 0$$

$$\frac{\partial p_0(x)}{\partial x} = 0 \tag{3.16}$$

$$\left[\frac{\partial p_{r+1}(x)}{\partial x}\right]_{x=0} = 2(1 - \frac{\partial \alpha_{r+1}}{\partial x})p_r(x) - \beta_r \frac{\partial p_{r-1}(x)}{\partial x}.$$

Another factor that must be considered is the dependence on the grid interval. As would be expected, the gradient-component operators are proportional to the grid interval. A generalized approach to incorporating this dependence is to compute the convolution weights using equations 3.12 and a unit grid interval. This generates weight functions that may then be applied to data on any grid by dividing the output of the convolution by the grid interval. The units of the ensuing gradient component will then be data units per grid interval.

There are four properties of the impulse response of gradient-component operators that are not shared by the regional filters. These are here discussed.

(1) In the previous chapter it was shown that the weight function given by equation 2.12 did not change for orders n and $n+1$, with $n = 0,2,4,...$. This is because in equation 2.12 for odd powers of either r or s, and hence for odd powers of n, it is necessary to evaluate orthogonal polynomials for either $x = 0$ or $y = 0$. It was established that odd orthogonal polynomials, evaluated at zero are in turn zero, and thus odd powers do not contribute to the filter coefficients. Examination of equations 3.12 indicates that this does not apply to gradient-component operators. This is because calculating these operators does not require evaluating odd orthogonal polynomials for x and y simultaneously equal to zero. Hence a unique operator is generated for each polynomial order and a given window size.

(2) Equations 2.14 and 3.16 imply that these operators are even functions about the axis corresponding to the gradient-component being computed, and odd about the other coordinate axis. The significance of this is that the Fourier transform of an odd function is imaginary, and thus these operators generate phase reversals. Equations 3.4a and b indicate that, from a theoretical standpoint, this is what is expected for differentiation.

(3) If the polynomial order is equal to zero, the impulse response has coefficients of zero. This result is to be expected, as the derivative of a zero order polynomial is zero.

(4) If the polynomial order is one less than the window size, the weight

function reduces to a one-dimensional operator. Using the notation of equations 3.12, non-zero coefficients occur for m equal to zero for y-component gradient operators, and for n equal to zero for x-component gradient operators. Specifically, when the window size is 3x3 and the polynomial order is two, the impulse response is identical to the finite-difference operator.

Transfer functions of horizontal-gradient operators

Three techniques for calculating the components of the horizontal gradient have been discussed. These can all be classified as two-dimensional convolutions. Thus transfer functions of these gradient operators can be determined. This serves two purposes. First, passbands of the gradient filters, and hence spatial-frequency content of gradient data, can be determined. The second motivation for transforming spatial operators is to provide a means of evaluating the efficacy of the filter. This can be done by comparing the ideal transfer functions, given by equations 3.4, with the transfer functions of each gradient operator. The goal is to design gradient weight functions whose frequency-domain representations resemble the ideal case in a given frequency band, without suffering from the drawback of high-frequency amplification. For all three weight functions, the monotonically increasing transfer function is modified by tapering the amplitude response of the high frequencies. These filters maintain the property of amplitude amplification corresponding to increasing frequencies in the low-frequency portion of the passband. Hence a criterion for evaluating these filters is the similarity of this frequency band and the corresponding

band of the ideal case.

Amplitude spectra have been generated from discrete two-dimensional Fourier transforms calculated for frequencies from zero to the Nyquist, using grid units as the spatial dimension. In the following discussion the transmission bands of these filters are estimated using the definition of cutoff given by Meskó (1984). These are the frequencies that correspond to decreases of 3 dB in the amplitude response.

Ideal gradient operators

Shown in figures 3.1a and b are the ideal transfer functions for differentiation with respect to x and y. These are plots of the functions given by equations 3.4a and b. As was previously discussed, this operation amplifies high-frequency content. The absence of a high-frequency cutoff causing enhancement of the high-frequency noise and eradication of signal is demonstrated by figure 3.2. This shows the magnitude of the horizontal gradient of the Bouguer gravity field from an area in north-central Alberta. These data will be discussed in detail in the following chapter and are shown in figure 4.1. The gradient-magnitude data were computed using the ideal x- and y-component gradient filters. This was done by fast-Fourier transforming the unfiltered gravity data and multiplying the result by $i2\pi k_x$ and by $i2\pi k_y$. The inverse transforms of these filtered spectra were computed in order to obtain the x- and y-components of the gradient. Incoherent noise is the predominant feature on these data, concealing any authentic trends, and thus rendering the results unusable. In order for gradient data to be applicable, the filter response must be modified so that it is possible to enhance a
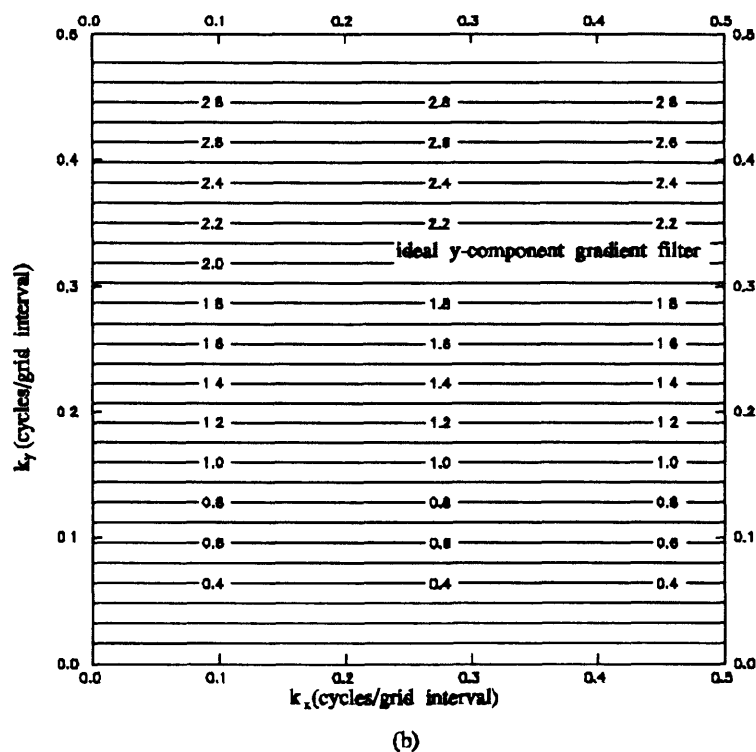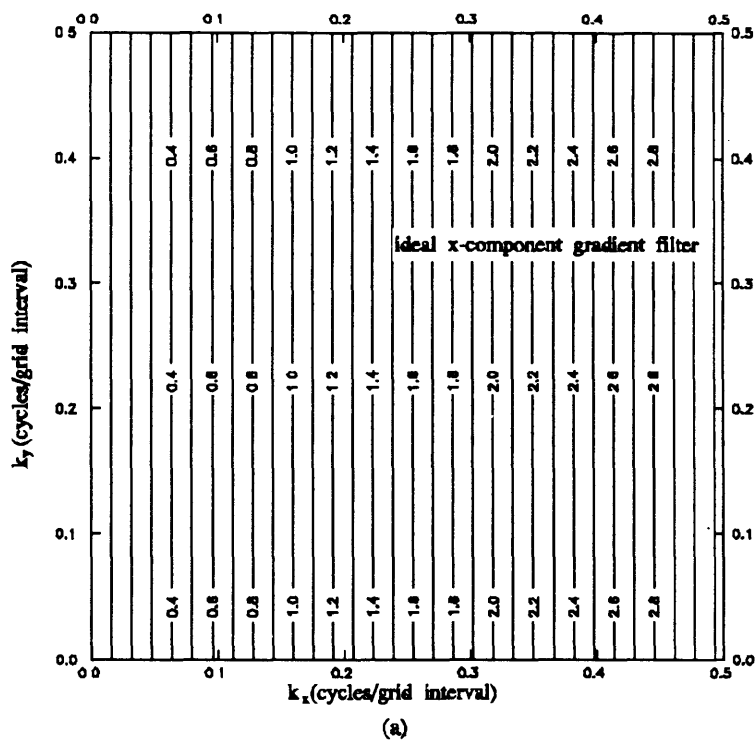
Figure 3.1. Amplitude spectra of differentiation with respect to x (a) and y (b). These are transfer functions of ideal gradient-component operators.
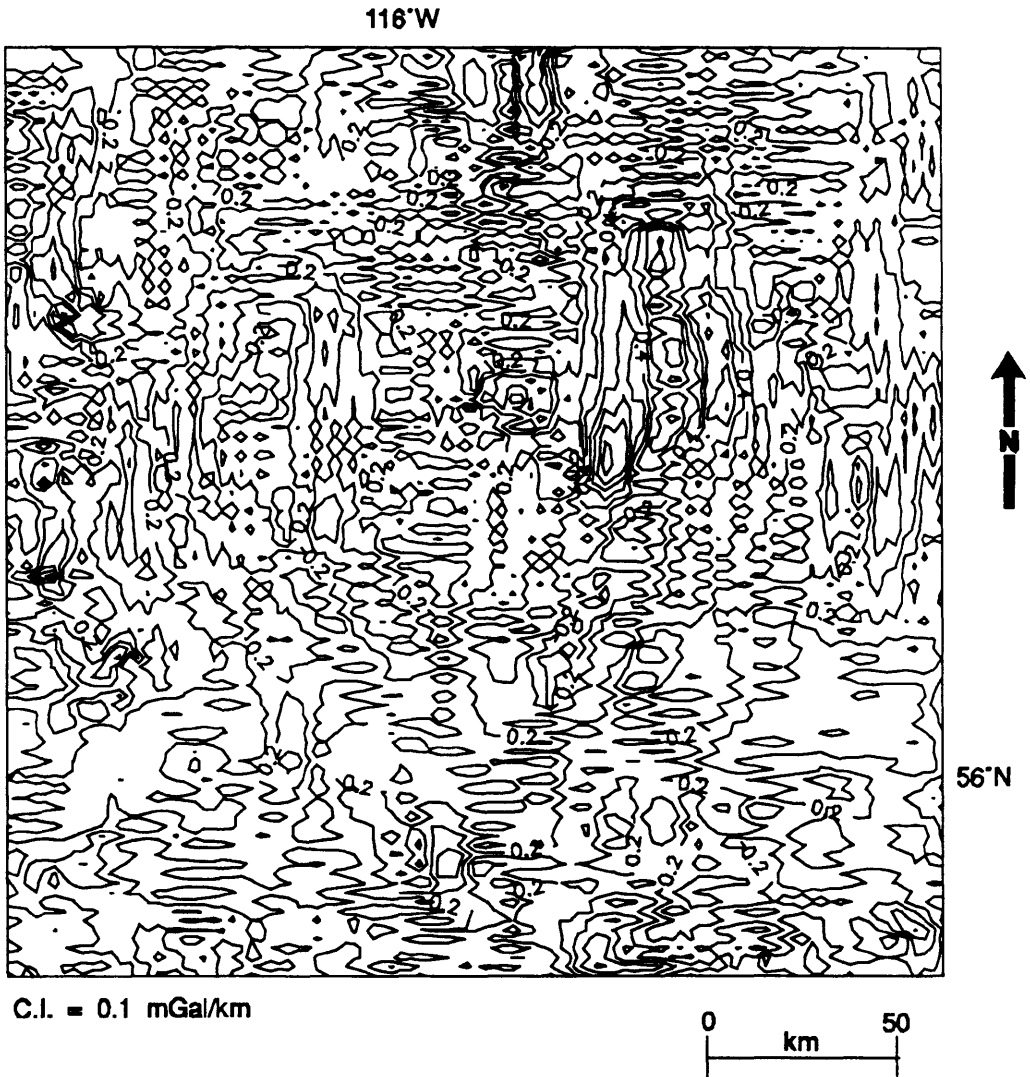
Figure 3.2. Horizontal-gradient magnitude of the Bouguer data shown in figure 4.1, computed in the wavenumber domain using ideal filter responses for differentiation with respect to the position variables x and y.

functional frequency range. The following three incarnations of this ideal case attempt to fulfil this requirement.

It can be seen on figures 3.1a and b that the filter response of the x-component operator and the y-component operator differ only by a transformation of the frequency axes. Because of this, it is only necessary to display the response of one of the gradient-component operators. Thus, in the following discussion the transfer function of the y-component operator is shown, with the understanding that the x-component operator can be obtained by a 90° counterclockwise rotation about the z-axis (where the z-axis is positive up from the k_x-k_y plane) followed by a 180° clockwise rotation about the x-axis. In addition, since the transfer functions are odd about the axis corresponding to the gradient component being computed, and even about the other frequency axis, the entire spectrum can be inferred from the spectrum in the first quadrant. Thus only this quadrant is displayed.

Finite-difference gradient operators

Shown in figure 3.3 are the filter responses of finite-difference gradient operators for the y-component. The passband of this weight function is centred at 0.25 cycles per grid units. It has low- and high-pass frequencies at 0.14 and 0.34 cycles per grid interval for frequencies parallel to the k_y axis and does not alter frequencies parallel to the k_x axis. This is what is to be expected, as these are one-dimensional operators, and thus should have amplitude responses that vary only with respect to the corresponding frequency axis. The spectrum resembles the ideal response in the low-
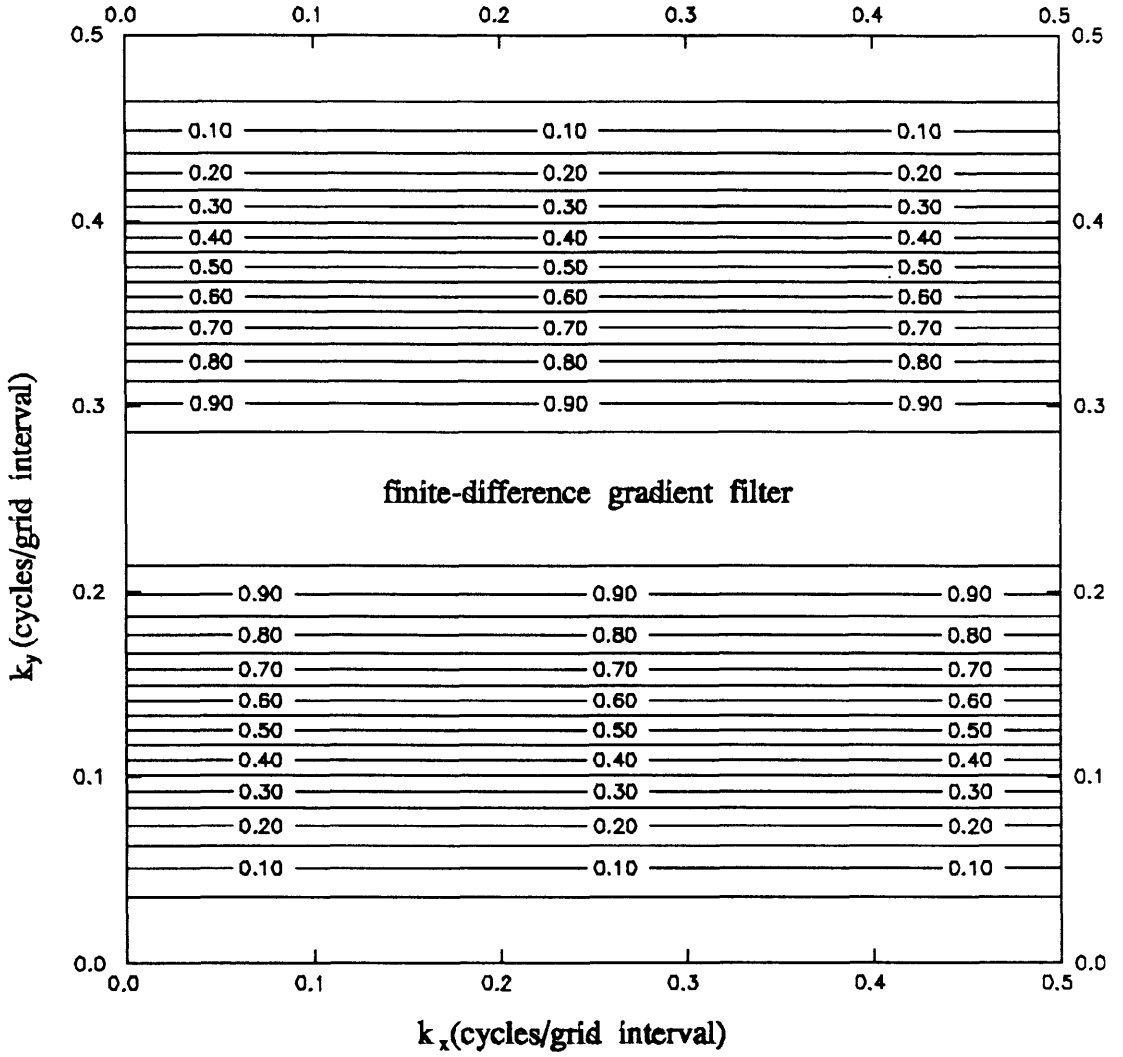
Figure 3.3. Amplitude response of the *y*-component finite-difference gradient operator.

frequency half of the passband, and thus should give reliable results for studies focusing on anomalies with wavelengths between 4.0 and 7.1 grid units. As well, these amplitude spectra make it clear that magnitude maps generated with these weight functions do not suffer from the unrestrained high-frequency amplification. However, the technique is limited because it is not possible to modify the transmission band of the filter.

Wavenumber-domain designed gradient operators

Transfer functions for several values of m have been generated from equations 3.5 and 3.6b. Responses were computed by calculating the response from equation 3.6b and inverse transforming this in the range from $-5 \leq x \leq 5$ and $-5 \leq y \leq 5$. This 11x11 weight function was then Fourier transformed to give the transfer function. Examples are shown for $m = 1$ and $m = 9$ in figures 3.4 and 3.5 respectively. These filters can be classified as *band-pass* with respect to the frequency axis corresponding to the gradient component, and *low-pass* with respect to the other frequency axis. For example, the y-component gradient filter shown is band-pass with respect to the k_y axis and low-pass with respect to the k_x axis. The filtering characteristics are thus specified by three frequencies; the low- and high-pass frequencies of the band-pass filter, and the cutoff frequency of the low-pass filter. The filter generated using $m = 9$, has a transmission band delimited by a band-pass filter designated by 1.10 and 2.53 cycles per grid interval, and a low-pass filter designated by 1.04 cycles per grid interval. Likewise, for the filter generated using $m = 1$, the transmission band is delimited by a
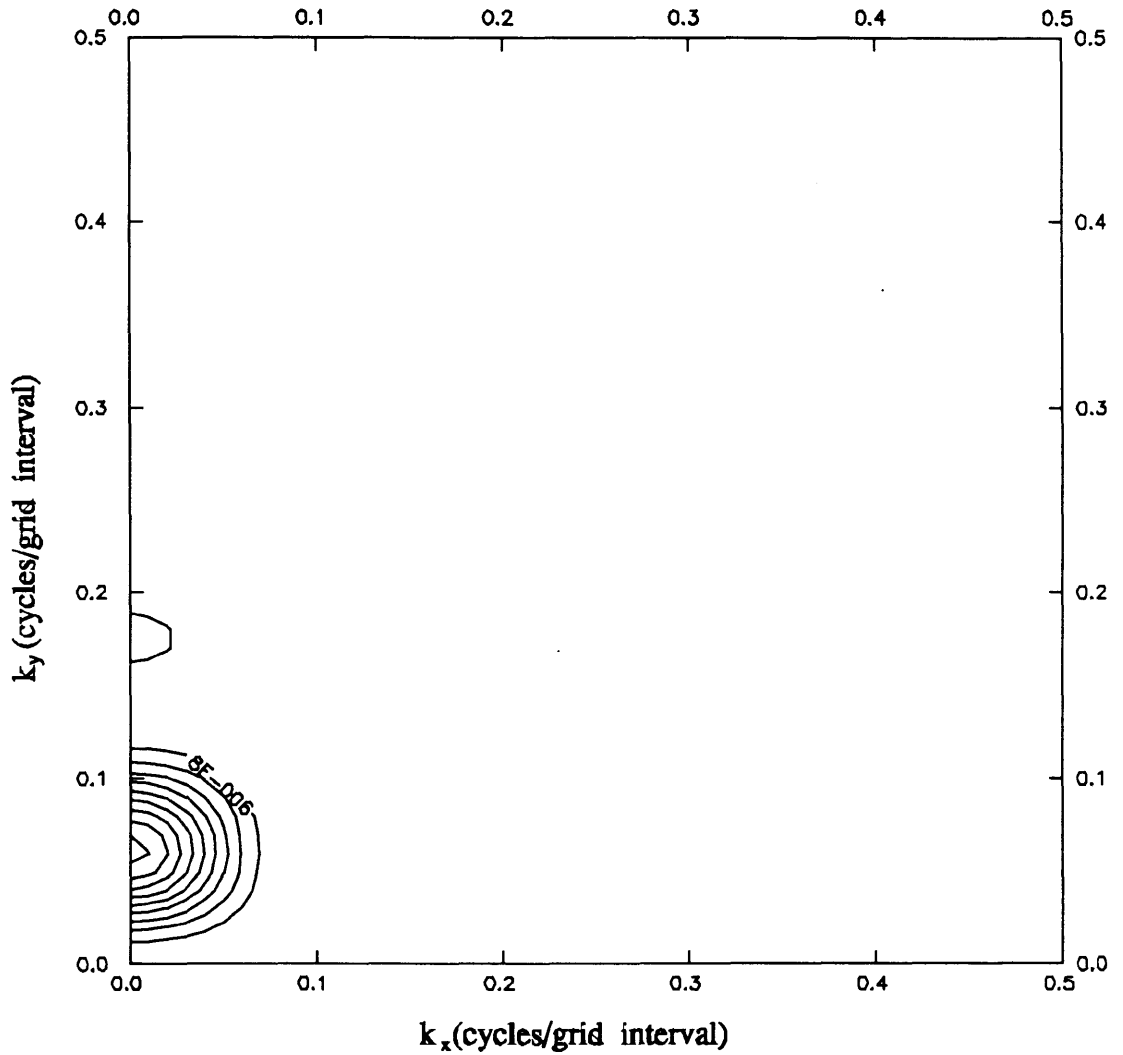
Figure 3.4. Amplitude spectrum of y-component gradient operator from Kis (1983), calculated for $m = 1$. This is the filter which passes the lowest frequency band.
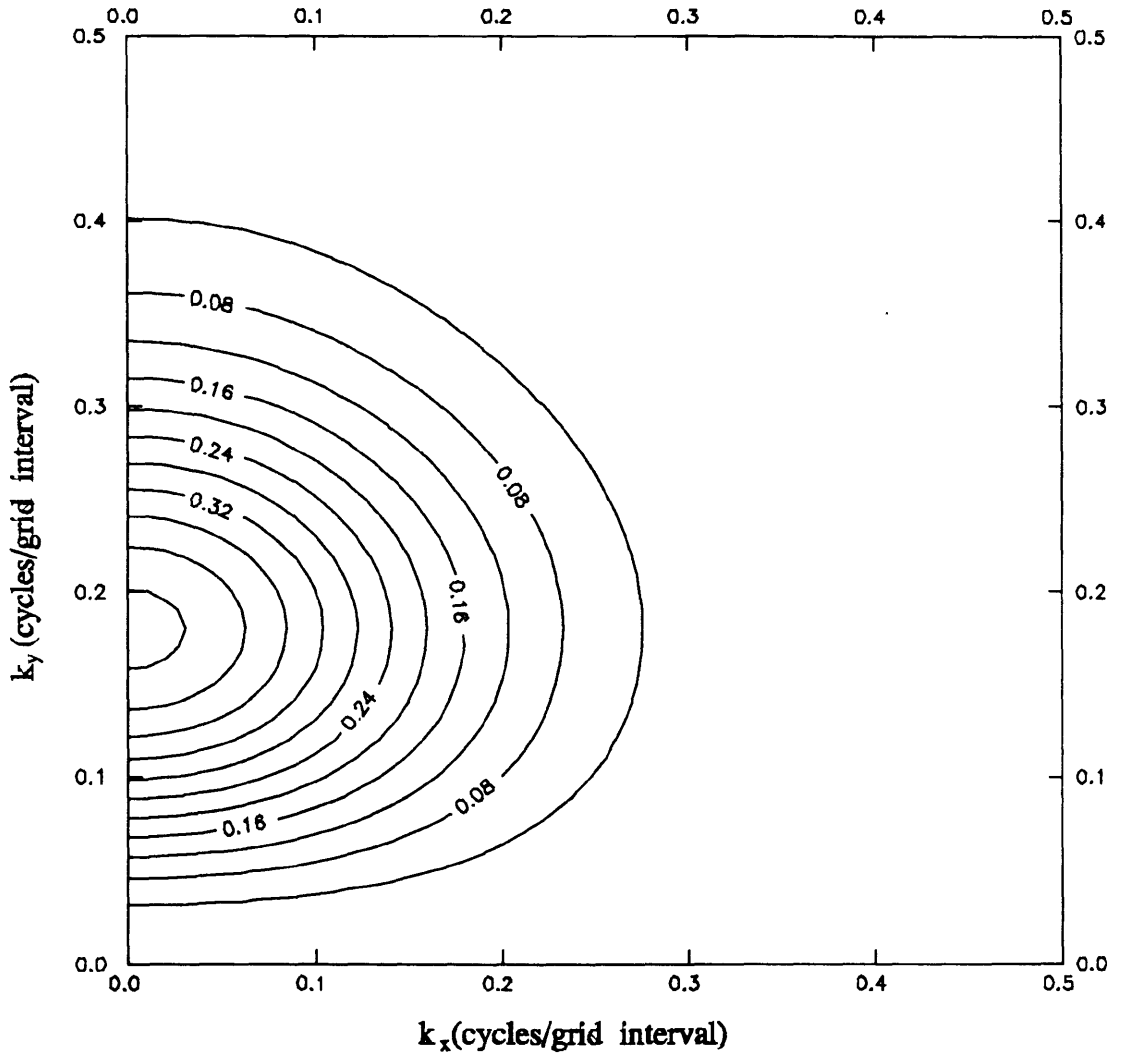
Figure 3.5. Amplitude spectrum of *y*-component gradient operator from Kis (1983), calculated for *m* = 9. This filter passes the highest frequency band that maintains the characteristics of the ideal filter.

band-pass filter designated by 0.04 and 0.08 cycles per grid interval, and a low-pass filter designated by 0.04 cycles per grid interval. These represent the practical limits of values that may be used for generating weight functions. This is because for $m = 0$ the low-pass filter becomes an all-reject filter; and for values of $m > 9$, the filter response undergoes considerable distortion in the high-frequency bands. This is demonstrated by figure 3.6, which shows an amplitude response for $m = 13$.

Comparison of the spectra shown in figures 3.4 and 3.5 with the ideal spectrum shown in figure 1b indicate that, overall, the transfer functions of these filters generally resemble the ideal filter in specific low-frequency bands of the spectrum. However, figure 3.5 indicates an inherent weakness in these weight functions: namely the flank of the transmission band does not have a constant slope. Thus the amplitude response is not consistent with those of the ideal spectra. This problem is most severe for $m = 9$, while for $m = 1$ the response is symmetric, and the slopes on the flanks of the transmission range are constant.

Local least-squares gradient operators

Computing the discrete Fourier transforms of equations 3.12a and b has enabled the amplitude spectra for local least-squares gradient operators to be computed for a variety of polynomial orders and window sizes. An example of a transfer function for a y-component operator is shown in figure 3.7, for a 5x5 window and a second-order polynomial. This transfer function is typical. That is, the response consists of a central asymmetric lobe, with smaller side lobes. Thus these operators
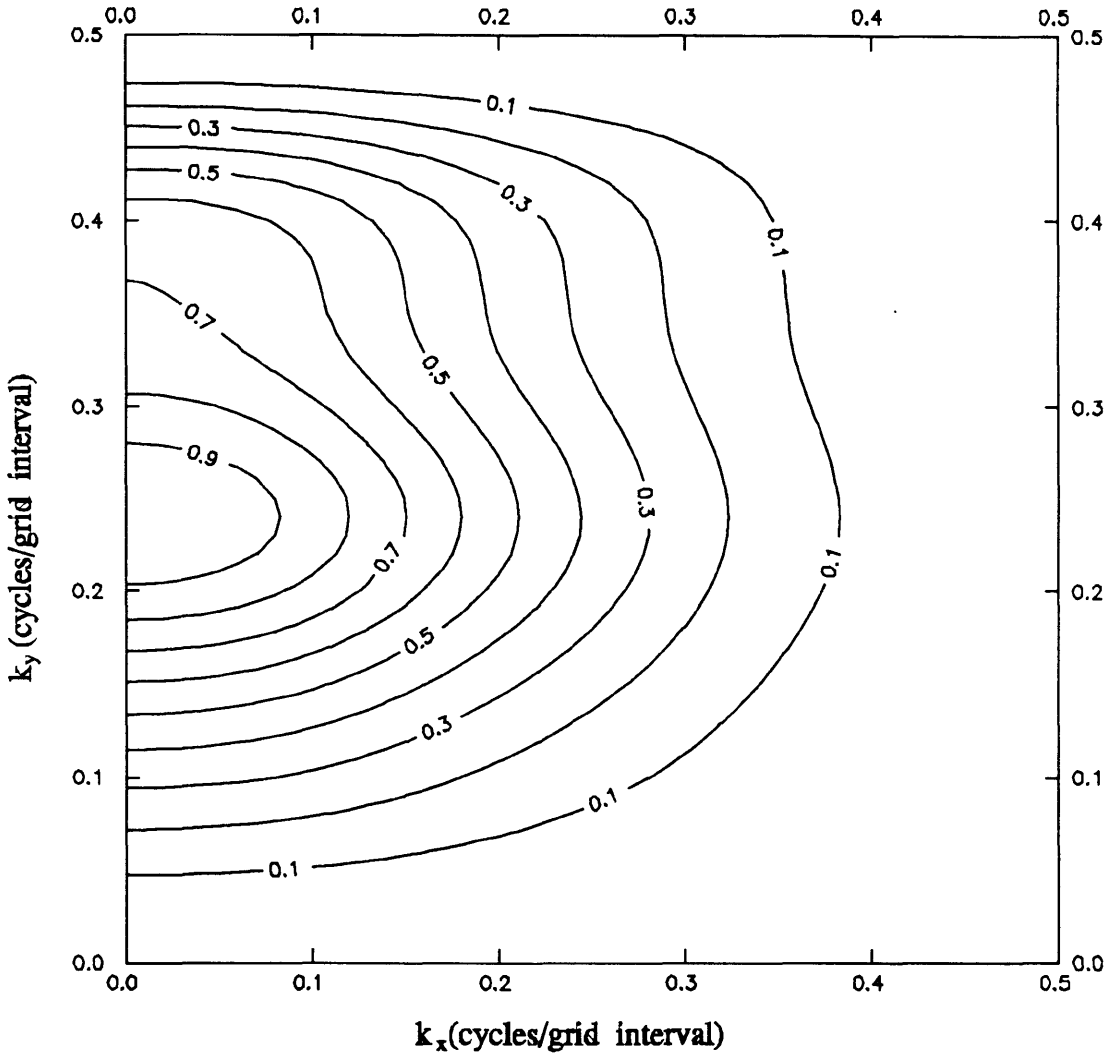
Figure 3.6. Amplitude spectrum of *y*-component gradient operator from Kis (1983), calculated for *m* = 13. There is considerable distortion from the ideal case in the high-frequency ranges.
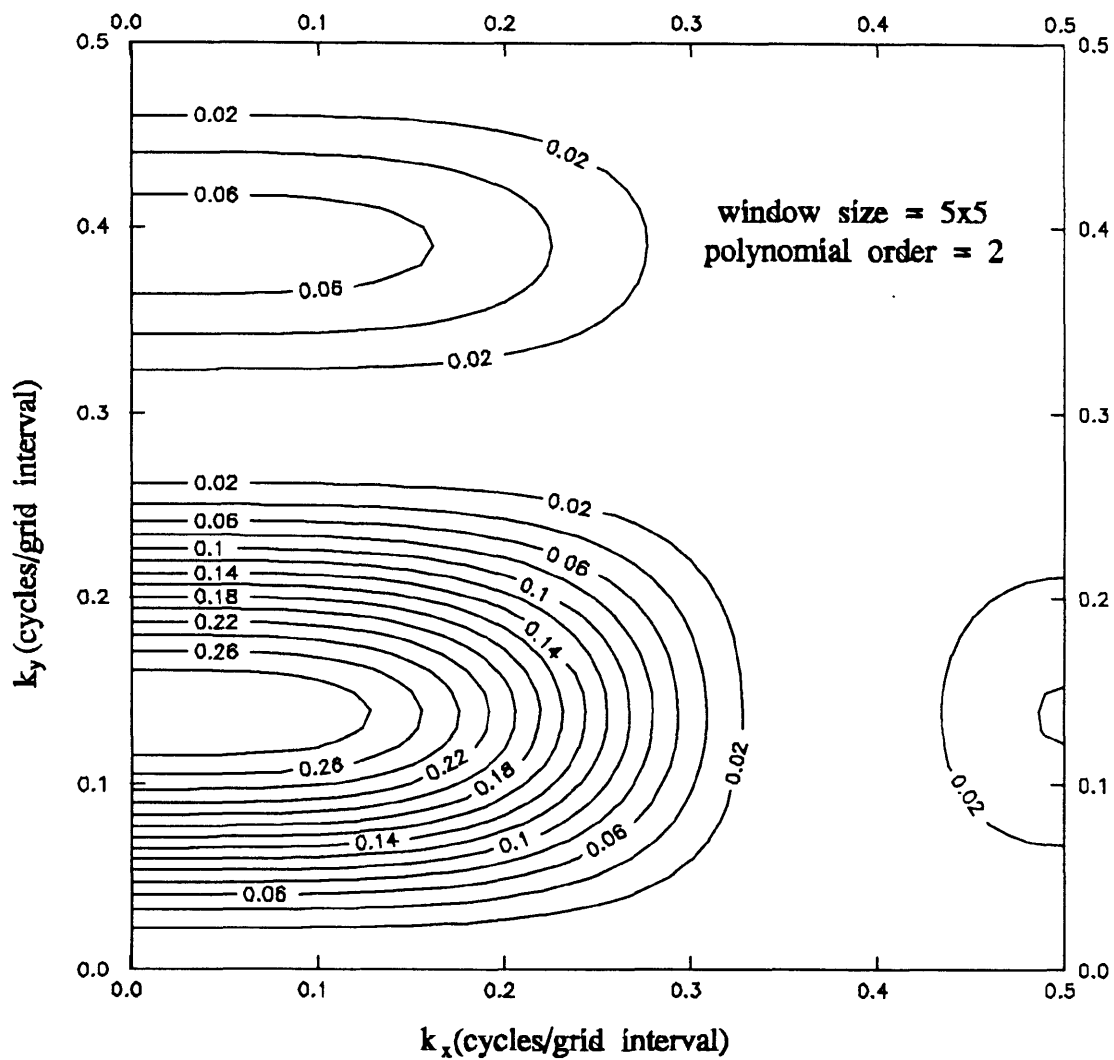
Figure 3.7. Transfer function of the *y*-component gradient operator for a 5x5 window, and a second-order polynomial.

pass virtually all frequencies, excluding zero frequency components, up to the Nyquist

frequency. However, outside of the central lobe the signal is effectively suppressed.

These filters can again be classified as band-pass filters in conjunction with low-pass

filters, as were the previous filters. It is important to note, however, the significant

improvement over the previous filters; that is, on the low-frequency flank of the

transmission band, the response conforms closely to the ideal case. Numerous

amplitude spectra, for various window sizes and polynomial orders, have been

computed, and this property applies in all cases. This indicates that local least-squares

operators have frequency-domain representations that are most consistent with the

ideal filter response.

As is the case for regional-pass filters, the passbands are determined by the

window size, and the polynomial order, and as before the wavenumbers passed

increase with increasing polynomial order and decrease with increasing window size

(Thurston et al., 1990). An example of increasing high-frequency transmission

corresponding to increasing polynomial order is shown in figures 3.8a-c. These show

filter responses for operators based on 7x7 windows and first-, second- and third-order

polynomials. In addition, figures 3.8b, 3.9a and b illustrate that frequency content

decreases with increasing window size. The transfer functions shown are for weight

functions computed with second-order polynomials, and windows of 7x7, 9x9, and

11x11.

The task of quantifying the dependence of passband on window size and

polynomial order was undertaken. The results of these analyses are shown in figures
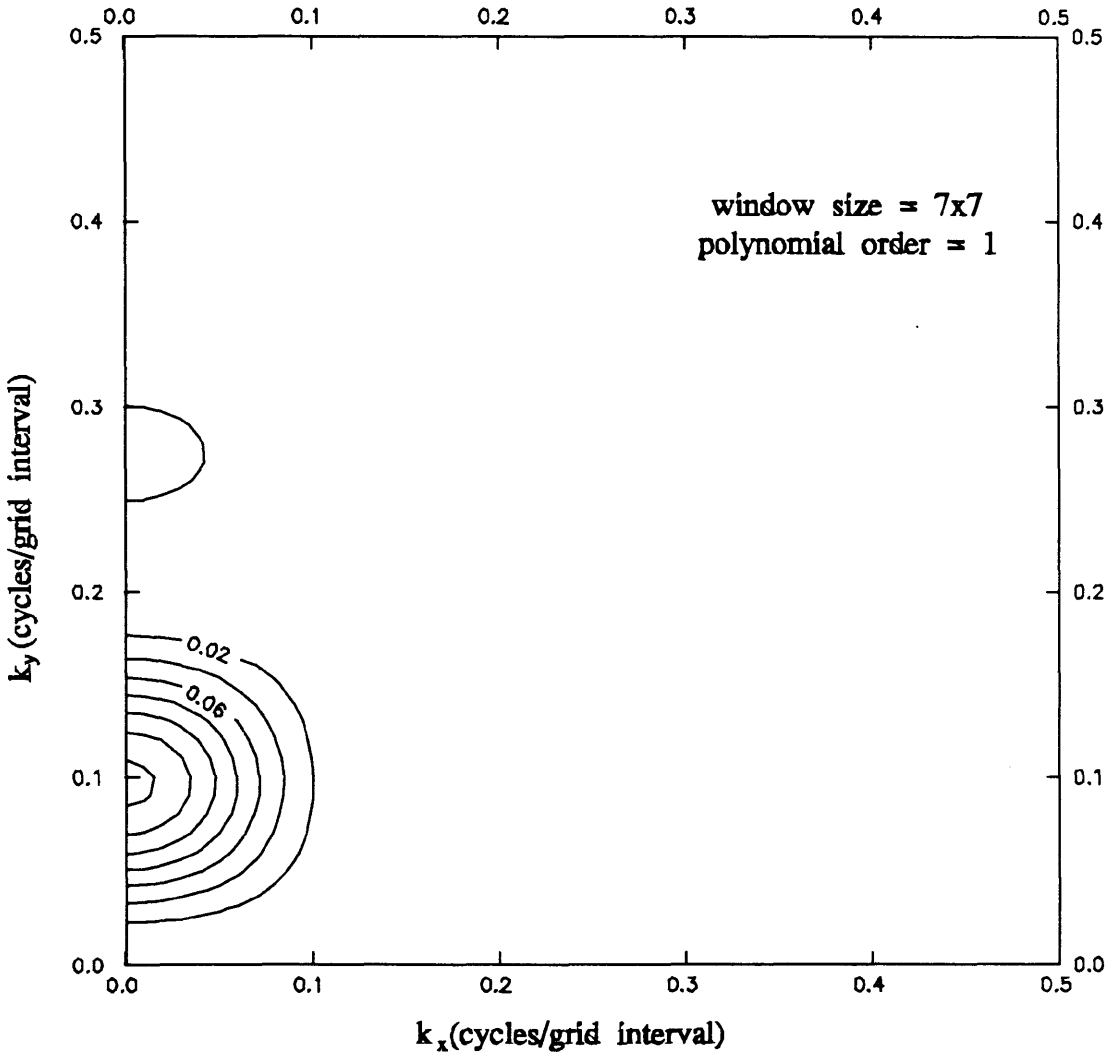
(a)

Figure 3.8. Transfer function of the *y*-component gradient operator for a 7x7 window, and a first- (a), second- (b) and third-order (c) polynomial.
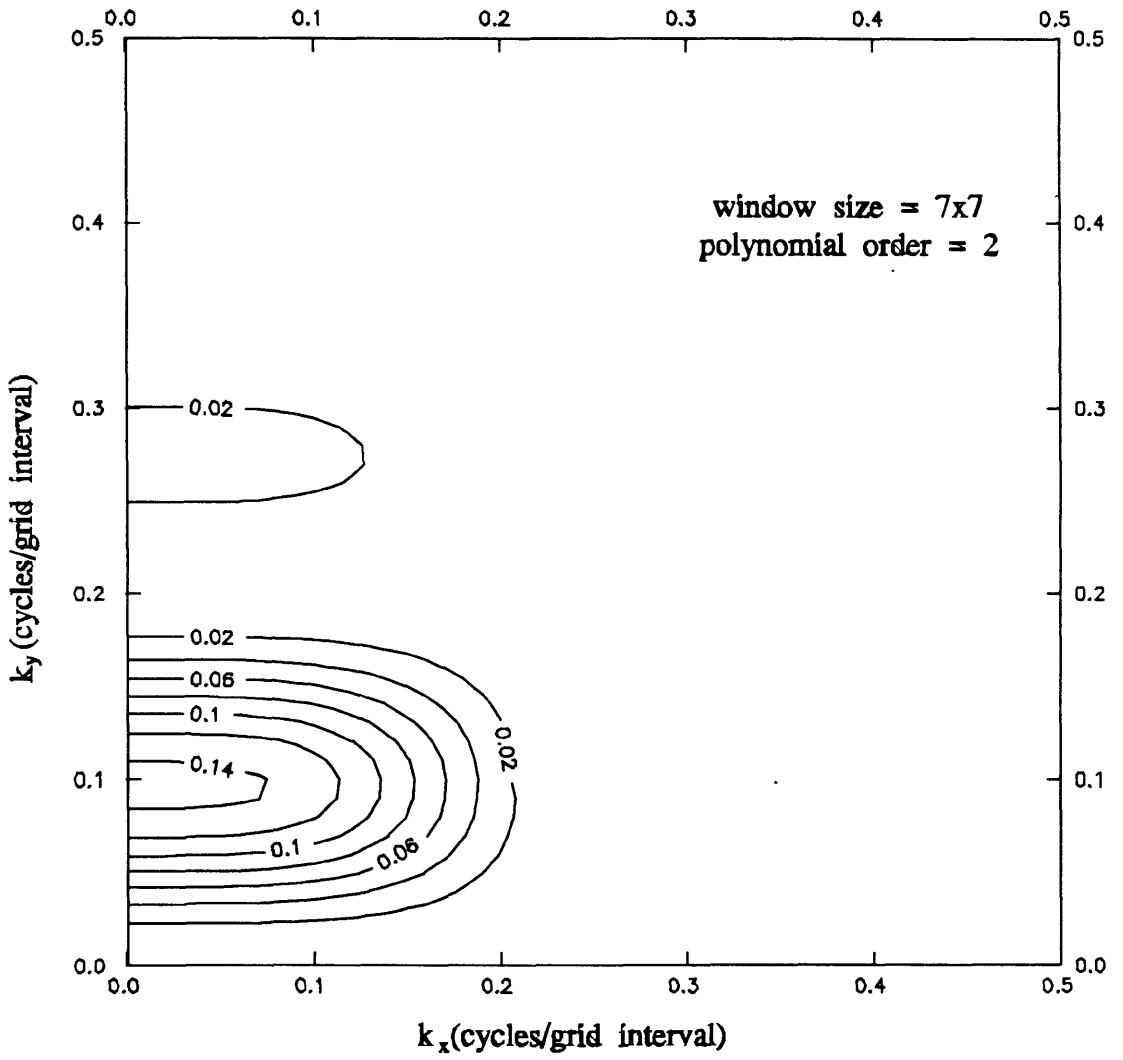
(b)
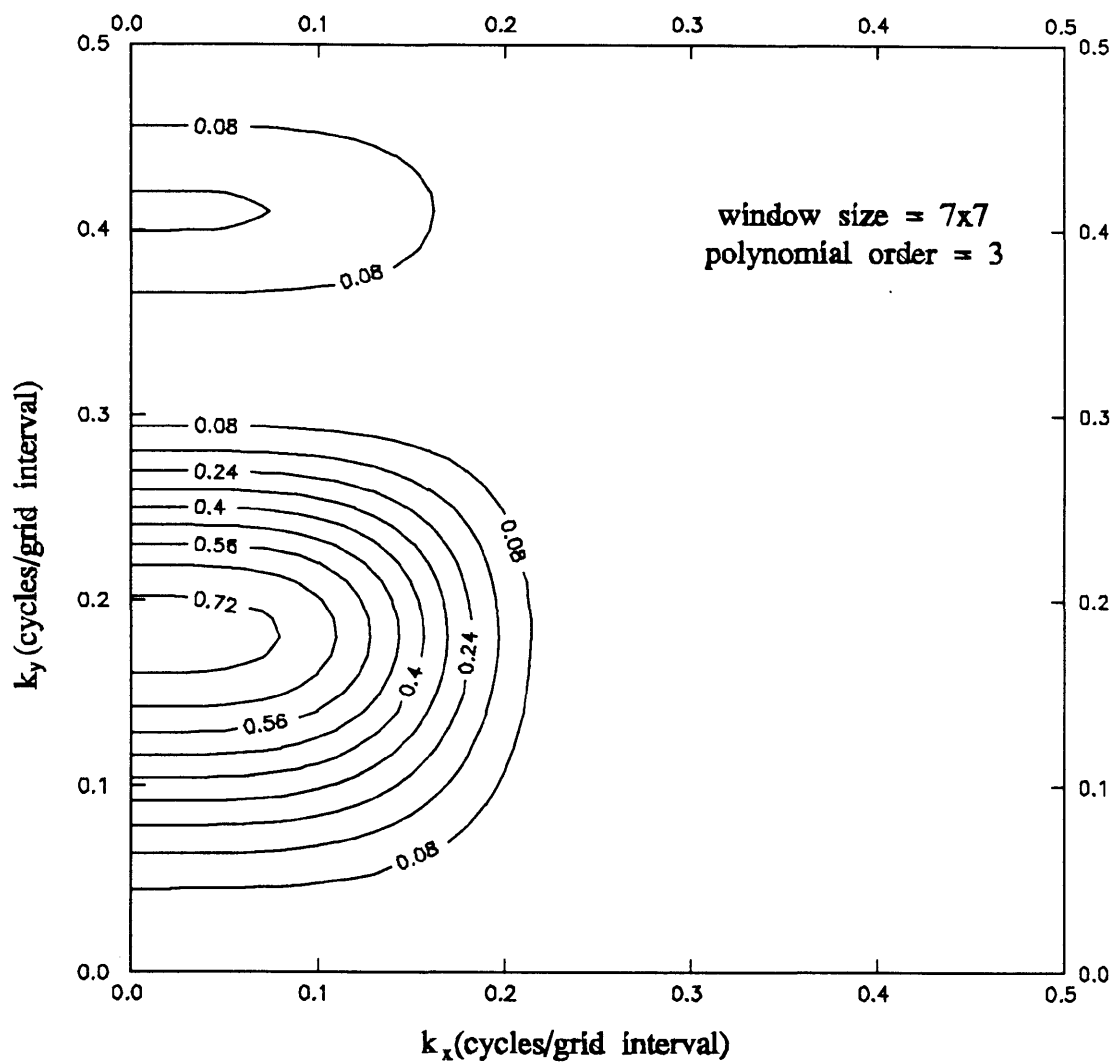
(c)
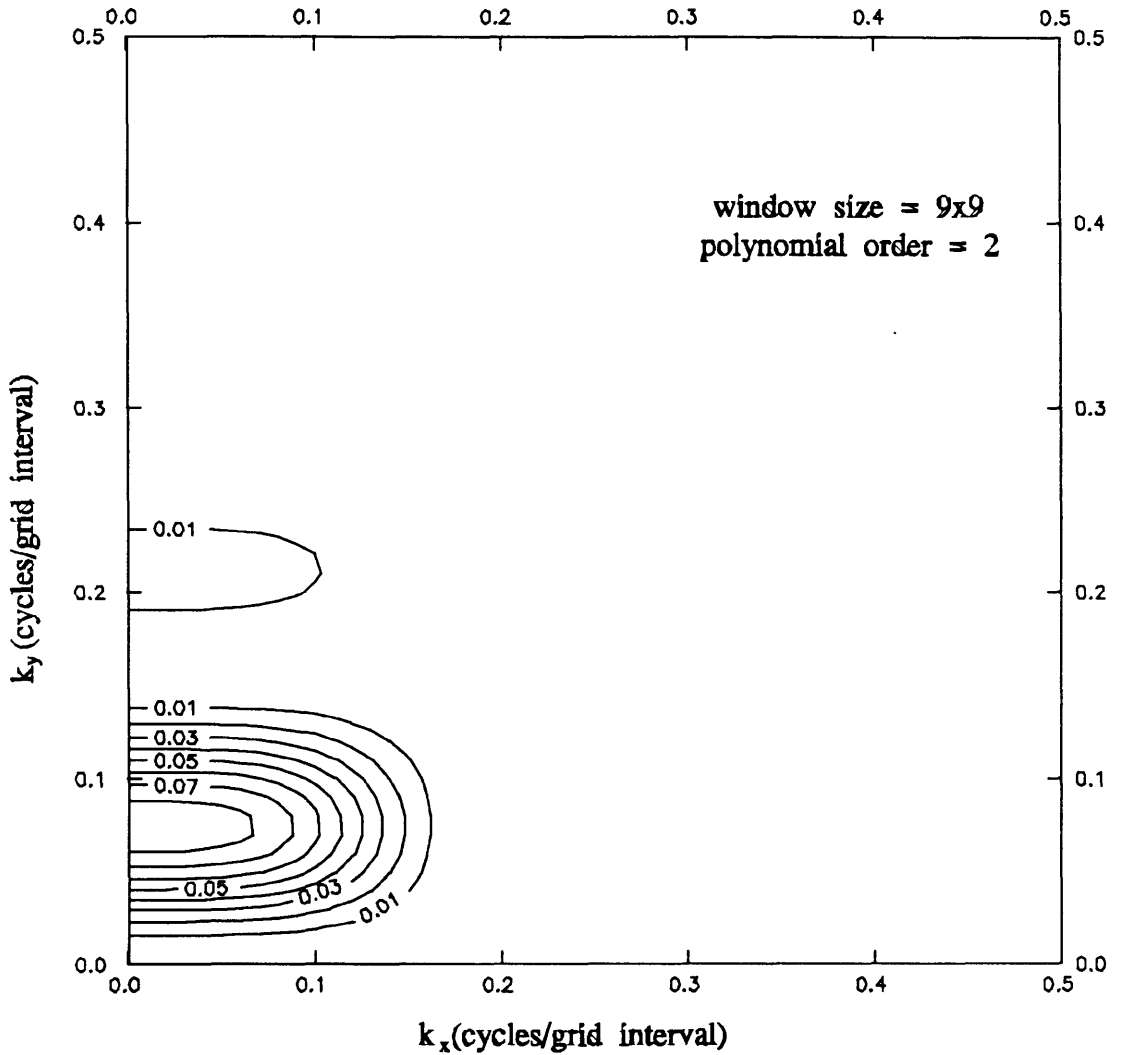
(a)

Figure 3.9. Transfer function of the y-component gradient operator for a 9x9 (a) and an 11x11 (b) window, and a second-order polynomial.
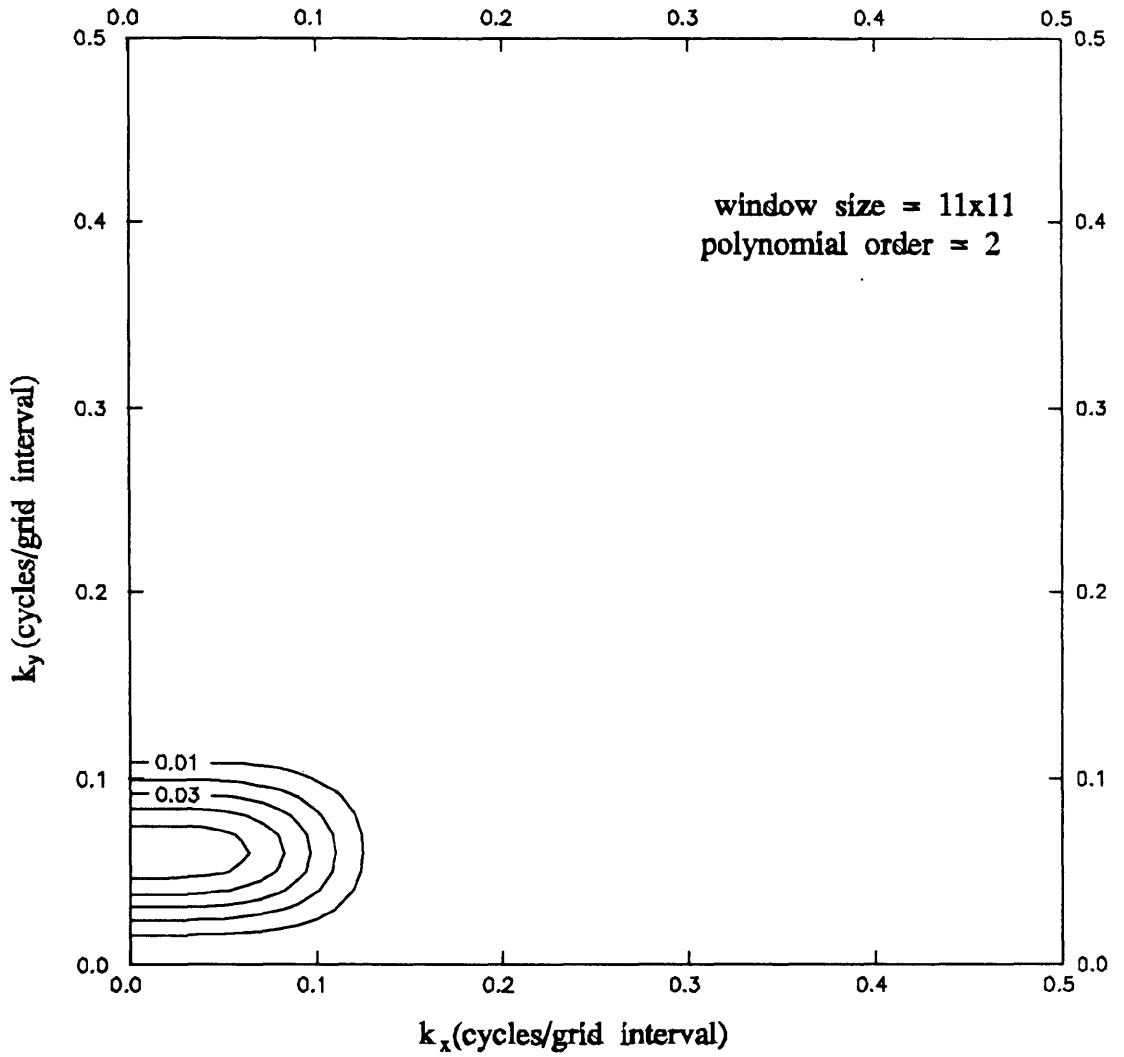
(b)

3.10. These data were obtained by empirically estimating the limits of the passband for a range of window sizes and polynomial orders. Because these filters are band-pass with respect to one frequency axis, and low-pass with respect to the other, a complete specification of the filtering characteristics would require determining the low- and high-pass frequencies of the band-pass filter, as well as the pass frequency of the low-pass filter. These data are awkward to display and require a prohibitive computational effort. It is considerably simpler to determine only the characteristics of the band-pass filter. Thus, the passbands were measured from the amplitude spectra of y-component operators along the k_y axis (i.e. for k_x equal to zero). This approach gives reliable estimates of the anticipated frequency content. If y-component operators are considered, then for polynomial orders of n and $n+1$ (for $n= 1,2,...$) the amplitude response of the band-pass filter is not altered. This is demonstrated by figures 3.8a and b. These amplitude responses indicate that maintaining a window size of 7x7, and increasing the polynomial order from one to two, increases only the frequency content in the k_x direction. Thus, measurements of band-pass frequencies were performed for filters derived from odd-order polynomials.

The abscissae in figures 3.10a-c are labelled k_y. However, because of the symmetry of the amplitude spectra of the x- and y-component operators, these results are identical to measuring passbands of x-component frequencies along the k_x axis. Thus the results apply equally to x- and y-component gradient filters.

Figures 3.10 display some interesting characteristics of these gradient-

first-order polynomial

high-pass wavenumber

low-pass wavenumber

window size

k_y(cycles/grid interval)
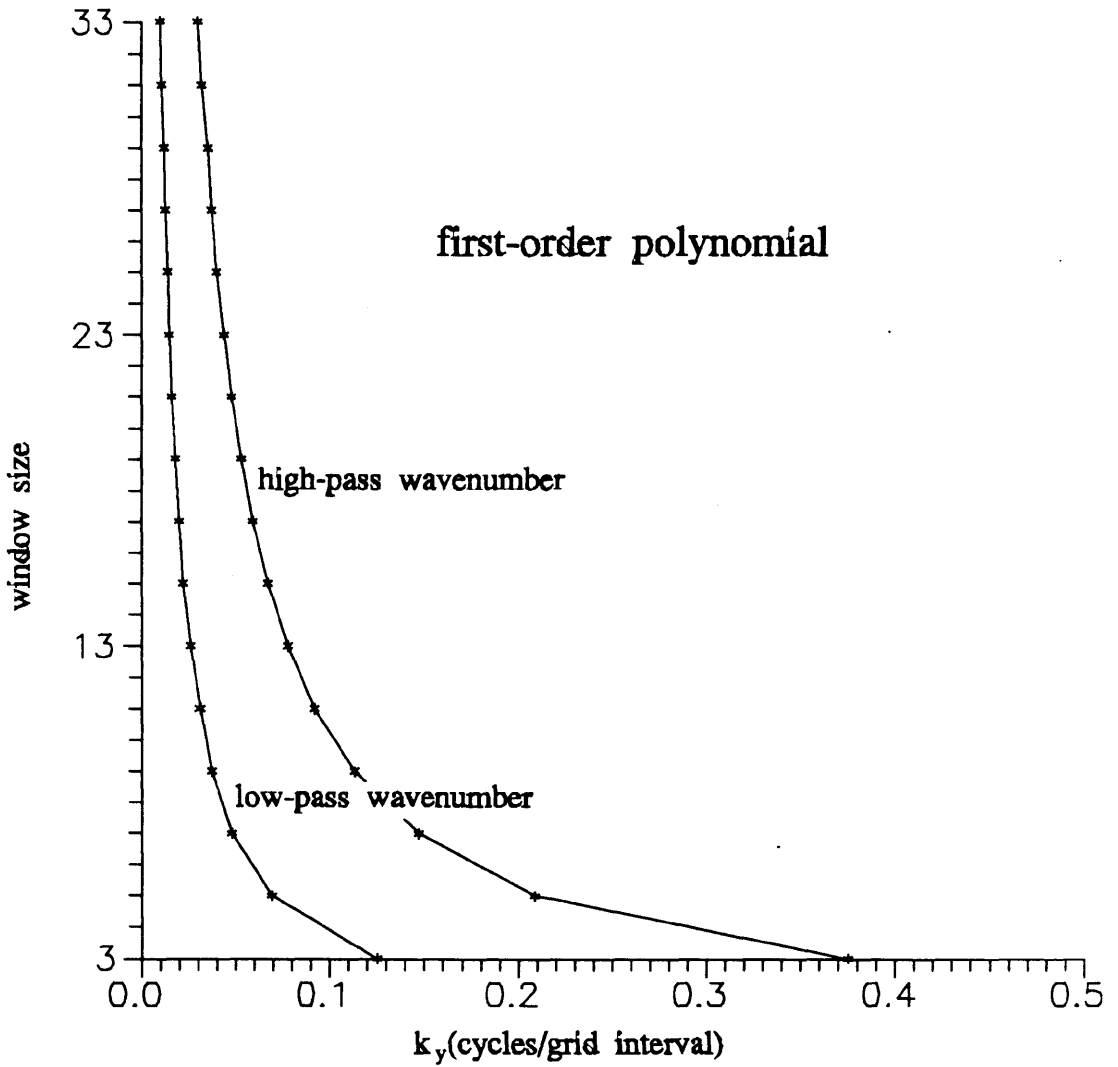
(a)

Figure 3.10. Low- and high-pass wavenumbers of gradient operators, for a first- (a) and third-order (b) polynomial, and the associated pass-band widths (c).

third-order polynomial

high-pass wavenumber

low-pass wavenumber

window size

k_y(cycles/grid interval)
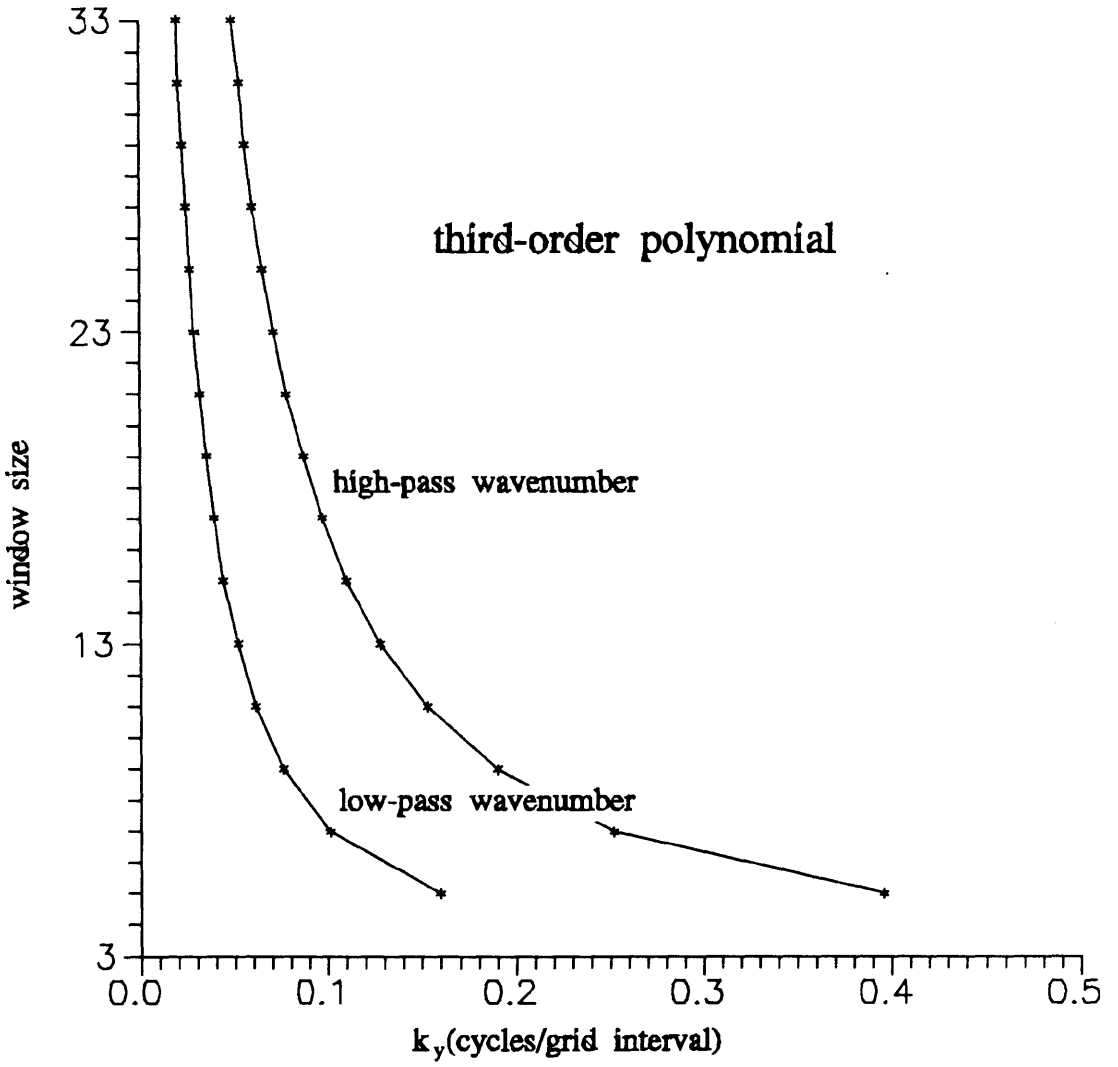
(b)
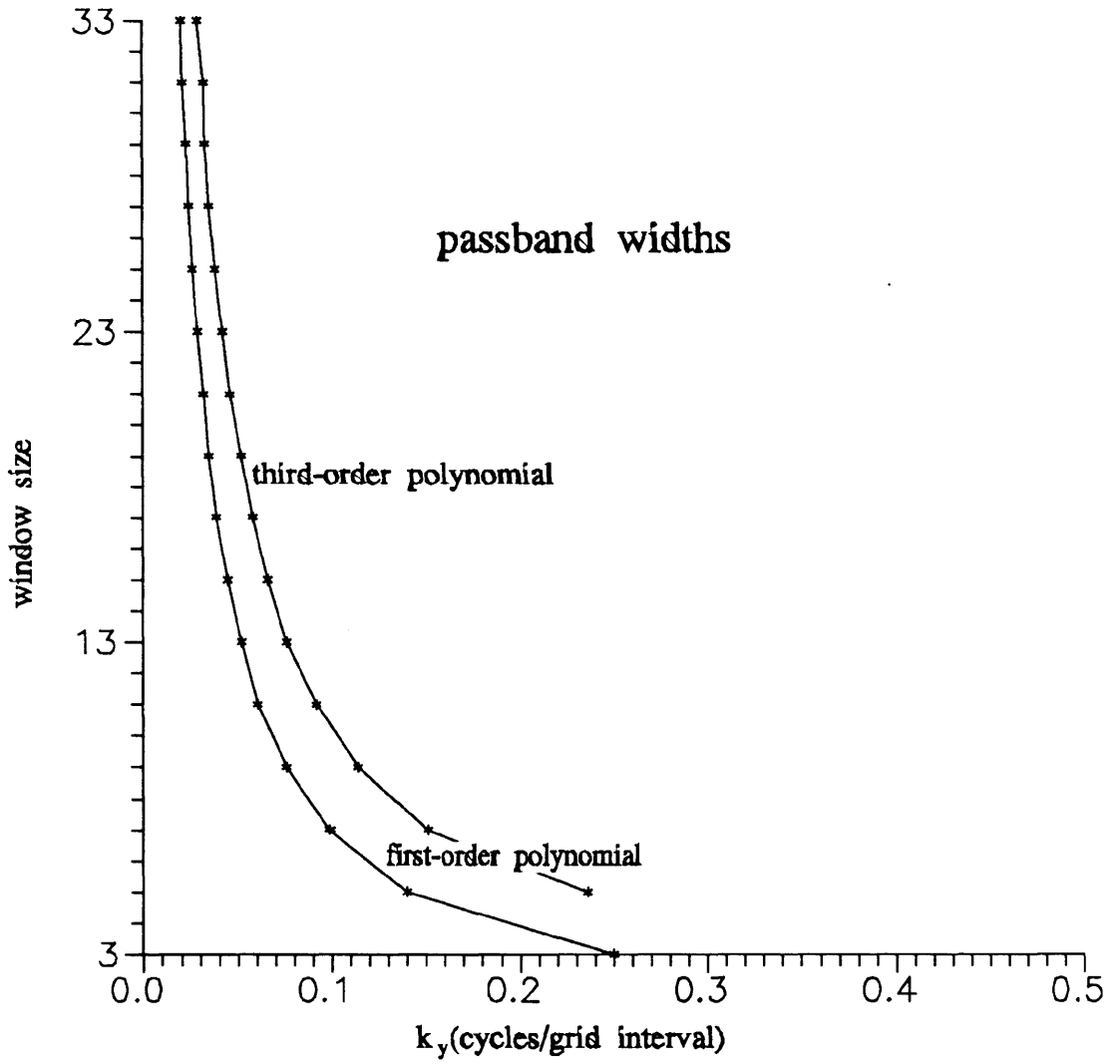
(c)

component operators. First, these plots provide an estimate of the frequency content of data filtered by a weight function of a given polynomial order and window size. This serves as a guide for selecting parameters according to the objectives of the study, as well as indicating the frequencies represented on gradient data. In addition they indicate the manner in which the filtering characteristics vary with window size and polynomial order. On all three plots, the curve becomes steeper for increasing window size. The implication of this is that the low- and high-pass frequencies and the width of the passband are relatively insensitive to variations in window size when the window size is large. Conversely, when the window size is small, these three quantities can be varied considerably by changing the window size. The transition between large and small windows occurs between 11x11 and 15x15.

Summary

The preceding discussion has demonstrated that reliable gradient-component operators can be generated by differentiating the local least-squares polynomial operators presented in chapter 2. It seems that these weight functions are more reliable than their wavenumber-domain-designed counterparts, and, unlike the finite difference operators, have a variable passband.

Quantification of the filtering characteristics of the local least-squares polynomial separation and gradient-component operators sets the stage for evaluation of these filters via application to real data. Such a study comes after the next chapter, which focuses on an analysis of the data using conventional wavelength filtering.

Chapter 4 - Wavelength Filtering of Bouguer Gravity Data

Introduction

The processing techniques based on polynomial approximation have been applied to a Bouguer gravity data set from northern Alberta. The data used for this study are based on 440 Bouguer gravity values from the Earth Physics Branch, Department of Energy Mines and Resources, Canada. Corrections to the data are described in detail by Goodacre et al. (1987). The Bouguer density used for the reduction is 2670 kg/m^3. Terrain corrections have not been performed, as for these data this is less than 1 mGal (Walcott and Boyd, 1971). To facilitate digital computations and automated display, the data were gridded at an interval of 2.5 km. The gridded data set comprises 101x101 grid points, and covers a square area of 62 500 km^2.

A contour map of these data is shown in figure 4.1. An initial analysis has been undertaken using conventional filtering techniques. The results of this filtering constitute the topic of this chapter. The purpose of this is to determine likely source bodies that give rise to the regional and residual anomalies. These results provide an understanding that will serve as the foundation for the subsequent study that employs polynomial approximation techniques.

Regional and residual anomaly maps

A suite of low-pass filtered (i.e. long-wavelength) maps and the associated
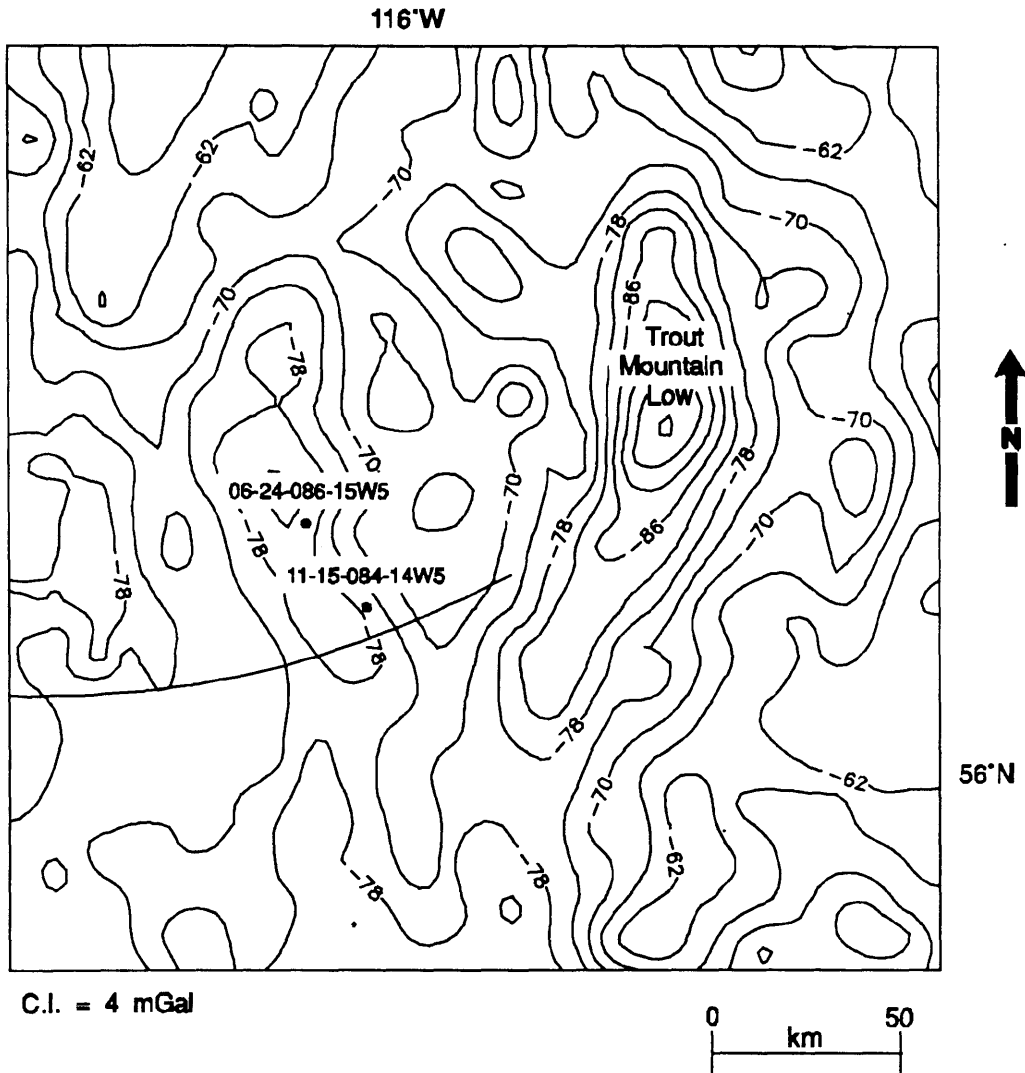
Figure 4.1. Bouguer gravity map of the study area, comprising the Trout Mountain Low. The two solid circles indicate basement-penetrating wells (after Ross et al., 1988), and the solid line indicates the Devonian axis of the Peace River Arch.

residuals has been computed. Filtering was performed in the frequency domain with a sixth-order Butterworth filter (Kanasewich, 1981, p. 265) using software developed by Eaton (1988). The order of the filter is proportional to the slope of the taper. For sixth order, the average slope is approximately 8 dB per octave. This slope effectively separates frequency components, and ringing artifacts induced by this rapid taper are not evident in the filtered data. In order to minimize edge effects, filtering was performed over a data set containing 181 grid nodes per side. The outermost 40 points along each edge of the map were discarded, leaving a window of 101x101 points. Filtered data were computed for cutoff wavelengths up to 1000 km. When wavelengths shorter than 1000 km are eliminated the output is uniform at approximately -70 mGal. For cutoff wavelengths shorter than about 30 km no coherent signal is apparent. Shown in figure 4.2 are the data filtered with cutoff wavelengths of 31.25 km, 62.5 km, 125 km, 250 km, and 500 km. These correspond respectively to spatial frequencies of 0.032 km^{-1}, 0.016 km^{-1}, 0.008 km^{-1}, 0.004 km^{-1}, and 0.002 km^{-1}. Where possible the discussion of the filtered data focuses on suggesting sources for the anomalies by correlation of the regional and residual anomaly maps with crustal features identified in related published studies.

$\lambda_c = 31.25$ km
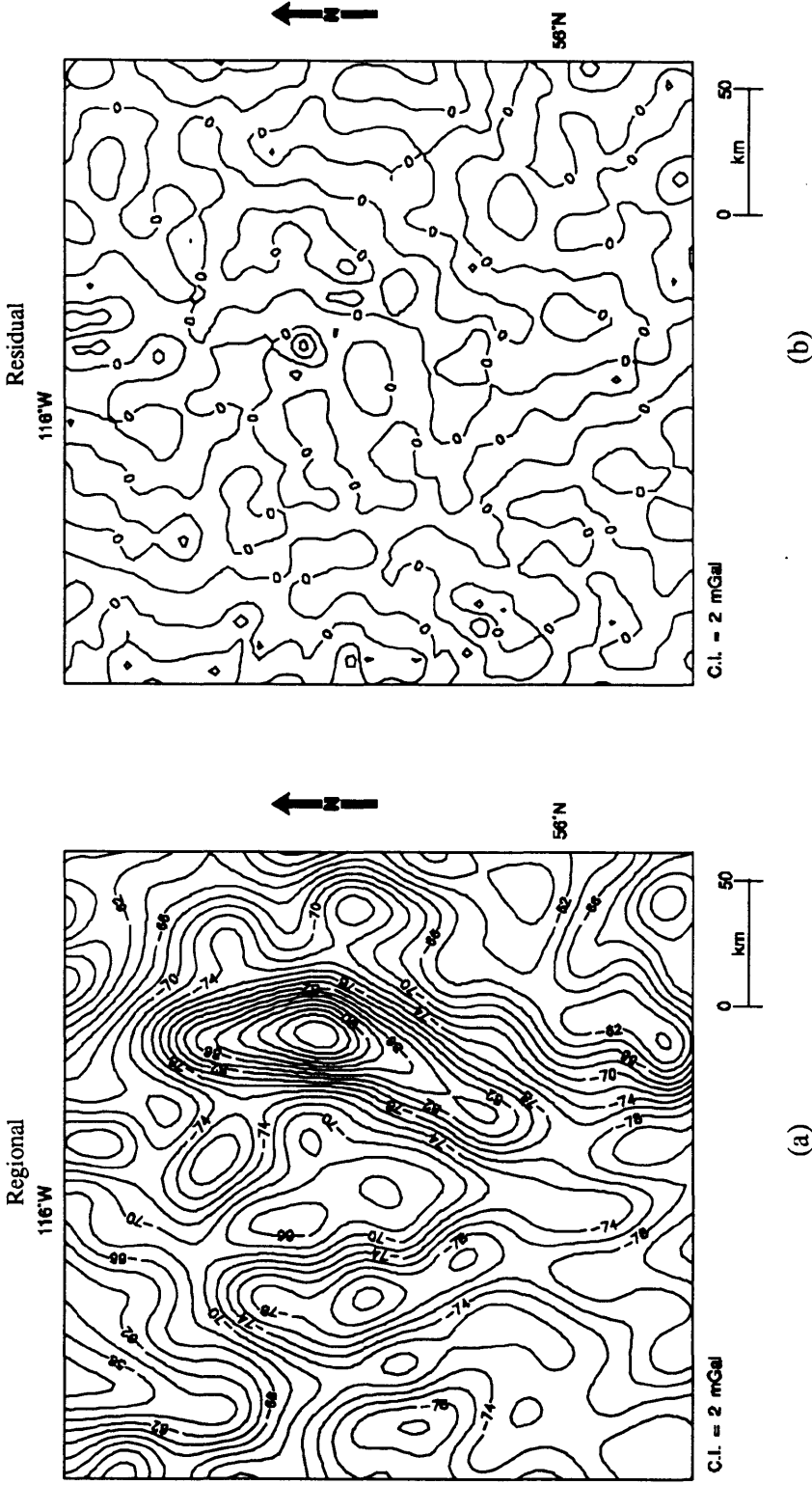
Figure 4.2. Low-pass filtered (a,c,e,g,i) and residual of low-pass filtered (b,d,f,h,j) Bouguer gravity data. λ_c denotes cutoff wavelength.

$\lambda_c = 62.5$ km
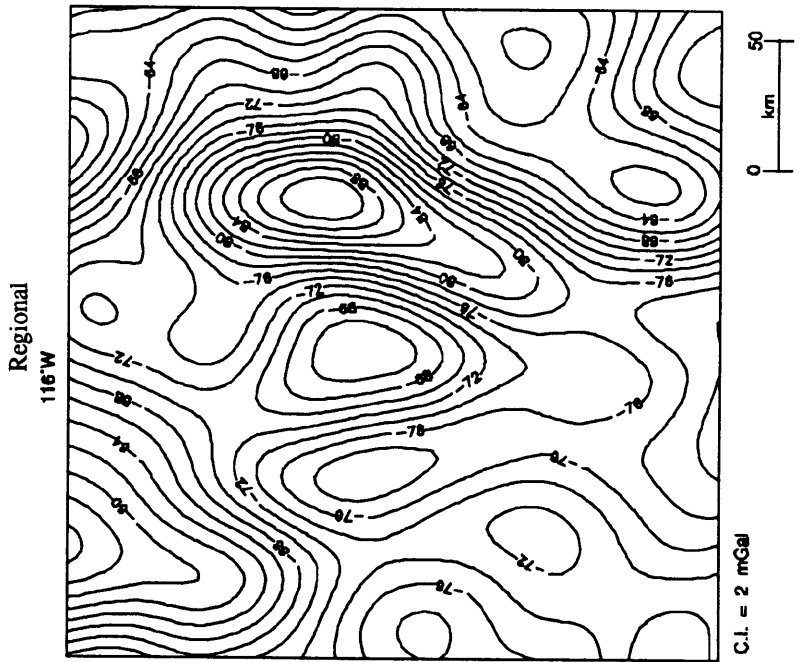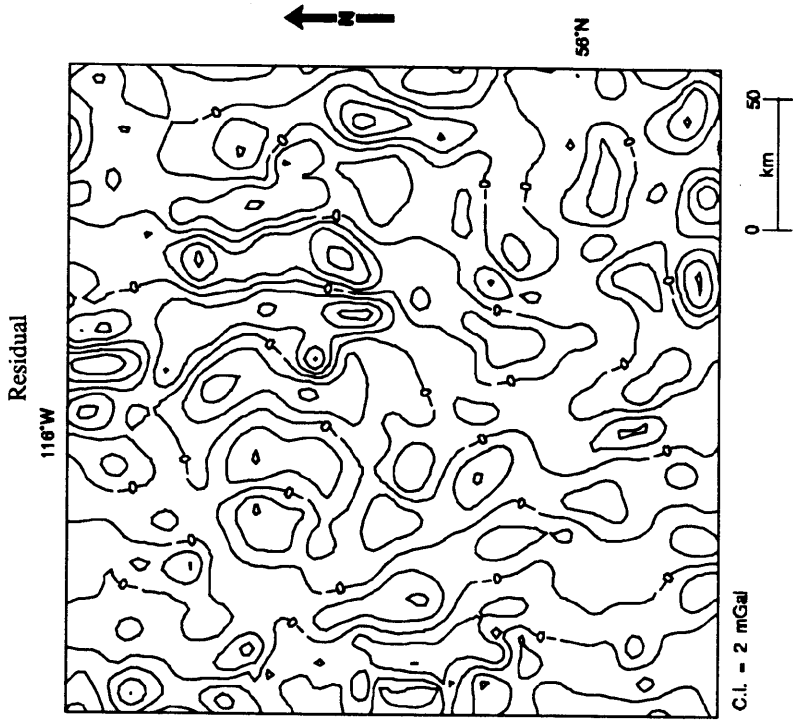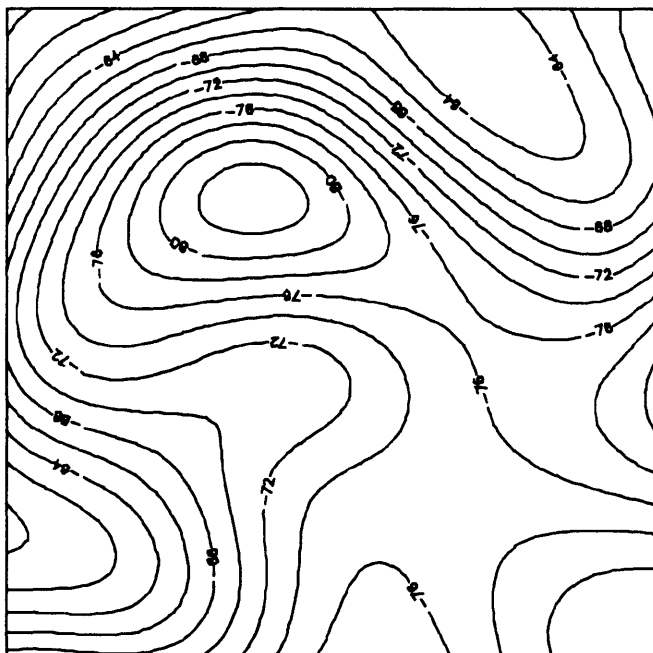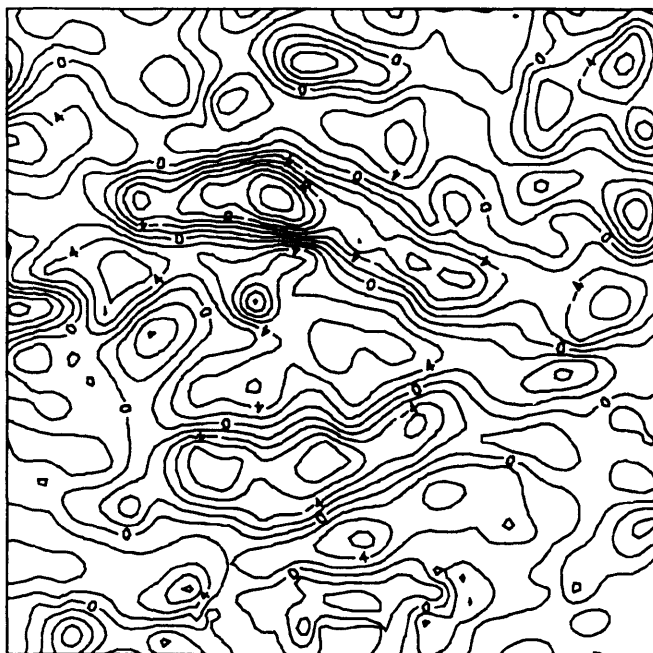
Residual

116°W

56°N

C.I. = 2 mGal

(d)

Regional

116°W

56°N

C.I. = 2 mGal

(c)

$\lambda_c = 125$ km

(f) Residual

(e) Regional

$\lambda_c = 250$ km

(h)

Residual

116°W

56°N

C.I. = 2 mGal

(g)

Regional

116°W

56°N

C.I. = 2 mGal

$\lambda_c = 500$ km

Residual

116°W

56°N

C.I. = 2 mGal

(j)

Regional

116°W

56°N

C.I. = 2 mGal

(i)
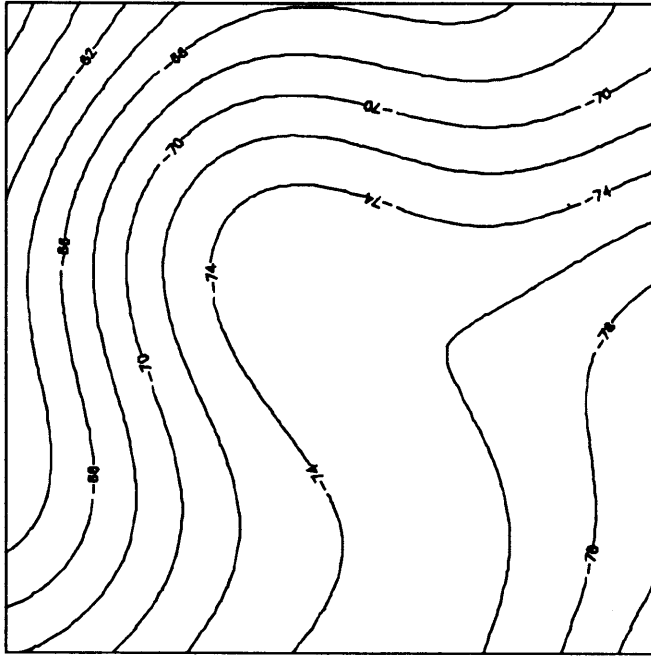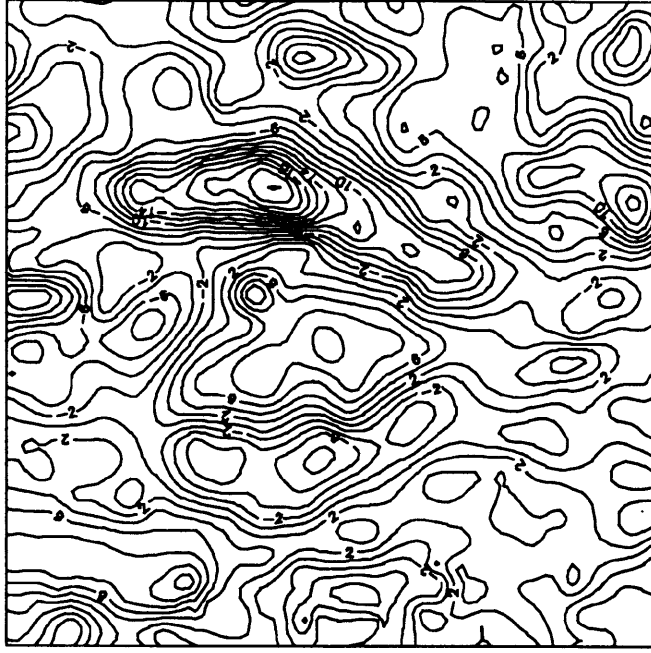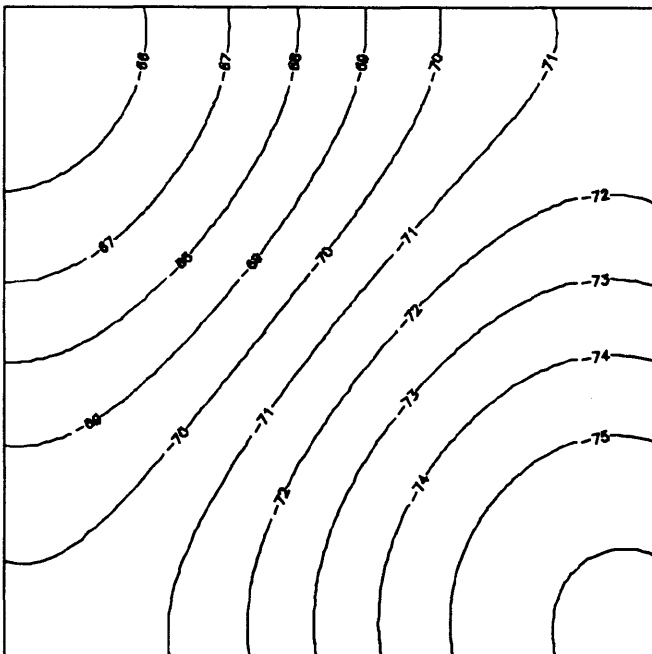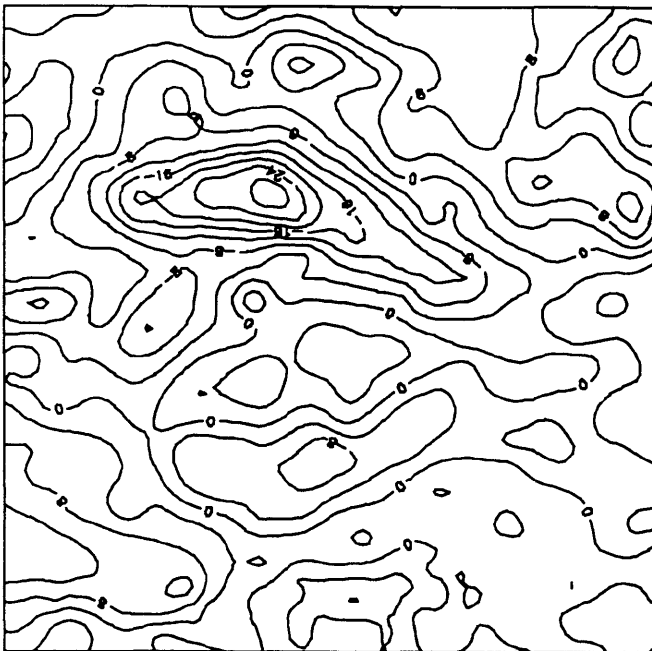
Long-wavelength anomaly maps

Kane and Godson (1985) studied attenuation caused by filtering, and concluded that anomaly maps containing wavelengths predominantly shorter than 250 km depict sources at less than 40 km depth. As a corollary to this, the first-order influence on the long-wavelength maps with cut-offs greater than 250 km will be upper mantle sources. It is also possible for large-scale shallower sources to give rise to anomalies with wavelengths longer than 250 km. In addition, the 125-km, 62.5-km, and 31.25-km, long-wavelength maps, shown in figures 4.2 b,d, and f, also include crustal sources. This assumption is based on the same reasoning used by Kane and Godson (1985) and figure 3 from their paper, which suggests that anomaly maps containing wavelengths shorter than 125 km include sources at depths less than about 15 km. The long-wavelength counterparts of these maps will thus include anomalies residing generally in the lower part of the crust. Consequently, this study of regional maps highlights mantle anomalies, crustal anomalies with broad areal extent, as well as smaller crustal bodies.

The map comprising wavelengths longer than 500 km, shown in figure 4.2i, depicts a negative gradient, with a relative high to the northeast; and a relative low to the southwest. If the base level of -70 mGal, corresponding to the output of the 1000-km low-pass filter, is subtracted from these filtered data, the northeastern portion of the map corresponds very closely to the middle-wavelength (500-1000 km band-pass filtered) Airy anomaly map of Sprenke and Kanasewich (1982). The fact that this feature is resolved on an isostatic anomaly map implies that this portion of the map

area is probably not in isostatic equilibrium. These authors surmised that this anomaly

is a relict of the Hudsonian orogeny; and is due either to anonamously high mantle

densities or to a topographic high on the Moho.

The relative low in the southeastern portion of the map area does not have a

counterpart on the middle-wavelength isostatic map; however Stephenson et al. (1989)

attributed this trend to crustal thickening beneath the Rocky Mountains (Berry and

Forsythe, 1975).

The 250-km long-wavelength map, shown in figure 4.2g, depicts a northeast-

trending relative low, centred approximately in the middle of the map, superimposed

on the longer-wavelength gradient seen on the 500-km long-wavelength anomaly map.

Burwash and Culbert (1976) identified a regional trend of increase in potassium

feldspar, accompanied by a decrease in specific gravity, towards the northeast. This

regional density trend closely resembles the shape, location, and orientation of this 250

km long-wavelength low. This density decrease was recognized from trend surface

analysis of potassium-feldspar and quartz mode observations, and specific gravity

measurements obtained from Precambrian rocks sampled in deep drill holes. These

authors attributed this to potassium metasomatism of crystalline basement rocks,

causing a decrease in specific gravity. This in turn was postulated to be related to the

positive isostatic nature of the Peace River Arch. If this density decrease is vertically

extensive it may give rise to the 250 km long-wavelength low.

The 125-km long-wavelength map, shown in figure 4.2e, is dominated by the

long-wavelength component of the Trout Mountain anomaly (discussed below).

Relative gravity highs in the southeastern and northwestern corners of this map have unknown origins. On the other hand, the axis of the saddle-shaped relative low in the southwestern quadrant of the map, with an amplitude of approximately 4 mGal, is coincident with the Devonian axis of the Peace River Arch. Stephenson et al. (1989) resolved a coincident low on a 400 to 700 km band-pass filtered isostatic anomaly map. These authors attributed this low to crustal thickening that could not be accounted for by a topographic high. It is possible that this is the cause of this anomaly; however, it also possible that this has an origin similar to the low on the 250-km long-wavelength data.

Short-wavelength anomaly maps

The aim of generating short-wavelength anomaly maps is to produce residuals which isolate crustal source bodies. This entails removing broad anomalies. For the present Bouguer gravity data, the broad anomalies are primarily due either to regional crustal density trends or to upper-mantle features, and can be represented by wavelengths greater than 250 km. In addition, as previously stated, bodies giving rise to anomalies with wavelengths less than 250 km generally reside at depths less than 40 km. Hence, the residual field for these Bouguer gravity data should depict specific bodies of relatively limited extent that are in the crust. Thus, crustal sources are depicted on the 250-km and 125-km residual maps (figures 4,2f and h respectively). The 62.5-km and 31.25-km residuals contain, shown in figures 4.2c and a respectively, little useful information, as will be discussed.

On the map shown in figure 4.2h the most prominent feature is an approximately 170 km x 60 km north-south (in the northern portion) and southwest-northeast trending (in the southern portion) low. This anomaly was first identified by Walcott and Boyd (1971). They designated it the Trout Mountain Low (TML), and surmised it to be due to a major lithologic change in the upper part of the basement, possibly associated with a granitic batholith. Burwash and Power (1990), using a suite of cores that intersect both the TML and the adjacent Precambrian basement, carried out detailed gravity modelling of this feature. They concluded that the TML is a granitic pluton, embedded in granulite-facies country rock. Based on these borehole samples, their model was constrained to have a density contrast of -0.05 g/cm^3 and a top depth coincident with the unconformity at the Precambrian surface. From these assumptions Burwash and Power obtained the following parameters for the source body: the northern segment is a steep-sided body, 25 km thick, trending north-south with a width at the base of 20 km. The southern segment trends N25°E with a base width of at least 30 km, and is not as well defined.

Apart from the TML, determining source bodies for the residual anomaly maps is speculative; however, assuming that these represent crustal sources, it is possible to make some general statements.

A common cause of gravity lows is granitic batholiths (Bott and Smithson, 1967). West of the TML there is a similar, albeit smaller-amplitude, north-south trending (in the northern portion), and southeast-northwest trending (in the southern portion) gravity low with a minimum amplitude of approximately 8 mGal. The

basement rocks corresponding to this anomaly have been intersected by two wells (Ross et. al., 1988) whose locations are shown on figure 4.1. These authors describe the core from the 06-24-086-15W5 well as quartz monzonite, and the core from the 11-15-084-19W5 well as granite. This lithology is similar to the TML basement cores, which were described by Burwash and Power (1990) as microcline-rich granite. As well, Ross et al. (1988) dated the core from the 06-24-086-15W5 well at >1995 Ma, an age similar to that of the rocks of the TML. While two samples do not provide sufficient control to draw firm conclusions, the lithologic, shape and age similarities, as well as the proximity to the TML, suggest that this body is also a granitic batholith, with a similar history as the TML.

In general, the 125-km short-wavelength map (figure 4.2f) bears a strong resemblance to the 250-km map (figure 4.2h). A significant difference is that the amplitude of the TML is lower on the 125-km residual map. This can be explained by the fact there is a long-wavelength component of the TML evident on the 125-km long-wavelength map. On the other hand, the smaller low is essentially the same on the 125-km and 250-km long-wavelength map. This is explained by the fact that this smaller pluton is wholly represented by wavelengths less than 125 km, and is affected very little by including signal with wavelengths between 125 km and 250 km. The absence of longer-wavelengths associated with this pluton implies that it does not extend as deep as the TML.

It should be noted that on the 250-km and 125-km residual maps (figures 4.2f and h respectively) the southwestern portion of the TML and both sides of the

adjacent pluton are flanked by parallel highs. Zurflech (1967) and Kane and Godson (1985) demonstrated that artificial anomalies of opposite polarity and the same orientation can be induced on the flanks of real features when Bouguer gravity data are high-pass filtered. Because there is no evidence for these linear features on the Bouguer anomaly map, it is quite likely that these are artefacts of the filter.

There is limited useful information on the 62.5-km short-wavelength map. The highest amplitudes can be traced to leakage of the high-amplitude longer-wavelength anomalies. In addition, there are a number of isolated peaks; however, these are generally less than 36 km from flank to flank, and thus will are unreliable, as the average station spacing is 12 km.

Finally, the 31.25 km short-wavelength data are of low amplitude and incoherent. Hence the threshold for signal for these Bouguer gravity data is taken to be about 0.032 km^{-1}.

Summary

Frequency filtering of the Bouguer gravity data has separated a number of trends that can be attributed to known crustal-scale features. In general, the contributions are well understood, with the exception of the small-scale crustal sources, which would require the incorporation of additional information and which is beyond the scope of this investigation. This study is intended primarily as a precursor to analysis via the polynomial approximation techniques. These approximation techniques encompass local and global least-squares approximation, as well as

transformation with horizontal-gradient component filters. Frequency filtering has highlighted the salient features of these Bouguer gravity data. In the following chapter these will be processed using polynomial approximation techniques. This will include two main components. The first is to undertake regional and residual separation with global and local least-squares approximation and to compare these results to the filtered data with similar frequency content. The purpose of this is to assess the consistency of these separation techniques. The second entails computing a suite of horizontal-gradient magnitude data sets in order to determine whether this approach enhances the results of the filtering.

Chapter 5 - Application of Polynomial Approximation Filters

Introduction

In this chapter, the filtering techniques studied in chapters 2 and 3 are applied to the Trout Mountain Bouguer gravity data. There are two main sections: application of polynomial approximation for estimating regionals, and computation of a suite of horizontal-gradient magnitude maps. The results of these filtering operations will be compared to the results of the wavelength filtering.

Application of global and local polynomial approximation methods is an attempt to reproduce the regional fields computed in the previous chapter. Understanding the filtering characteristics of the polynomial approximation methods aids in the computation of regionals which are equivalent to the wavelength-filtered maps in terms of frequency content.

The focus of the horizontal-gradient magnitude analysis is to construct maps in which bandwidths ranging from the threshold of coherent short-wavelength signal to the longer-wavelength crustal sources are emphasized. Because the filtering characteristics of the gradient-component filters are understood, it is possible to generate maps comparable to the wavelength-filtered maps. Knowing the frequency content of the gradient-magnitude maps facilitates evaluation of the horizontal-gradient magnitude technique, as well as enhancing the interpretation.

Regional/residual separation using polynomial approximation

In chapter 2 the filtering characteristics of global polynomial approximation were discussed. This analysis showed that the frequency content of these regional fields varies from point to point, making it difficult to generate maps suitable for comparison with wavelength-filtered maps. However, by using the passbands of centre filters as a guide and experimenting with various polynomial orders and data-set sizes, it is possible to generate results that resemble the wavelength-filtered maps. Thus, polynomial approximation was performed over large data sets, from which smaller cores were extracted. Windowing the map has the additional benefit of eliminating effects induced by the unreliable filtering characteristics in the vicinity of the edges.

From a mathematical standpoint, local least-squares polynomial fitting and wavelength filtering are equivalent operations, and thus differences that arise can be attributed to the differences in the transfer functions of the filters. In chapter 2, it was demonstrated that local polynomial filters bias signal at 45° to the coordinate axes. As a result, the frequency content of maps generated with local least-squares polynomial filters can not identically match the wavelength-filtered maps. Where possible, filter functions were designed to accommodate the dominant trends, with parameter selection based on the results of the passband measurements presented in chapter 2.

The algorithm implemented for global polynomial fitting is based on computing the coefficients in terms of orthogonal polynomials. The coefficients are computed from equation 2.12, and the long-wavelength component is calculated by using these coefficients in equation 2.11. Local least-squares polynomial approximation was

implemented as a convolution process, with the coefficients of the weight functions computed using equation 2.15.

Regional fields were generated using these algorithms, with polynomial forms defined by both equations 2.1a and b, for comparison with the 125-km and 250-km long-wavelength anomaly maps from figures 4.2e and g. It is important to remember that polynomials defined by equation 2.1b include higher-order cross terms that result in increased high-frequency content of signal that is oblique to the coordinate axes. The former are shown in figures 5.1 and 5.2, and the latter are shown in figures 5.2 and 5.3. Each figure comprises two maps depicting polynomial approximation with both polynomial types. Figures 5.1a and b show the result of approximating 181x181 points with eleventh-order polynomials, and figures 5.3a and b show third-order polynomials computed from a 151x151-point data set. Regional fields computed using local least-squares polynomials are shown in figures 5.2a and b (57x57 window, and a second-order polynomial), and in figure 5.3 (45x45 window, and a first-order polynomial). Only one result is shown for the first-order local least-squares operator as, for first order, identical operators are given by both polynomial types.

data-set size=181x181

order = 11
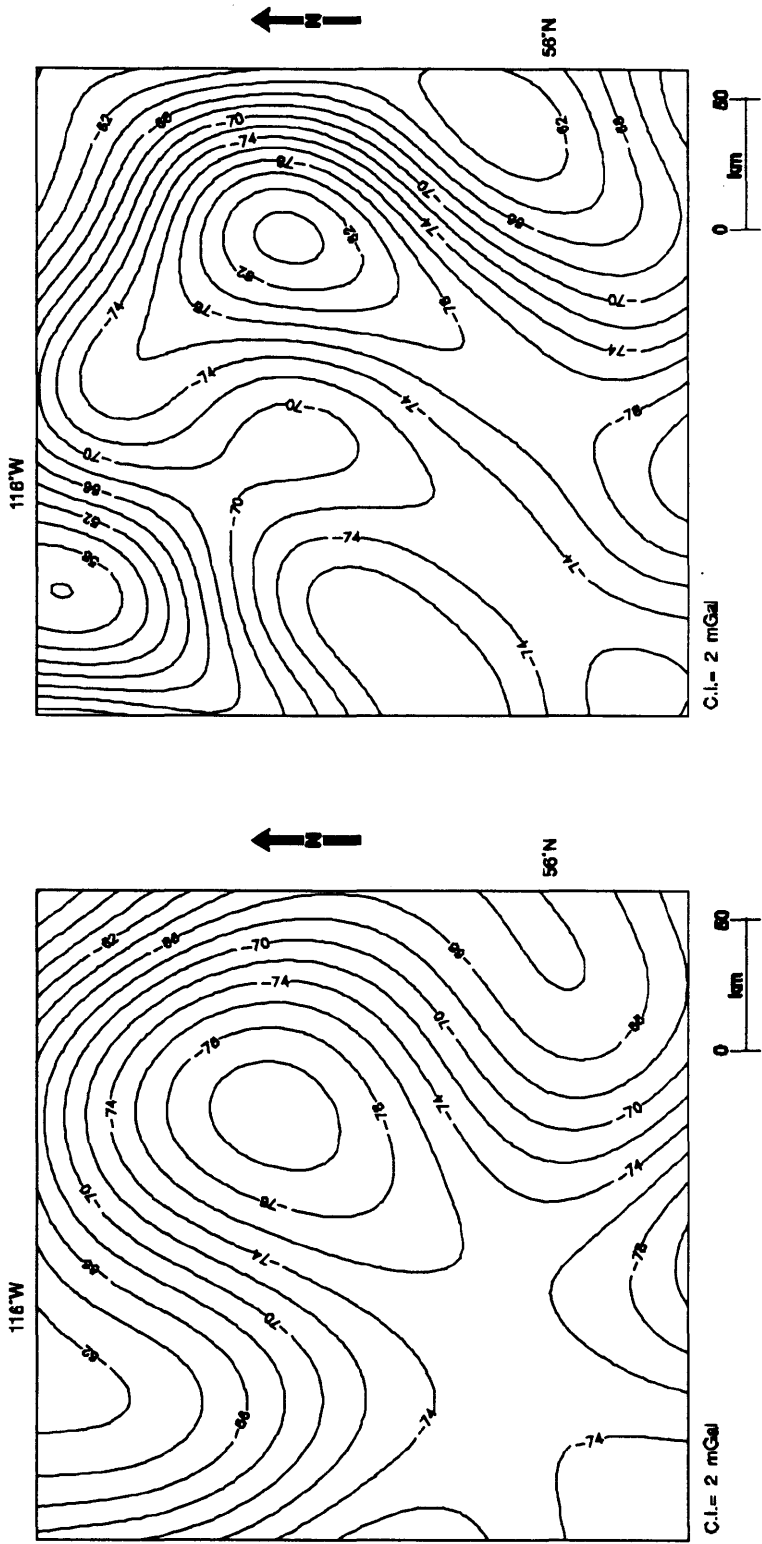
(a)

(b)

Figure 5.1. Data from figure 4.1 low-pass filtered using global least-squares polynomials defined by equation 2.1a (shown in a) and 2.1b (shown in b).

102

window size = 57x57
order = 2/3
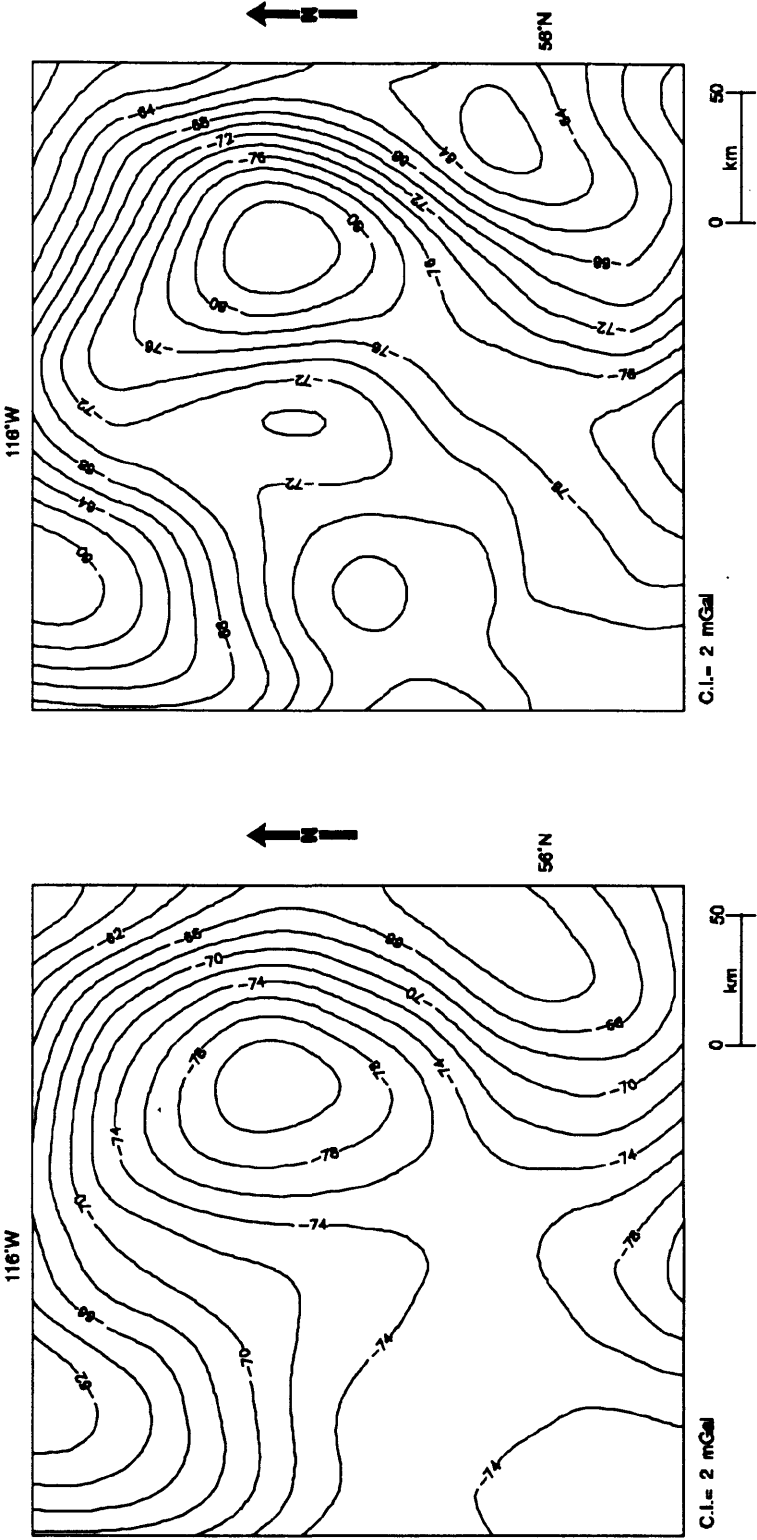
(a)

(b)

Figure 5.2. Data from figure 4.1 low-pass filtered using local least-squares polynomial filters. Polynomial types 2.1a (shown in c), and 2.1b (shown in d) are used for computing the weight functions.

data-set size = 151x151

order = 3
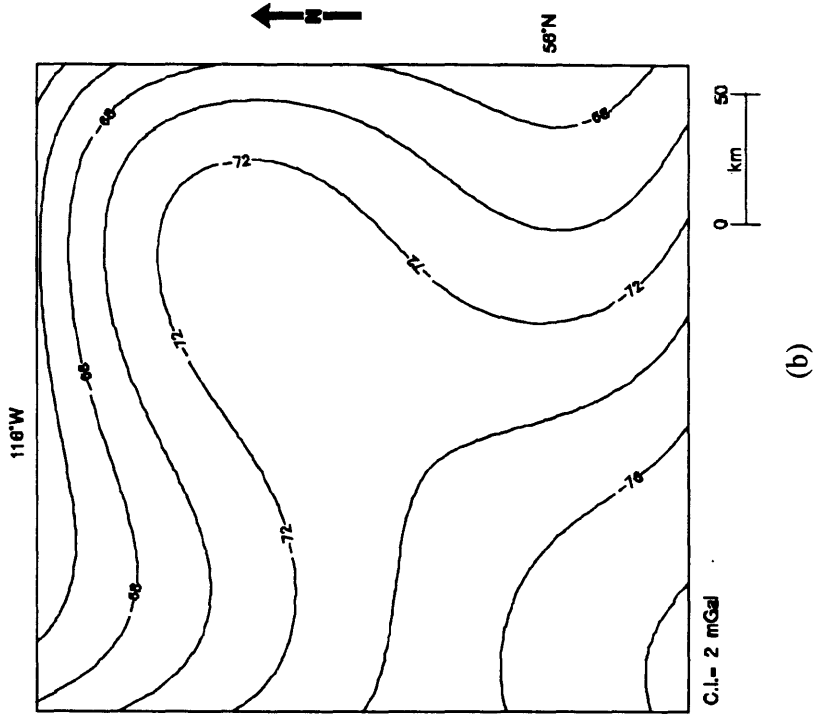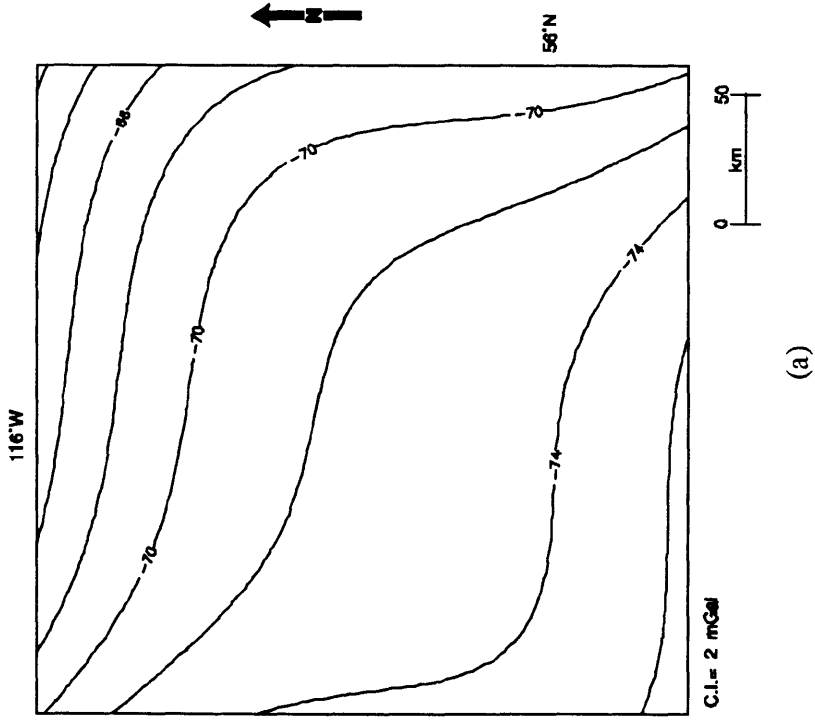
Figure 5.3. Data from figure 4.1 low-pass filtered using global least-squares polynomials defined by equation 2.1a (shown in a) and 2.1b (shown in b).

window size = 55x55
order = 0/1
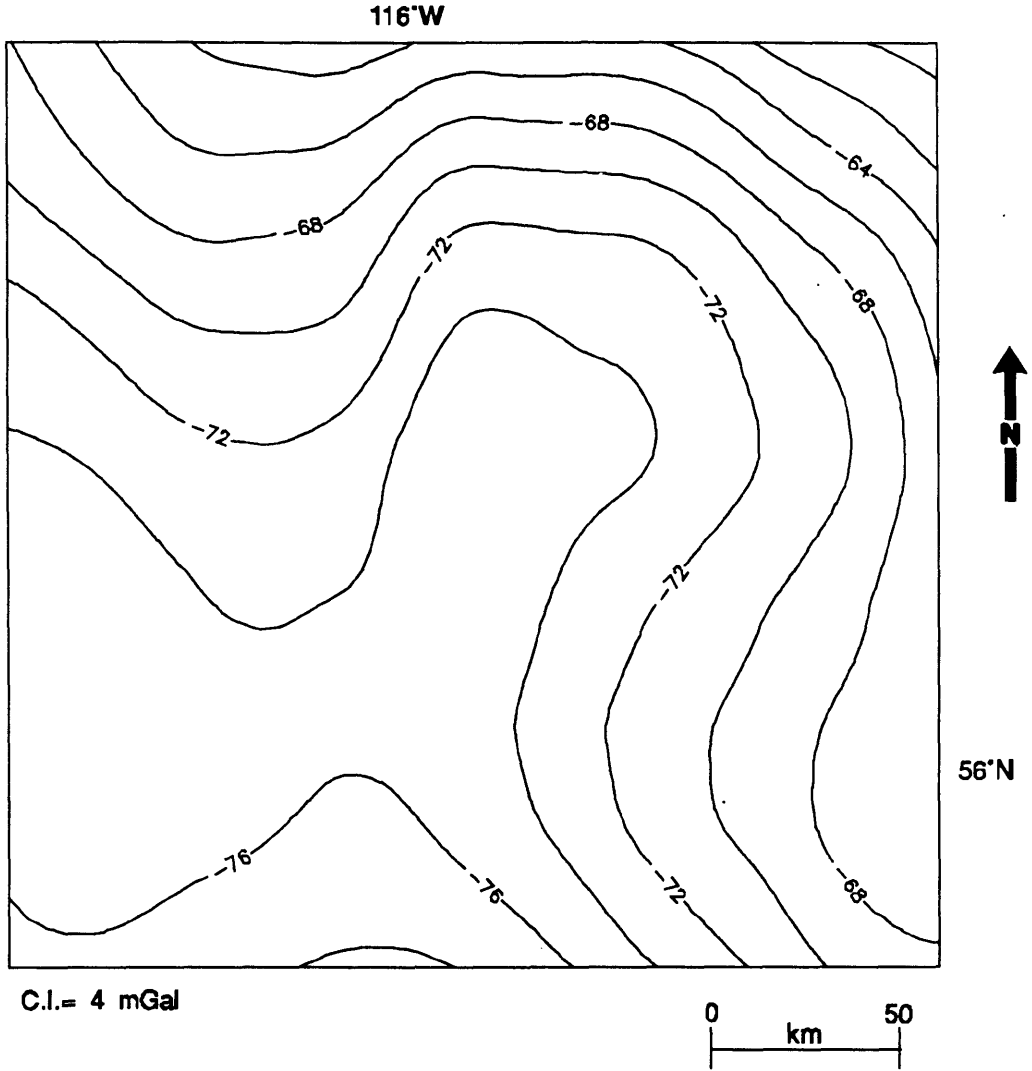
Figure 5.4. Data from figure 4.1 low-pass filtered using local least-squares polynomial filters.

Regional maps computed using polynomial approximation

No one regional field computed using polynomial approximation wholly

reproduces the 125-km long-wavelength anomaly field. The northeasterly trending low

corresponding to the TML is narrower from flank to flank on the map shown in figure

5.1b, than on the map in figure 5.1a. This implies the former comprises shorter

wavelengths. In addition, the northwestern trend characteristic of the northern portion

of the long wavelengths of this low, and the northeasterly trending extension to the

south, seen on figure 5.1b, are not present on figure 5.1a. The inability of this

polynomial-approximation method to resolve these features is not unexpected. This is

because the coordinate axes are positive to the north and to the east, and thus

approximation by polynomials defined by equation 2.1a pass considerably shorter

wavelengths in these directions. Thus, signal that is not parallel to the coordinate axes

has noticeably lower frequency content. On the other hand, when polynomials defined

by equation 2.1b are used for global approximation, frequency content is somewhat

increased for signal that is not along the axes. The result of this is that on the map

shown in figure 5.1b the long-wavelength component of the TML is more accurately

depicted.

The improved results attributed to the inclusion of extra terms in the

approximating polynomial are marred by the fact that on figure 5.1b the subtle

expression of the Peace River Arch is truncated by a northeasterly trending low. It is

difficult to explain the origin of this anomaly; however, since it is not apparent on

either the wavelength-filtered maps, or on the maps generated from local

approximation, it is quite likely an artefact. The fact that it does not appear when the data are filtered with phase-invariant filters (figures 4.2 and 5.2) suggests that it is a result of a phase shift. Further, the fact that it does not appear on figure 5.1a implies that this spurious feature is also related to increasing the high frequencies of signal that is not parallel to the coordinate axes.

It is important to note that, with respect to the 125-km long-wavelength anomaly map (figure 4.2e), the centre of the TML is shifted approximately 25 km to the northwest and 25 km to the southeast on figures 5.1a and b respectively. This may be due to the fact that global polynomial approximation is not phase-invariant; this distortion can shift the position of the body.

Computing the 125-km long-wavelength map with local polynomial approximation does not significantly change the results. One noteworthy difference is that the centre of the TML is coincident with the centre on the 125-km long-wavelength map (figure 4.2e). This is probably because local polynomial approximation is a phase-invariant operation. As well, the northeasterly trending feature in the southwest corner is no longer evident, supporting the proposition that it is related to phase distortion.

The regional field computed by local polynomial approximation, shown in figure 5.4, is the most successful at reproducing the results of the 250-km long-wavelength Butterworth filter. On this map, the amplitude and orientation of the prevalent northeasterly trend is very nearly identical to the low resolved by wavelength filtering.

Finally, it should be noted that the results obtained by using polynomials of the type of equation 2.1b are at the expense of increased computational effort. This is because these polynomials require calculating an extra $o(o+1)/2$ coefficients, as well as incorporating the additional terms in the regional polynomial calculation. This added computational burden increases for higher-order polynomials and for larger data sets. For third-order and 151x151 data points, polynomials defined by equation 2.1b required an additional one-third of the execution time than was needed to compute polynomials defined by 2.1a. For eleventh-order and 181x181 data points the execution time increased by approximately 1.8 times. The polynomial form used for local least-squares polynomial approximation has very little effect on computation time. This is because the number of terms in the approximating polynomial only increases the number of operations required to compute the coefficients of the weight function, which is a small task when compared to convolving the operator with the data.

Horizontal-gradient magnitude analysis

Kane and Godson (1985) compiled a 250-km short-wavelength anomaly map of the conterminous United States, and a horizontal-gradient magnitude map using finite differences. These authors noted that these maps are complementary. The gradient-component operators developed in chapter 3 facilitate extending computation of corresponding wavelength-filtered and horizontal-gradient magnitude maps. This is because local least-squares polynomial operators facilitate variation of the frequency

content of the gradient-magnitude maps. This allows a suite of these maps to be compiled, each featuring a different bandwidth of crustal anomalies.

The horizontal-gradient magnitude maps of these Bouguer data have been obtained by separately convolving the data with the impulse responses of the x- and y-component operators given by equation 3.13 and using these components to compute the horizontal-gradient magnitude. Parameters for horizontal-gradient component operators were chosen in order to generate gradient-magnitude maps that have frequency content comparable to the wavelength-filtered maps presented in chapter 4. Frequency content of gradient-magnitude maps were estimated using the results in figure 3.10. The gradient-component operator parameters, the estimated low- and high-pass wavenumbers, and the figure number in which the corresponding map appears, are summarized in table 5.1.

Figure	Window	Polynomial	Low-pass	High-pass
5.6	5x5	3	0.064 km^{-1}	0.160 km^{-1}
5.7	17x17	2	0.008	0.024
5.8	31x31	1	0.004	0.013
5.9	51x51	1	0.002	0.008

Table 5.1
Parameters for generating horizontal-gradient magnitude maps.

Before discussing specific features of the gradient-magnitude maps, it is appropriate to make some general comments regarding the frequency content. In chapter 3 the filtering characteristics of the gradient-component operators were discussed. This discussion focused on determining the passbands associated with

various combinations of parameters. However, irrespective of the behaviour of the filter, transforming an anomaly to its gradient-magnitude counterpart inherently alters the frequency content. This occurs because the magnitude of the gradient of an input waveform has wavelengths half as long, provided these wavelengths fall within the passband of the gradient-component operators.

This can be demonstrated by a simple example using data in a single independent variable, say x. A single wavelength (or period) of any spatial or temporal series can be represented as

$$f(x) = A\cos(\gamma x) + B\sin(\gamma x) \tag{5.1}$$

where $\gamma = 2\pi/T$, and T is the period (Jeffreys, 1964). The gradient magnitude of the function defined by equation 5.1 is:

$$\left|\frac{\partial f(x)}{\partial x}\right| = |-A\gamma\sin(\gamma x) + B\gamma\cos(\gamma x)|. \tag{5.2}$$

One way of determining the wavelengths of both functions is to find the distance between adjacent local maxima. Maxima are located by finding the roots of the first derivatives of each function, for which the second derivatives are greater than zero. For equation 5.1, this occurs for $\gamma x = \pi/4 + 2n\pi$, whereas for equation this occurs for $\gamma = 3\pi/4 + n\pi$, where $n = 0,1,2,...$ Thus, the spacing between maxima, and hence the wavelength, of the gradient magnitude is one-half of that of the input waveform. This is illustrated by figure 5.5.

This implies that wavelength-filtered maps contain essentially the same information as gradient-component maps comprising wavelengths half as long. For
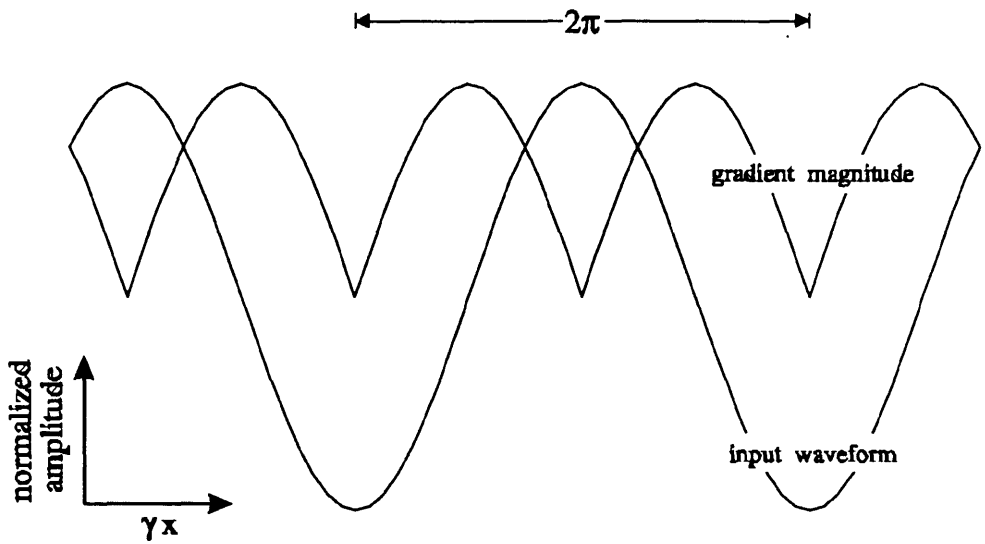
Figure 5.5. A monochromatic waveform, and its gradient magnitude. A single cycle of the input waveform spans two cycles of the gradient magnitude.

instance, gradient-component operators based on a 31x31 window and a first-order polynomial enhance wavelengths approximately between 70 km and 200 km. Thus these express the same features as wavelength-filtered maps with cut-offs between 140 and 400 km.

Horizontal-gradient magnitude maps

Shown in figure 5.6 is the gradient-magnitude map computed using a 5x5 window and a third-order polynomial. In chapter 4, 0.032 km^{-1} was determined to be the upper frequency limit of signal for these data. According to table 5.1, these gradient-component operators emphasize frequencies between 0.064 km^{-1} and 0.16 km^{-1}, a band that comprises primarily noise. However, because the noise has a magnitude that is generally less than 2 mGal, higher-amplitude lower-frequency coherent trends are evident. This is an example of high-amplitude anomalies appearing on gradient-magnitude maps, even though these anomalies are comprised of frequency bands not within the bandwidth specified in table 5.1. This can be attributed to the fact that the frequency content of gradient-magnitude maps is more complicated than is implied by table 5.1. That is, each gradient component contains a relatively small amplified frequency band in the direction perpendicular to the direction of the gradient component. This is the passband specified in table 5.1. When the components are squared and summed to compute the gradient, this band is repeated and thus constitutes the primary frequency band of the gradient magnitude. In addition to this, there is a broad frequency band present, that includes all but the highest frequencies,
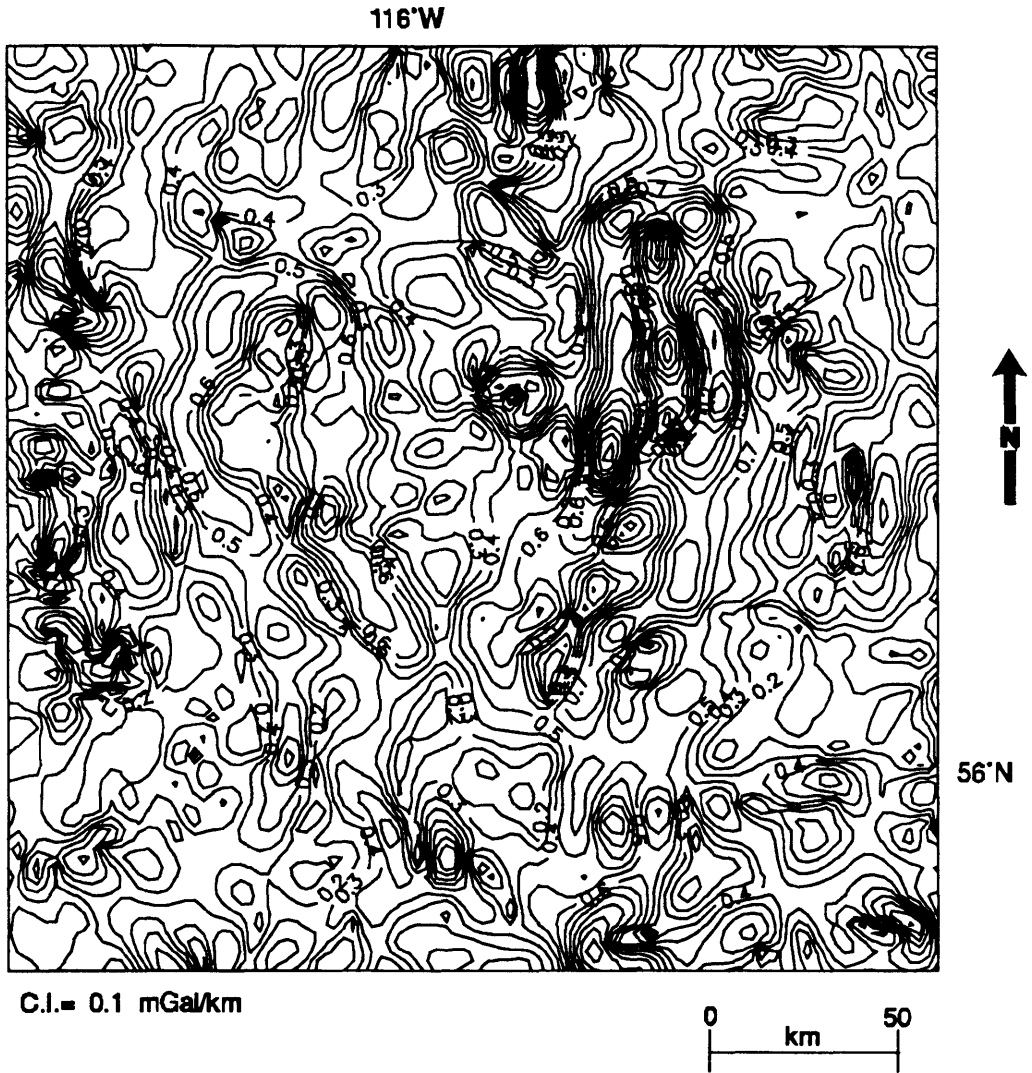
Figure 5.6. Horizontal-gradient magnitude data computed using a 5x5 window, and a third-order polynomial.
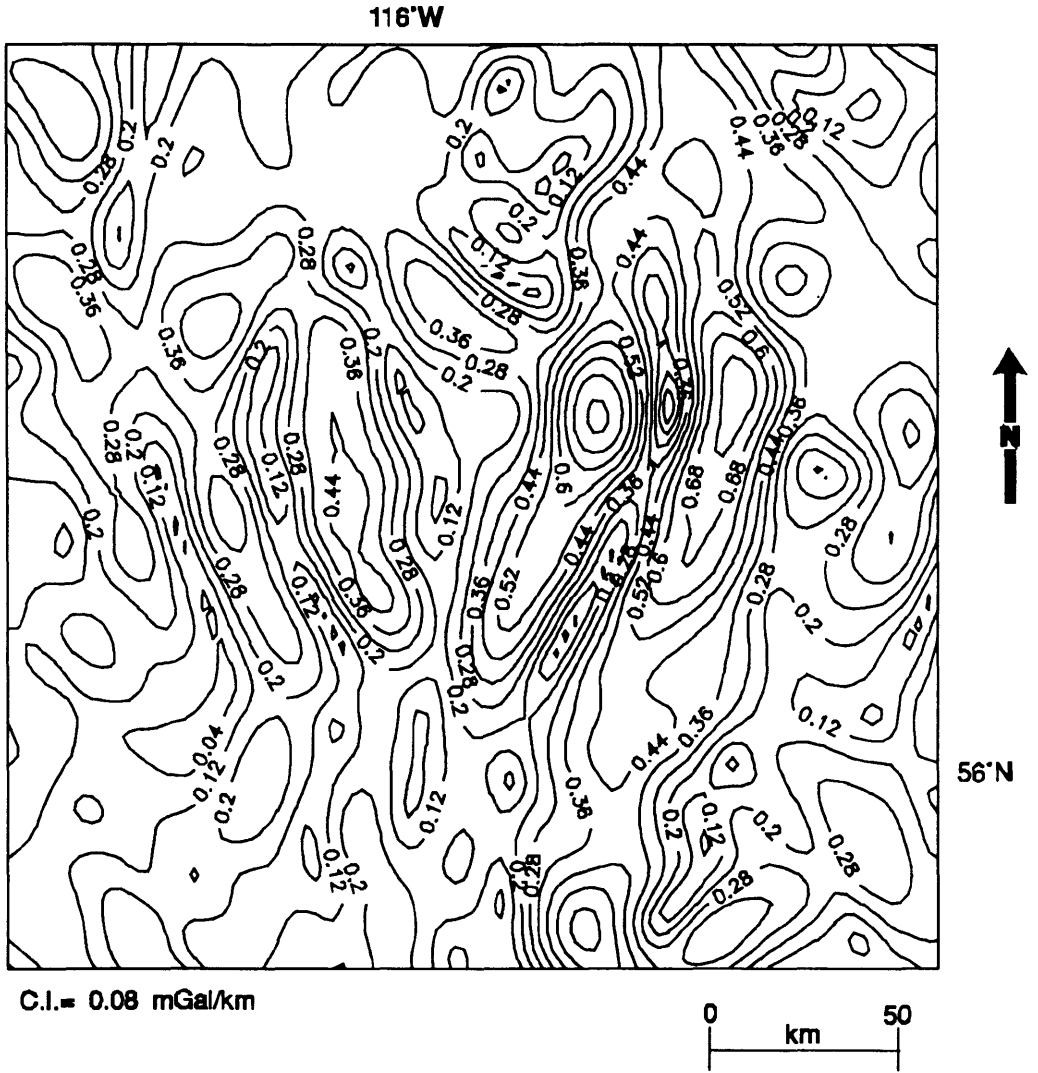
Figure 5.7. Horizontal-gradient magnitude data computed using a 17x17 window, and a second-order polynomial.
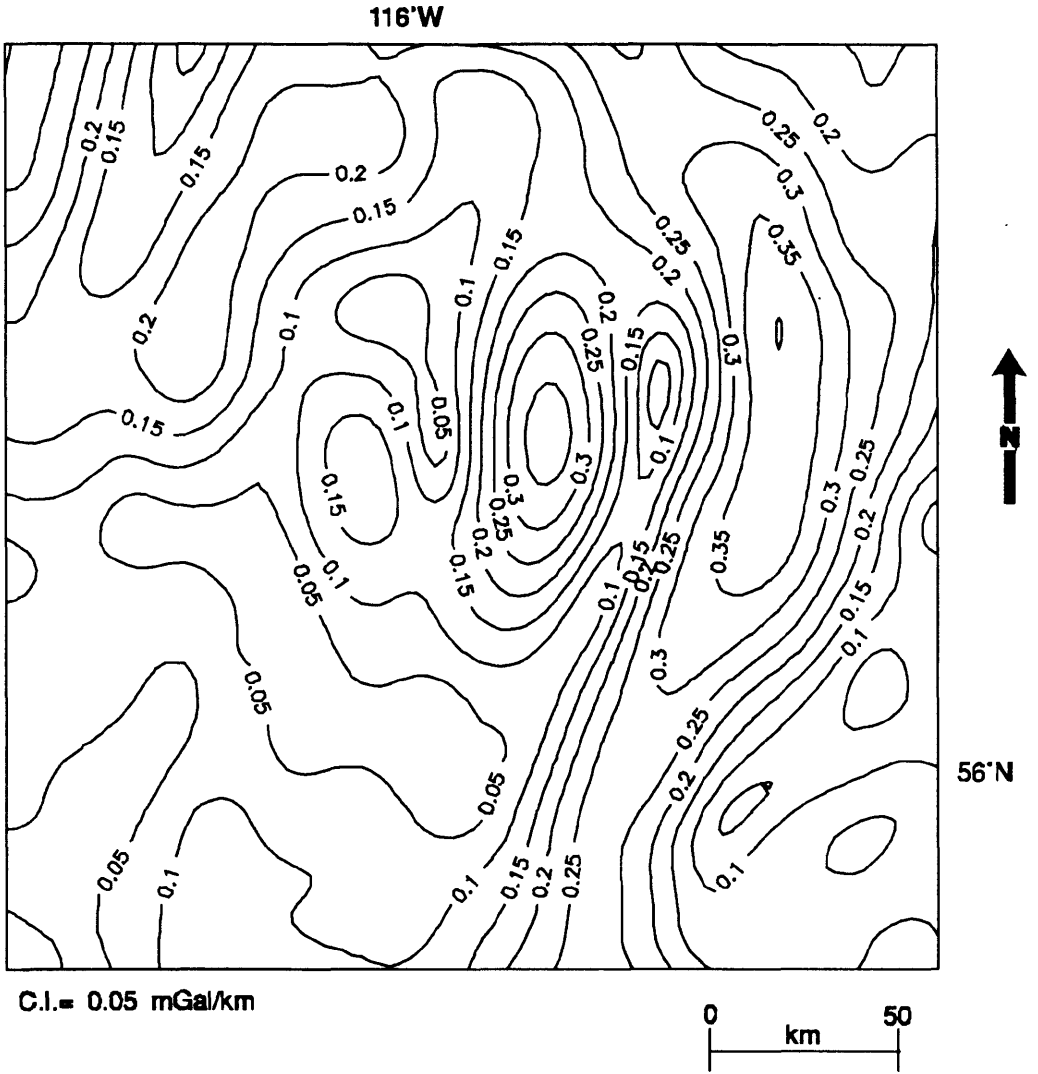
Figure 5.8. Horizontal-gradient magnitude data computed using a 31x31 window, and a first-order polynomial.
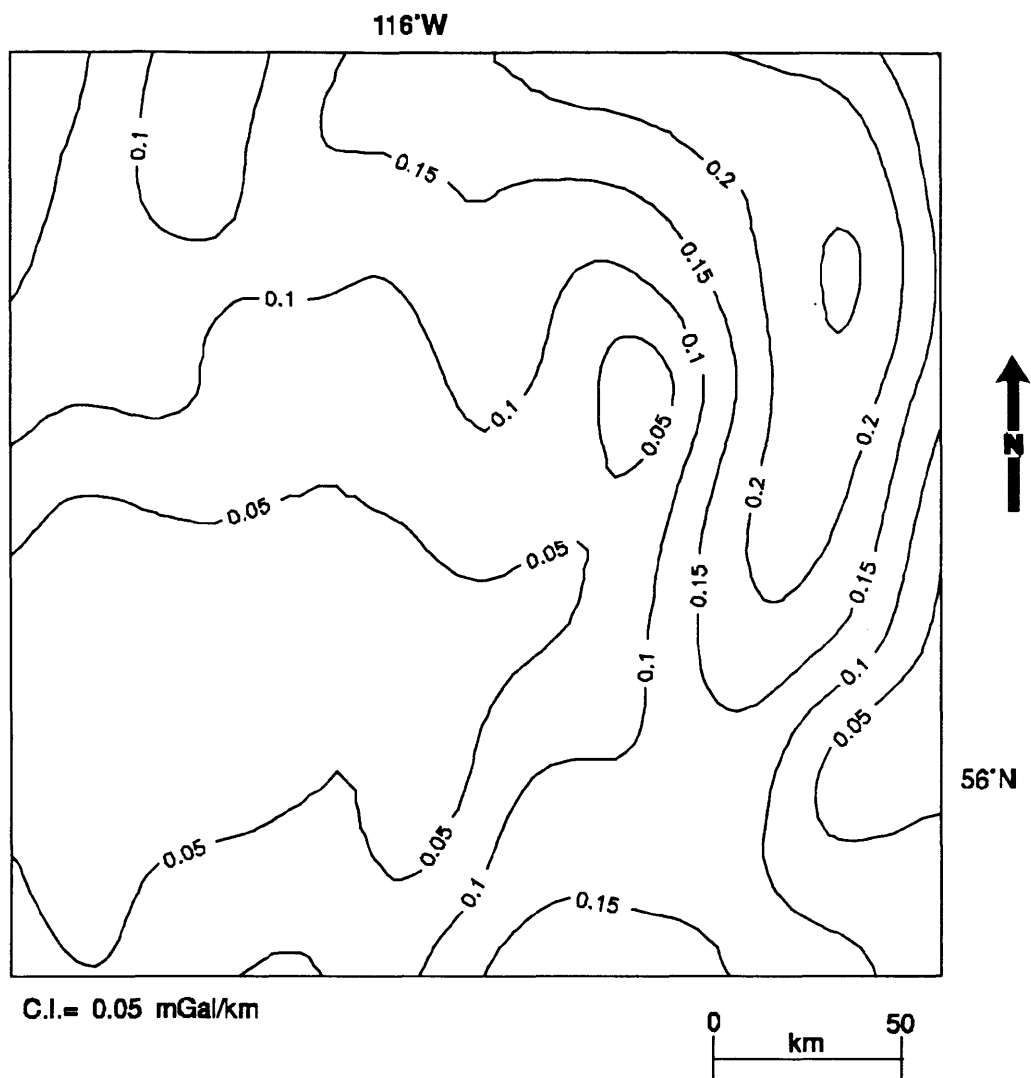
Figure 5.9. Horizontal-gradient magnitude data computed using a 51x51 window, and a first-order polynomial.

in the orthogonal direction. This frequency band is not common to both gradient components, and is thus an ancillary contribution; however it can result in the preservation of high-amplitude anomalies, even if they are not within the passband given in table 5.1.

The predominant feature on the map shown in figure 5.6 is the TML. The gradient-maxima can be used to locate the edges of the pluton. The importance of using a high-frequency gradient-magnitude map to locate the edges of this pluton will be discussed later.

The northern portion is flanked on the east and west by a gradient of 1.8 mGal/km. Here, the gradient maxima are approximately 25 km apart. This width increases to a maximum at the centre of the anomaly, where it is 30 km. In the southern portion the gradient maxima are considerably lower, and are separated by a distance of roughly 35 km. The peak that defines the northern end is readily apparent, however the southern end is not evident. This makes it difficult to measure length accurately, but 140 km is a reasonable estimate. Overall these areal dimensions are in agreement with the modelling results obtained by Burwash and Power (1990); however there is some discrepancy in the southern portion, which was modelled to have a width of 30 km. The good agreement in the northern portion is not surprising, as one of the results of the modelling was that these walls are steep-sided. On the other hand, the western edge of the southern portion was modelled with nonvertical walls that dip to the northwest. For sloping contacts, gradient maxima are offset downdip (Grauch and Cordell, 1987). This would result in the distance between gradient maxima

overestimating the width of the source. Further, for a constant density change, horizontal gradients decrease as the slope of the contact decreases (Hammer and Anzoleaga, 1975). Thus, non-vertical sides for this portion of the Trout mountain pluton may also be the reason for the observation that these are the lowest gradients associated with the TML.

In addition to the TML, the low to the west, speculated to also be caused by a pluton, is delineated well on this map. The northern portion has a width of about 35 km, which narrows to 30 km in the south. Like the TML, the northern end is well-defined, whereas a peak corresponding to the southern end is nonexistent. However, based on the lateral gradients, 120 km is a reasonable estimate for the length.

Although there are a number of other features resolved on this map, like the short-wavelength anomaly maps, it is difficult to determine likely causes for these anomalies. Hence, no attempt will be made to interpret these features other than to note that they are likely caused by shallow crustal bodies.

The map shown in figure 5.7 has undergone enhancement of wavelengths between 125 and 40 km, and thus is most closely associated with the 250-km short-wavelength anomaly map in terms of information. Comparison of these maps indicates that the same features are depicted on both. This pair demonstrate the complementary nature of wavelength-filtered and gradient-magnitude maps. That is, while the 250-km short-wavelength anomaly map, shown in figure 4.2h, shows the magnitude and polarity of the anomalies, the gradient-magnitude map in figure 5.7 highlights geometrical relationships between features. For instance, on the map shown in figure

5.7, the eastern edge of the TML is part of an extensive north-south trend. As well, the northern end of the low to the west of the TML is seen to be truncated by a feature oriented to the northwest. This can be attributed to the fact that horizontal-gradient magnitude maps highlight density boundaries.

As discussed previously, in terms of frequency content, the horizontal gradient-magnitude map shown in figure 5.8 most closely resembles the 125-km long-wavelength anomaly map shown in figure 4.2e. Like the 125-km long-wavelength map, the most prominent feature on this gradient-magnitude map is related to the TML. Here, the pluton is defined by eastern and western maximum gradients of approximately 0.4 mGal/km. It should be noted that the gradient maxima of the TML depicted on this map do not depict the edges of the pluton. This is because the maxima of the gradient of the long-wavelength components of an anomaly are not geographically coincident with the edges of the source body, while the short-wavelength gradients retain the shape information (Kane and Godson, 1985). Hence, areal dimensions should only be estimated from the short-wavelength gradient-magnitude signature.

Aside from resolving the long-wavelength component of the stronger anomalies, there is a subtle feature on figure 5.8 that is not evident on any of the wavelength-filtered maps. This is the northwest trending ridge of magnitude 0.06 mGal/km, in the southwestern portion of the map. The centre of this ridge is coincident with the maximum gradient, as imaged on figure 5.6, that corresponds to the eastern edge of the smaller pluton. This is interesting because the southeastern

portion of this ridge appears to be an extension of the maximum that corresponds to the eastern edge of the smaller body. The fact that it extends to the southeastern portion of the TML may signify that this body joins the Trout Mountain pluton.

On the gradient-magnitude map shown in figure 5.9 wavelengths between 500 and 125 km have been highlighted. Thus, the northeasterly oriented low resolved on the 250-km long-wavelength map (figure 4.2g) should be obvious. While the eastern portion of this feature is outlined by a peak, the anomaly is not as well defined on this map as it is on its wavelength-filtered counterpart. This is largely due to the presence of the TML, which is not completely removed by the gradient-component filters. This is a second example of leakage of frequency bands that are not within the specified passband. In this case this is detrimental, as it precludes delineation of this gravity low.

Summary and conclusions

The following conclusions regarding local and global least-squares polynomial approximation can be drawn from this study:

In some cases, global polynomial approximation has been observed to cause a geographic shift of the centres of anomalies with respect to their location on maps filtered by phase-invariant operators. This has been attributed to spatially-dependent phase distortion.

Global and local least-squares approximation by polynomials defined by equation 2.1a are hampered by the fact that these polynomials result in the

transmission of considerably higher frequencies along the directions of the coordinate axes. This degrades features that are oblique to the axes. Polynomials defined by equation 2.1b are more equitable, and are thus more dependable. Nevertheless, regional fields for both polynomial types should be computed, because using polynomials defined by equation 2.1b rather than 2.1a has been shown to introduce artificial anomalies. This may be due to a combination of including extra terms in the approximating polynomial, and phase distortion.

Because of the extra terms, global approximation by polynomials defined by equation 2.1b is more computationally intensive than approximation by polynomials defined by equation 2.1a.

The following conclusions regarding horizontal-gradient magnitude maps can be drawn from this study:

Horizontal-gradient maps are comparable to wavelength-filtered maps that have cutoff wavelengths twice as long.

Gradient-magnitude maps highlight density boundaries. This facilitates measurement of areal dimensions from the gradient-magnitude maps. This must be done from the short-wavelength maps, as the longer-wavelength components do not retain the shape information. In addition, this has been observed to portray subtle features that are not otherwise apparent, and reveal relationships between anomalies that are not obvious on wavelength-filtered maps.

It is difficult to filter out high-amplitude features completely using the horizontal-gradient magnitude, even when these features are outside the passband of

the gradient-component operators. This makes the horizontal-gradient magnitude technique unsuitable for studying long-wavelength crustal features that are masked by higher-amplitude shorter-wavelength features.

Chapter 6 - Conclusions

The framework for this thesis is local least-squares polynomial approximation. This approach entails computing the value of the best-fit polynomial over a subrange centred on, and in the immediate vicinity of, each input data point. Thus, each processed data point originates from a unique polynomial.

Previous studies have demonstrated that for data in one independent variable this technique is equivalent to linear digital filtering (Wood and Hockens, 1970; Chan and Leong, 1972). The present study commences with an extension of this concept to data in two independent variables. This confirms that, like their one-dimensional counterparts, these are phase-invariant low-pass linear digital filters. The two-dimensional operators are complicated by the fact that the transfer functions are not isotropic, and transmit higher frequencies oblique to the axes of the coordinate system. The amount of directional distortion depends upon the terms contained in the approximating polynomial. Hayes (1970) defines two potential forms for these functions, which are given by equations 2.1. Operators designed using polynomials from equation 2.1b have the widest passband at bearings of 45° to the axes; however, the amount of distortion is small compared to that which is induced by operators based on polynomials defined by equation 2.1a.

Analysis of the transfer functions of the impulse responses concentrates on determining high-pass frequencies for various parameter combinations. In addition to quantifying the filtering characteristics, this reveals the following properties of these filters: the high-pass frequency is proportional to the polynomial order, and inversely

proportional to the number of points incorporated in the least-squares fit; using fewer points decreases the directional distortion; and, for a given polynomial order the high-pass frequency varies the most when the number of points is small.

Global approximation entails replacing the entire data set by a single best-fit polynomial. Lance (1982) has shown that this technique is tantamount to filtering with a spatially dependent operator, with a unique weight function for each data point. Towards the centre of the data set, the local and global operators have similar filtering characteristics, and in fact the global filter that acts on the centre data point is identical to a local operator. Thus, the discussion of the filtering characteristics of the local operators has ramifications for the global method. In particular, this suggests that directional dependence is reduced when polynomials defined by equation 2.1b are used in favour of polynomials defined by equation 2.1a. This is demonstrated by application to Bouguer gravity data.

The use of local least-squares polynomial approximation for computing horizontal-gradient vector components was introduced by Sharpton et al. (1987). The derivative rule for convolution facilitates formulation of their method in terms of convolution. This is accomplished by differentiating the expressions for the low-pass local least-squares operators. This gives analytic expressions for the impulse responses of the x- and y-components of the horizontal-gradient vector.

Transfer functions of local least-squares operators have been compared to transfer functions based on two other approaches to computing horizontal-gradient components: finite differences, and ideal low-pass filtered impulse responses designed

in the frequency domain. The former are restricted because the passbands cannot be varied, whereas the latter do not conform to the ideal transfer functions. The local least-squares operators are not hampered by these shortcomings.

Previous workers have recognized that the magnitude of the horizontal-gradient vector can be used to detect edges of features on Bouguer gravity data. When this technique is enhanced by introducing gradient components with a variable frequency content, application to a Bouguer gravity data set has demonstrated the following characteristics:

Subtle features are highlighted. This is particularly true for the longer-wavelength gradient-magnitude maps; and because these features are not necessarily obvious on wavelength-filtered maps, they can enhance the interpretation. As well, these maps complement wavelength-filtered maps by highlighting density boundaries.

When interpreting areal dimensions from horizontal-gradient magnitude maps, it is important to use the high-frequency gradient magnitudes, as the low-frequency components do not represent source-body edges.

A drawback of these maps is that there is a secondary low-pass element that includes a broad frequency band, making it difficult to remove high-amplitude features.

References

Abdelrahman, E.M., Bayoumi, A. I., Abdelhady Y.E., Gobashy, M.M., and El-Araby, H.M., 1989, Gravity interpretation using correlation factors between successive least-squares residual anomalies: Geophysics, 54, 1614-1621.

Abdelrahman, E.M., Riad, S., Refai E., and Amin Y., 1985, On the least-squares residual anomaly determination: Geophysics, 50, 473-480.

Achieser, N.I., 1956, Theory of approximation: Fredrick Ungar Publishing Company.

Agocs, W.B., 1951, Least-squares residual anomaly determination: Geophysics, 16, 686-696,

Båth, M., 1974, Spectral analysis in geophysics: Elsevier Scientific Publishing Company.

Berry, M.J., and Forsythe, D.A., 1975, Structure of the Canadian Cordillera from seismic refraction and other data: Canadian Journal of Earth Sciences, 12, 182-208.

Besl, P.J., 1988, Surfaces in range image understanding: Springer-Verlag.

Blakely, R.J., and Simpson, R.W., 1986, Approximating edges of source bodies from magnetic or gravity anomalies: Geophysics, 51, 1494-1498.

Bott, M.H.P., and Smithson, S.B., 1967, Gravity investigation of subsurface shape and mass distribution of granite batholiths: Bulletin of the Geological Society of America, 78, 859-878.

Burwash, R.A., and Power, M.A., 1990, Trout Mountain anomaly, northern Alberta: its role in the northwest foreland of the Trans-Hudson orogeny, *in* Lewry, J.F., and Stauffer, M.R., eds., The Early Proterozoic Trans-Hudson Orogen of North America: Geological Association of Canada, Special Paper 37, 301-311.

Burwash, R.A., and Culbert, R.R., 1976, Multivariate geochemical and mineral patterns in the Precambrian basement of western Canada: Canadian Journal of Earth Sciences, 13, 1-18.

Chan, S.H., and Leong, L.S., 1972, Analysis of least-squares smoothing operators in the frequency domain: Geophysical Prospecting, 20, 892-900.

Chandler, V.W., Koski, J.S., Hinze, W.J., and Braile, L.W., 1981, Analysis of multisource gravity and magnetic anomaly data sets by moving-window application of Poisson's theorem: Geophysics, 46, 30-39.

Claerbout, J.F., and Muir, F., 1973, Robust modeling with erratic data: Geophysics, 38, 826-844.

Coons, R.L., Woollard, G.P., and Hershey, G., 1967, Structural significance of the mid-continent gravity high: Bulletin of the American Association of Petroleum Geologists, 51, 2381-2399.

Cordell, L., and Grauch, V.J.S., 1985, Mapping basement magnetization zones from aeromagnetic data in the San Juan basin, New Mexico, *in* Hinze, W.J., Ed., The Utility of Regional Gravity and Magnetic Anomaly Maps: Society of Exploration Geophysicists, 181-197.

Cordell, L. 1979, Gravimetric expression of graben faulting in Santa Fe country and the Española Basin, New Mexico: New Mexico Geological Society Guidebook, 30th Field Conference, Santa Fe Country, 39-64.

Davis, J.C. 1986, Statistics and data analysis in Geology: John Wiley and Sons Inc.

Dole, W.E., and Jordan, N.F., 1978, Slope mapping: Bulletin of the American Association of Petroleum Geologists, 62, 2427-2440.

Eaton, D.W.S., 1988, An integrated geophysical study of Valhalla gneiss complex, southeastern British Columbia: M.Sc. Thesis, The University of Calgary.

Erdélyi, A., Mangus, W., Oberhettinger, F., and Tricomi, F.G.,1954, Tables of integral transforms: McGraw-Hill Book Company.

Fajklewicz, Z., 1959, The use of cracovian computation in estimating the regional gravity: Geophysics, 24, 465-478.

Forsythe, G.E., 1957, Generating and use of orthogonal polynomials for data-fitting with a digital computer: Journal of the Society of Industrial and Applied Mathematics, 5. 74-88.

Fuller, B.D., 1967, Two-dimensional frequency analysis and design of grid operators, *in* Mining Geophysics, volume 2, Theory: Society of Exploration Geophysicists, 658-708.

Goodacre, A.K., Grieve, R.A.F., and Halpenny, J.F., 1987, Bouguer gravity anomaly map of Canada, Canadian Geophysical Atlas, Map 3, scale 1:10 000 000.

Grauch, V.J.S., and Sawatzky, 1989, Regional patterns of basin and range structure determined from gravity data of Nevada: Presented at the 59th Annual International Meeting, Society of Exploration Geophysicists, Expanded Abstracts, 353-354.

Grauch, V.J.S., and Cordell, L., 1987, Limitations of determining density or magnetic boundaries from the horizontal gradient of gravity or pseudogravity data, Geophysics, 52, 118-121.

Hammer, S., and Anzoleaga, R., 1975, Exploring for stratigraphic traps with gravity gradients: Geophysics, 40, 256-268.

Hartman, R.R, Teskey, D.J., and Friedberg, J.L., 1971, A system for rapid digital aeromagnetic interpretation: Geophysics, 36, 891-918.

Hayes, J.G., 1970, Numerical approximations to functions and data: University of London, The Athlone Press.

Heiland, C.A., 1943, A rapid method for measuring the profile components of horizontal and vertical gravity gradients: Geophysics, 8, 119-133.

Henderson, R.G., and Cordell, L., 1971, Reduction of unevenly spaced potential field data to a horizontal plane by means of finite harmonic series: Geophysics, 36, 856-866.

Jacobsen, B.H., 1987, A case for upward continuation as a standard separation filter for potential-field maps: Geophysics, 52, 1138-1148.

Jeffreys, H., 1964, Note on Fourier analysis: Bulletin of the Seismological Society of America, 54, 1441-1444.

Kanasewich, E.R., 1981, Time sequence analysis in geophysics: University of Alberta Press.

Kane, M.F., and Godson, R.H., 1985, Features of a pair of long-wavelength (>250 km) and short-wavelength (<250 km) Bouguer gravity maps of the United States, *in* Hinze, W.J., Ed., The Utility of Regional Gravity and Magnetic Anomaly Maps: Society of Exploration Geophysicists, 46-61.

Kilty, K.T., 1983, Werner deconvolution of profile potential field data: Geophysics, 48, 234-237.

Kis, K., 1983, Determination of coefficients for the computation of derivatives of potential fields with respect to x, y and z: Acta Geodaetica, Geophysica et Montanistica Hungary, 18, 501-511.

Ku, J.C., 1990, Integrated basement interpretation of magnetics with subsurface and seismic data: Presented at the 60th Annual International Meeting, Society of Exploration Geophysicists, Expanded Abstracts, 608-609.

Lance, J.O., 1982, Frequency domain analysis of least squares polynomial surfaces with application to gravity data in the Pedregosa basin area: Ph.D thesis, The University of Texas at El Paso.

Lapidus, L., 1962, Digital computations for chemical engineers: McGraw-Hill Book Company Inc.

Letts, P.J. and Rochon, G., 1980, Generation and use of digital elevation data for large areas: Presented at the 6th Canadian Symposium on Remote Sensing, 597-602.

Meskó, A., 1984, Digital filtering: applications in geophysical exploration for oil: John Wiley and Sons Inc.

Peeples, W.J., Coultrip, R.L., and Keller, G.R., 1986, Quasi-ideal spatial filters for large maps: Annales Geophysicae, 4, 547-554.

Ross, G.M., Parrish, R.R., Bowring, S.A., and Tankard, A.J., 1988, Tectonics of the Canadian Shield in the Alberta subsurface: Geological Association of Canada-Mineralogical Association of Canada-Canadian Society of Petroleum Geologists, Program with Abstracts, 13, A106.

Sharpton., V.L., Grieve, R.A.F., Thomas, M.D., and Halpenny, J.F., 1987, Horizontal gravity gradient: an aid to the definition of crustal structure in North America: Geophysical Research Letters, 14, 808-811.

Simpson, S.M., 1954, Least squares polynomial fitting to gravitational data and density plotting by digital computer: Geophysics, 19, 255-269.

Sprenke, K.F., and Kanasewich, E.R., 1982, Gravity modelling and isostasy in western Canada: Journal of the Canadian Society of Exploration Geophysicists, 18, 49-57.

Stephenson, R.A., Zelt, C.A., Ellis, R.M., Hajnal, Z., More-à-l'Huissier, P., Mereu, R.F., Northey, D.J., West, G.F., and Kanasewich, E.R., 1989, Crust and upper mantle structure of the origin of the Peace River Arch: Bulletin of Canadian Petroleum Geology, 37, 224-235.

Stewart, R.R., 1985, Median filtering: Review and a new F/K analogue design: Journal of the Canadian Society of Exploration Geophysicists, 21, 54-63.

Swarz, C.A., 1954, Some geometrical properties of residual maps: Geophysics, 19, 913-928.

Syberg, F.J.R., 1972, A Fourier method for the regional-residual problem of potential fields: Geophysical Prospecting, 20, 47-75.

Telford, W.M., Geldart, L.P., Sheriff, R.E., and Keys, D.A., 1976, Applied geophysics: Cambridge University Press.

Thomas, M.D., Grieve, R.A.F., and Sharpton, V.L., 1988, Gravity domains and assembly of the North American continent by collisional tectonics: Nature, 331, 333-334.

Thomas, M.D., Sharpton, V.L., and Grieve, R.A.F., 1987, Gravity patterns and Precambrian structure in the North American Central Plains: Geology, 15, 489-492.

Thorarinsson, F., Magnusson, S.G., and Bjornsson, A., 1988, Directional spectral analysis and filtering of geophysical maps: Geophysics, 53, 1587-1591.

Thurston, J.B., Brown, R.J., and Lyatsky, V.B., 1990, Horizontal gradient maps of gravity and magnetic data in western Canada: Presented at the National Convention of the Canadian Society of Exploration Geophysicists.

von Frese, R.R.B., Hinze, W.J., and Braile, L.W., 1982, Regional North American gravity and magnetic anomaly correlations: Geophysical Journal of the Royal Astronomical Society, 69, 745-761.

Walcott, R.I., and Boyd, J.B., 1971, The gravity field of northern Alberta and part of Northwest Territories and Saskatchewan: Gravity Map Series of the Earth Physics Branch, Nos. 103-111.

Wood, L.C., and Hockens, S.N., 1970, Least squares smoothing operators: Geophysics, 35, 1005-1019.

Wylie, C.R., 1960, Advanced engineering mathematics: McGraw-Hill Book Company Inc.

Zeng, H., 1989, Estimation of the degree of polynomial fitted to gravity anomalies and its applications: Geophysical Prospecting, 37, 959-973.

Zurflech, E.G., 1967, Application of two-dimensional linear wavelength filtering: Geophysics, 32, 1015-1033.